High Impedance Ion Acceleration using Applied Diverging Magnetic Fields

Daisuke ICHIHARA

A dissertation submitted in partial fulfillment of the requirements for
the degree of Doctor of Philosophy
(Department of Aerospace Engineering)
in
Nagoya University

September 2017

Dissertation committee:

Professor	Akihiro SASOH, Chair
Professor	Noriyasu OHNO
Professor	Jiro KASAHARA
Lecturer	Akira IWAKAWA

Acknowledgements

First of all, I would like to acknowledge my supervisor Prof. Akihiro Sasoh for all the support throughout my doctoral work. You kindly accepted me as a doctoral student after my graduation of master degree. I am grateful for all your support for research, how to control my motivation, and social rules and manners. I was always interested in experiments and analysis, but you told me the importance of finalizing project, including journal publications, conferences and this dissertation.

I also want to thank Associate professor Shigeru Yokota. I learned a lots of important experimental skills and analyzing procedures of plasma physics and electric propulsion. Dr. Akira Iwakawa gave me a lots of valuable suggestions and comments for all of my work. I learned how to summarize results in logically and how to make an explicit presentation. I also want to thank my committee members of this dissertation, Professor Noriyasu OHNO, and Professor Jiro KASAHARA for taking time and making a lots of valuable suggestions and comments for this dissertation.

I was also lucky to have so many good alumni of Ionized Gas Dynamics Laboratory. Mr Shota Harada, Mr Tomoki Uno, Mr Hisashi Kataoka, Mr Teruaki Baba, and Mr Akira Uchigashima. Your good experimental works were so valuable in this dissertation.

Finally, I would like to express my gratitude to my family for their understanding, lots of support and encouragement.

Daisuke ICHIHARA

Table of contents

List of Figures

List of Tables

Nomenclature

A	correction area
A_{eff}	effective collection area
A_{p}	probe exposed area
A_{s}	electrode collection area in double probe
B	magnetic field strength
$\mathbf{B}$	magnetic field vector
$\overline{B}$	representative magnetic field strength
$c_{\mathrm{i,eff}}$	effective ionization cost, Eq. (4.5)
c_{v}	voltage coefficient in Eq. (3.8)
$c_{\mathrm{v,RR}}$	voltage coefficient in rigid rotator model, Eq. (3.9)
d	inter electrode distance in **E×B** probe
e	elementary charge
$\mathbf{E}$	electric field vector
E	electric field strength
E_{i}	ion beam energy
F	thrust
F_1	thrust in time zone 1, Fig.2.8
F_2	thrust in time zone 2, Fig.2.8
F_{A}	applied-field thrust
f_{u}	electron's velocity distribution function of electron
f_{ε}	electron's energy distribution function of electron
F_{EXP}	experimentally measured thrust
F_{S}	self field-thrust
F_{tare}	tare force
g	gravity acceleration constant
I	collected current in double probe
I_{sat}	ion saturation current in double probe
I_{sp}	specific impulse, Eq. (3.10)
$\mathbf{j}$	discharge current density vector
$\hat{J}_1$	working gas flow rate through anode or helicon plasma source in ampere equivalent
$\hat{J}_2$	working gas flow rate through the hollow cathode in ampere equivalent
J_{c}	collected ion current
J_{d}	discharge current
$J_{\mathbf{E\times B}}$	collected ion current in **E×B** probe
J_{h}	heater current in emissive probe

J_i	ion beam current
j_i	ion beam current density
$J_{i,Z}$	ion current of Z-charged ions
J_k	keeper current
k	Boltzmann constant
$\dot{m}$	total mass flow rate
$\dot{m}_1$	mass flow rate through hollow cathode, Fig.3.2
$\dot{m}_2$	propellant mass flow rate through injection port 2, Fig.3.2
m_e	electron mass
m_i	ion mass
$m_{i,Z}$	ion mass of Z-charged ion
n_e	electron number density
$n_{i,Z}$	number density of Z-charged ion
P	electric power
P_a	anode power loss
P_s	RF input power
R	radius
R_a	anode radius
R_c	cathode radius
r_p	probe radius
r_{probe}	radial probe position
T_e	electron temperature
u	velocity
$\mathbf{u}$	velocity vector
u_A	characteristics exhaust velocity of applied-field force
u_e	exhaust velocity
$u_{\mathbf{E}\times\mathbf{B}}$	ion velocity inside **E×B** deflection section
$u_{i,Z}$	velocity of Z-charged ion
u_S	characteristics exhaust velocity of self-field force
V	voltage
V'_0	the sum of the anode sheath drop and the cathode sheath drop, Eq. (3.8)
V_0	the sum of the plasma's electrical resistance and sheath potential drops, Eq. (3.8)
$V_{a,Z}$	acceleration voltage of Z-charged ion
V_d	discharge voltage
$V_{\mathbf{E}\times\mathbf{B}}$	applied voltage difference in **E×B** probe
V_f	floating potential with respect to the cathode potential
V_k	keeper discharge voltage

V_p	double probe voltage
V_{RPA}	RPA's third grid potential
V_s	space potential with respect to cathode
Z	charge state
z_c	cathode position in Af-MPD thruster
z_{probe}	axial probe positon
α	applied-field thrust ratio against to self-field thrust, Eq. (3.3)
δ	sheath thickness
ε_0	permittivity in vacuum
$<\varepsilon_i>$	average ion kinetic energy
$<\theta>$	ion beam divergence half-angle
η	thrust efficiency, Eq.(3.11)
$\eta_{a,Z}$	voltage efficiency of Z-charged ion
κ	density decrement inside pre-sheath
λ_D	Debye length
σ	standard deviation
φ_a	anode potential
φ_b	beam potential, Fig.2.10
φ_s	space potential, Fig.2.10
χ^2	expected value
$\omega_{c,e}$	electron cyclotron frequency
$\omega_{c,i}$	ion cyclotron frequency
ω_{LH}	lower hybrid frequency
r,θ,z	cylindrical coordinates
x,y,z	Cartesian coordinates

1.

Introduction

1.1. Current states of 1-kW-class electric propulsions

Nowadays, electric propulsion is widely used in space crafts for their attitude control,[1-5] orbit raising and even as a bus equipment in space exploration. The development of electric propulsion started from 1960',[6,7] and the first demonstration in space was an ion engine, which was tested in the Space Electric Rocket Test (SERT-1) mission in 1964.[8,9] Since then, numerous ground experiments, numerical studies, and orbit demonstrations have been conducted.[10-26] In 2013, more than 200 space crafts were equipped with electric propulsion system and operated in space.[27]

Because the available power in space is limited up to 10 kW class, the input power to the electric propulsion system is mainly 1 kW class. For example, the electric propulsion named as "satellite-plasma-thruster (SPT) series" (primarily used for attitude controls propulsion system of 6 tons class of satellites) is operated with 1.5 – 4.5 kW input power and can exhaust xenon propellant at 16 – 18 km/s.[28,29] The input power to the 25 cm-Xenon Ion Propulsion System (XIPS)[30] and PPS®-5000[31] (used for orbit rising from low earth orbit to geo stationary orbit) was 4.5 kW and 5.0 kW, respectively. The input power to the NASA Solar electric propulsion Technology Application Readiness (NSTAR)[32] (the main engine of Deep Space 1[33] and Dawn asteroid probe[34]) and PPS®-1340[31] (the main engine of Small Missions for Advanced Research in Technology-1 (SMART-1) moon probe[35]) was 2.3 kW and 1.1 kW, respectively. In addition to the input power, the exhaust velocity u_e and thrust-to-power ratio F/P (which means thrust with unit input power) are necessary to calculate the required propellant mass and transition time to the designated orbit with specified velocity increment requirements.[36] For $P \sim 1$ kW class operation,

scaling laws about thruster geometries, operating conditions and semi-empirical optimum operating conditions to maximize thrust efficiency have been proposed.[37-40] Existing thrusters, which operated in space, were designed based on these criteria and typical thruster performances of u_e ~ 14 km/s, F/P ~ 40 mN/kW were achieved.[30,41,42]

1.2. High impedance ion accelerations and wall losses

The input power P to the electric propulsion is given by the product of the discharge current J_d and the discharge voltage V_d, i.e. $P \equiv J_d V_d$. Even with the same input power, the acceleration mechanisms and design criteria could be different depending on the set value of J_d and V_d.

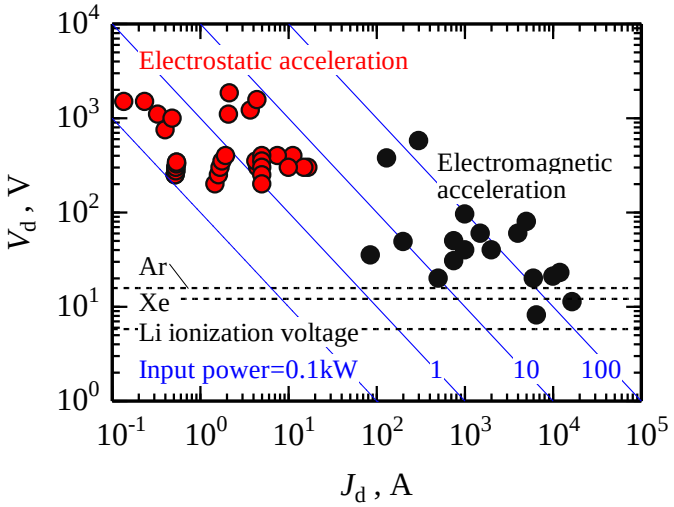

FIG. 1.1 Typical operating conditions of 0.1-100 kW input power electric propulsions.[17,30,41]

Figure 1.1 shows J_d and V_d values of typical electric propulsion system in each input power operation. In Fig 1.1, ionization energies of typical propellants such as Ar (15.8 eV), Xe (12.1 eV), and Li (5.4 eV) are also shown as dashed lines. Depending on the input power, the J_d and V_d set values are roughly classified in two types. In input power P ~ 1 kW class operation, small J_d (~10^1 A) and high V_d (~10^3 V) values are utilized. In this dissertation, this small current and high voltage operation is referred to as “high impedance operation”. Most of the existing electric propulsions with high impedance operation are classified under the electrostatic acceleration type (see red symbols in Fig. 1.1), in which a thrust is generated by electrostatically accelerating the ions.

According to the energy consumption laws of electrostatic acceleration, the ratio of ionization power dissipation to the total input power can be decreased by increasing the discharge voltage.[43] Thus, with the constant input power, the electric energy is efficiently converted to ion kinetic energy by the high impedance operation. The electric field to accelerate the ions is maintained by installing grid electrodes inside plasma flow[44] or applying magnetic field in the discharge channel.[25] XIPS and NSTAR have a set of grid electrodes at the thruster exit. The ions are collimated towards exhaust direction and electrostatically accelerated without collisions by using the potential difference between the grid electrodes. PPS®-5000 and PPS®-1340 have an applied magnetic field in radial direction. Figure 1.2 shows the electrodes and applied magnetic field configurations of these PPS® series thrusters. Typically, $B \sim 50$ mT of magnetic field is applied in the direction perpendicular to the discharge channel wall between the upstream anode and downstream hollow cathode. It is well known from the classical diffusion theory, that the electron mobility perpendicular to the magnetic lines of force is proportional to B^{-2} and the mobility perpendicular to the magnetic lines of force is 2 – 3 orders smaller than that along the magnetic lines of force.[45] Accordingly, low mobility electrons emitted from the hollow cathode are trapped by the applied radial magnetic field. As a result, electric impedance increases locally and axial electric field is maintained. This axial electric field accelerates electrons. Propellants supplied from upstream are ionized by collision with the accelerated electrons and, subsequently accelerated by the electric field.

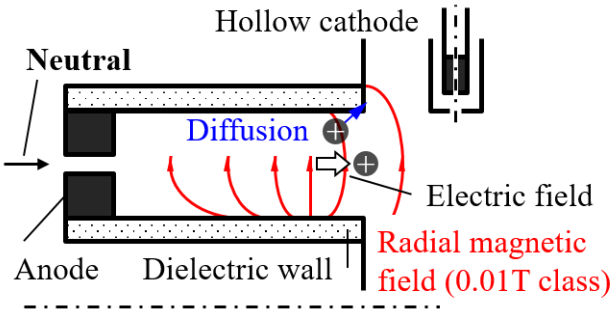

FIG. 1.2 Schematics of ion accelerator using radial magnetic field.

The small electron mobility perpendicular to the magnetic lines of force makes magnetic lines of force equals to equipotential surface. In practice, it is difficult to apply uniform radial magnetic field in the acceleration region because of the leaked magnetic field which result in bending of lines of force. Therefore, a part of the generated ions is accelerated towards the discharge channel wall and recombines at the wall surface.[46-49] Ion collisions with the wall causes not only thrust[50,51] but also loss in the input energy. As a result of ion bombardments, the discharge wall temperature increases and 10 – 20% of the input power is consumed in this wall heating.[52,53] Moreover, the ion bombardment erodes the discharge channel wall at, typically, 15 – 20 μg/h[54] and restricts the thruster lifetime.[55-57] It is shown in Ref. 38 that decreasing the input power miniaturizes the discharge channel and decreasing the volume-to-surface ratio makes the ion bombardment more effective.

1.3. Ion-wall-loss mitigation campaigns in electrostatic accelerator

To address the above mentioned problems, several ion-wall-losses mitigation method have been proposed.[58-72] Hofer et al.[60] proposed the concept of "magnetic shielding", where an acceleration channel design is combined with that for an applied magnetic field so that ion collisions against the discharge channel wall are mitigated with a superimposing magnetic field along the channel wall. The effectiveness of this scheme was demonstrated for 6-kW class laboratory Hall thrusters.[61,62] However, the scheme is still under development, especially in a power range lower than 1 kW operation.[63] Mazouffre et al.[71] proposed the "external discharge Hall thruster", where both ionization and electrostatic acceleration occur outside the discharge channel. Due to the diffusion of accelerated ions caused by curved magnetic field the thruster performance deteriorated.[72] Fisch et al.[64] proposed a cylindrical Hall thruster, which consists of an upstream annular part and a downstream cylindrical part and have a cusped magnetic field in the effective acceleration region to make the accelerating electric field slightly inclined inward the radial direction for mitigating ion bombardments. Figure 1.3(a) shows the schematic of a cylindrical Hall thruster. Based on thrust measurements,[69] the thruster performances were $u_e \sim 15$

km/s and F/P ~ 40 mN/kW. These approaches of magnetic shielding, external discharge, and changing discharge channel geometry are based on the conventional Hall thruster principles of trapping electrons by a radially magnetic field dominant configuration.

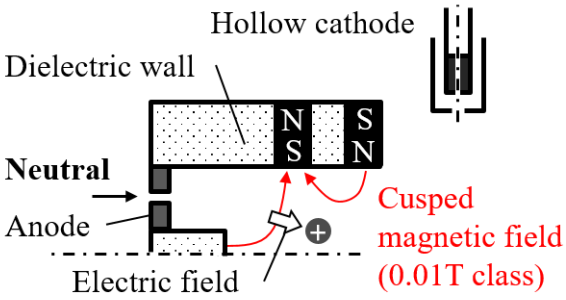

(a) Cylindrical hall thruster[64]

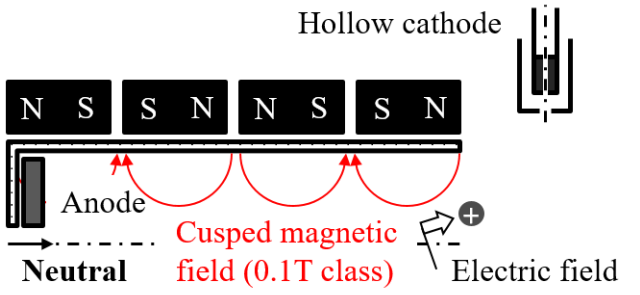

(b) High efficiency multistage plasma thruster[74]

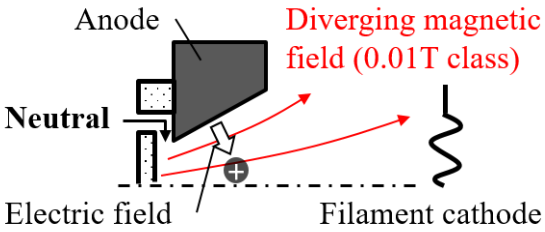

(c) End-hall thruster[79]

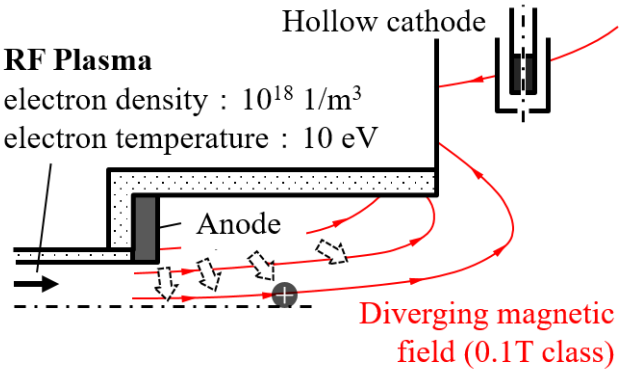

(d) Helicon electrostatic thruster[80]

FIG. 1.3 Schematics of ion trajectory control by using applied magnetic fields.

THALES Electron Devices GmbH in Ulm developed another concept of a High Efficiency Multistage Plasma (HEMP) thruster.[73] Figure 1.3 (b) shows the schematic of a HEMP thruster.[74] In this scheme, an axisymmetric discharge chamber is magnetically separated, between the upstream anode and the downstream cathode, by a cusped magnetic field into several stages. Because of strong magnetic field at each cusped region, axial electric field parallel to the discharge chamber wall is maintained and ions are accelerated towards the exit. However, in the "external discharge" approach also, ion beams are extracted with a large diverging half-angle due to the large curved magnetic field at the final stage of the cusped region and hence deteriorate the thruster performance.

Confining plasmas by a magnetic nozzle is another possible method to mitigate ion-wall collisions.[75] Ahed et al.[76] proposed a critical magnetic field strength above which high-confinement operation is achieved in a helicon plasma thruster, which expands helicon plasma through the diverging magnetic nozzle without direct current discharge for acceleration.[77] However, based on the energy conservation law, the average ion kinetic energy in exhaust plume is limited by the plasma enthalpy in the plasma source. Therefore, compares with electrostatic or electromagnetic accelerators with a pair of anode and cathode, the expected thrust level is a few millinewtons with a relatively low specific impulse.[78] Kaufman et al.[79] developed an End-Hall thruster (or ion source), which is an electrostatic ion accelerator and combines the diverging magnetic field and a pair of electrodes: a schematic is shown in Fig. 1.3(c). The End-Hall thruster has a diverging section in its anode and central filament cathode. A conical "potential well" is formed over the anode inner surface so that the accelerated ions bounce back and forth against the well, and the extracted ion beam has a wide angular distribution. This configuration is suitable for plasma processing rather than space propulsion application because it uniformly distributes ion beams over a large diverging angle.

Harada et al.[80] developed another type of electrostatic thruster, named "Helicon Electrostatic Thruster (HEST)", which has a radio frequency (RF) plasma source connected to an electrostatic acceleration part. Figure 1.3(d) shows the ion acceleration concept of HEST. A diverging magnetic field was applied between an upstream ring anode and a downstream hollow cathode. The magnetic lines of force are greatly modified downstream by permanent magnets and soft iron yokes, generating a magnetic field free region where the field strength is less than 3 mT. The hollow cathode is set in this field free region. Assuming that emitted electrons from the hollow cathode diffuse along the magnetic lines of force, the space potential at center axis is kept at the cathode potential. Radial inward electric field expected to be induced between the anode and the cathode potential center axis and ions generated at the RF plasma sources are accelerated toward

the center axis. Hence, ions are accelerated toward the direction, which is apart from the discharge channel wall and the ion bombardments are expected to be mitigated.

This brief review shows that mitigating ion bombardment with keeping high thruster performance has not been achieved. Suppressing the divergence of the ions in radial magnetic field is difficult due to the large curvature of the lines of force. As expected in Ref. 80, electrostatic ion acceleration in diverging magnetic field has a possibility to consistent the ion bombardment mitigation with higher thruster performance.

1.4. Research objective and thesis outline

The objective of this thesis is to demonstrate high impedance ion acceleration in diverging magnetic field by integrating several elemental technologies: maintaining high impedance discharge in a strong magnetic field, electrostatic ion acceleration in diverging magnetic field, and enhancing ionization near the anode.

In Chapter 2, the experimental apparatuses and data analysis procedure for each parameter are described in detail. Two types of vacuum chambers (Chamber-A and Chamber-B) were used for thrust measurement and plasma diagnostics. A pendulum-type thrust stand measured tens of millinewton-class thrust. Thrust stand calibration method and procedure to correct the electromagnetic interaction forces are also described. In this experiment, five types of plasma diagnostic tools were used. The measurement principle, data analysis procedure, and error analysis for each diagnostic tool are described in detail.

In Chapter 3, high impedance, electromagnetic acceleration in diverging magnetic field is focused. The direct current discharge in diverging magnetic field is utilized in magnetoplasmadynamic (MPD) thruster[44] in which both ions and electrons are accelerated by an electromagnetic force[16] in low impedance condition, i.e. large discharge current and low discharge voltage[17] (see black symbols in Fig. 1.1). In this chapter, the hollow cathode is utilized as a discharge cathode in applied field type MPD (Af-MPD) thruster and demonstrate the high impedance, direct current discharge in diverging magnetic field with up to 265 mT of strength.

The power consumption in the anode sheath, as one of the main power loss mechanisms, is also discussed.

Chapter 4 describes the contributions of pre-ionized working gas injection scheme in an electrostatic ion acceleration in HEST operation. The acceleration performances are characterized by the input RF power. In short, small amount of the RF power enhances ionization and acceleration of the working gas; however, excessive amount of the RF power is only consumed for generating low energy, doubly charged ions with high ion generation cost. The thrust efficiency will be governed by the input power balance between ion generation and electrostatic acceleration. In the last section of this chapter, the optimum input power balance to maximize thruster performance is discussed.

In Chapter 5, wall-less ion acceleration demonstrated by diverging magnetic field electrostatic thruster (DM-EST) is demonstrated. Owning to an electron cloud in the downstream region, the generated potential structure had small potential drop near the anode and large potential drop from the exit of the diverging magnetic field. The magnetic field strength and its distribution inside the ring anode affect both ionization and electrostatic acceleration characteristics. By strengthening the magnetic field only near the ring anode inner surface, high electron number density region of 10^{20} m^{-3}appears locally near the ring anode inner surface. Ions are accelerated from anode potential by obliquely inward electric field and extracted as ion beam.

2.

Experimental apparatuses and procedures

In this chapter, experimental apparatuses and procedures are described in detail. In this experiment, two different vacuum chambers named as Chamber-A and Chamber-B were used. In Chamber-A, direct thrust measurements were conducted by using a gravity pendulum type thrust stand (see Section 2.2). Chamber-B is smaller in size and has a traverse system consisting of a two-axis, automatic linear stage and a stepping motor.

2.1. Vacuum Chamber

2.1.1. Chamber-A

2.1.1.1. Vacuum pumping systems of Chamber-A

Chamber-A is made of stainless steel, and has a cylindrical shape with an inner diameter of 2000 mm and axial length of 4000-mm. The inner surface is of Chamber-A polished to a grade of #600. Figure 2.1 shows the schematics of Chamber-A. Chamber-A is evacuated from atmospheric pressure to 200 Pa by a rotary pump (2100SD, adixen Vacuum Products) with an exhaust speed of 33.3 l/s followed by a turbo molecular pump (3203LMC, SHIMAZU Corporation) with an exhaust speed of 3200 l/s. An air-cooled chiller (CF700, cooling capacity; 0.7 kW, Yamato Scientific Co., Ltd.) is used for the water-cooling of the turbo molecular pump. The ambient pressure inside Chamber-A is measured at one-end at the downstream surface of the chamber, by using a Pirani gauge (GP-1S, ULVAC, Inc.) and an ionization gauge (GI-TL3, ULVAC, Inc.). Because the ionization gauge is calibrated in N_2 gas, a conversion factor of 1.34 is used to correct the measured pressure value. The ultimate pressure is 1.0×10^{-3} Pa. With an argon supply of 0.41, 1.25, and 2.08 mg/s, the ambient pressure inside Chamber-A was 6.0×10^{-3}, 18×10^{-3}, 30×10^{-3} Pa,

respectively. Chamber-A has a VF-400 flange in its upper surface. The gravity pendulum type thrust stand for direct thrust measurement is connected to the VF-400 flange. The thrust stand also works as a feed-through for solenoid-coil-current, propellant, and cooling water. The details of the thrust stand are described in section 2.2.

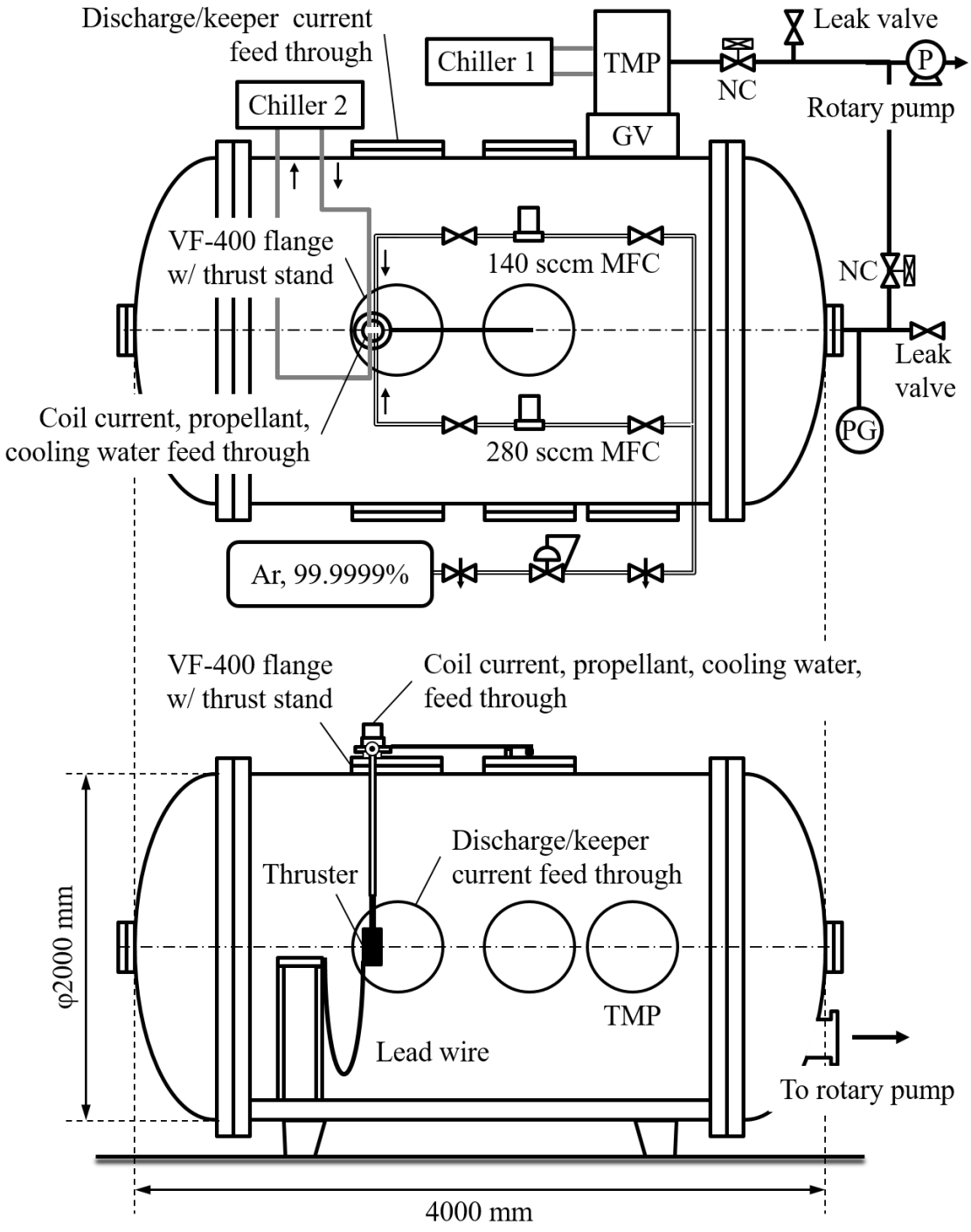

FIG. 2.1 Schematics of Chamber-A.

2.1.1.2.Feed systems

In this dissertation, argon (purity; 99.9999%) was used for as the propellant. The propellant supplied through a 1/4 in. stainless steel tube and a 1/4 in. urethane tube. The internal pressure of the supplying tube was regulated to about 0.2 MPa, and branched into two flow lines: one for the main discharge and the other for the hollow cathode discharge. To control the flow rate in each flow line, two mass flow controllers (MODEL3660, KOJIMA INSTRUMENTS INC.) were used. The maximum argon flow for each mass flow controller was 280 sccm for the discharge flow line and 140 sccm for the hollow cathode flow line. To control each of the mass flow controllers, lead-out units CR-200 for discharge line and CR-300 for the hollow cathode line were used, both made by KOJIMA INSTRUMENTS INC. The flow control accuracy is 1% of the maximum value. After these mass flow controllers, both flow lines are connected to the propellant feed–through, which located at the top part of the thrust stand. Inside the thrust stand arm there are four 1/4 in. copper tube. One of the copper tubes supplies propellants to the thruster and to the hollow cathode. The rests of the tubes are used for supplying cooling water. In order to improve the response time of the flow controls, both mass flow controllers located near the propellant feed-through.

In these experiments, steady-state operation characteristics were investigated. To avoid the melting of the anode and the breakdown between solenoid coil wires, an air-cooled chiller (PCU-6300R, cooling capacity: 6.3 kW, Apiste Corporation) was used for both the anode and solenoid coil water-cooling. Distilled water was used as coolant. The coolant line of the anode was connected to that of the solenoid coil in series. The coolant was supplied through the 1/4 in. copper tube inside the thrust stand arm. The cooling water circulated from the solenoid coil to the anode.

Electrical power for both the discharge and hollow cathode operation were supplied through a current feed-through, which located at the side flange of Chamber-A. The solenoid coil current was supplied through the 1/4 in. copper tubes, which also used for supplying cooling water. Chamber-A was electrically grounded for safety. Power supplies for the discharge, hollow cathode

operation, and solenoid coil were all direct current type and controlled in constant current (CC) mode. The specifications of each power supply are summarized in Table 2.1.

Table 2.1 Power supplies used in the experiments in Chamber-A.

Application	CC/CV/RF	Model number	Manufacturer	Specification
Main discharge	CC	HX01000-12M2I	Takasago Ltd.	1000 V, 36 A
	CC	HX01000-12M2B×2		
Hollow cathode discharge	CC	KC8002	Kaufman & Robinson Inc.	800 V, 2 A
Solenoid coil	CC	PWR1600L	Kikusui Electronics Corp.	~80 V, ~100 A
	CC	N8761A	Keysight Technologies	300 V, 17 A

2.1.1.3.Data acquisition systems

All telemetry signals were collected by an oscilloscope (DL750, Yokogawa Meters & Instruments Corporation) with plug-in modules (701250, 12 bit resolution, Yokogawa Meters & Instruments Corporation) at a sampling rate of 100. A discharge voltage (voltage difference between the anode and the cathode) and a keeper voltage (voltage difference between a keeper electrode and the cathode) were measured with high-voltage probes, connected parallel to the discharge circuit; P6015A (damping ratio: 1000:1, TEKTRONIX, Inc.) for the discharge voltage and P5100A (damping ratio; 100:1, TEKTRONIX, Inc.) for the keeper voltage. The ambient pressure inside the Chamber-A was recorded by using a monitor signal (linearity: ± 15%) from the ionization gauge.

2.1.2. Chamber-B

2.1.2.1.Vacuum pumping systems of Chamber-B

Chamber-B is made of stainless steel, has cylindrical shape with 1200mm inner diameter and 3200 mm axial length. The inner surface of Chamber-B is polished to grade #320. Figure 2.2 shows the schematics of Chamber-B. Chamber-B is evacuated from atmospheric pressure to less

than 10 Pa by a dry pump (AA70WN-H, EBARA International Corporation) with an exhaust speed of 116.7 l/s followed by an evacuation to the order of 10^{-3} Pa by a cryopanel cooled below 15 K. For the cooling of cryopanel, a cooling unit consisting of a cryopump (CRYO-U20, exhaust speed: 8200 l/s, ULVAC CRYOGENICS Inc.) and a compressor (C30, ULVAC CRYOGENICS Inc.) were used. The dry pump was operated by an N_2 gas (purity: 99.99%) supply. The dry pump and cryopump were water-cooled by an air-cooled chiller (RKE220Ba-V-G2, ORION Machinery Co., Ltd.). Distilled water was used as a coolant. The dry pump and cryopump were connected to the air-cooled chiller in parallel. The ambient pressure inside Chamber-B is measured as well in Chamber-A. The ultimate pressure of Chamber-B was 1.0×10^{-3} Pa.

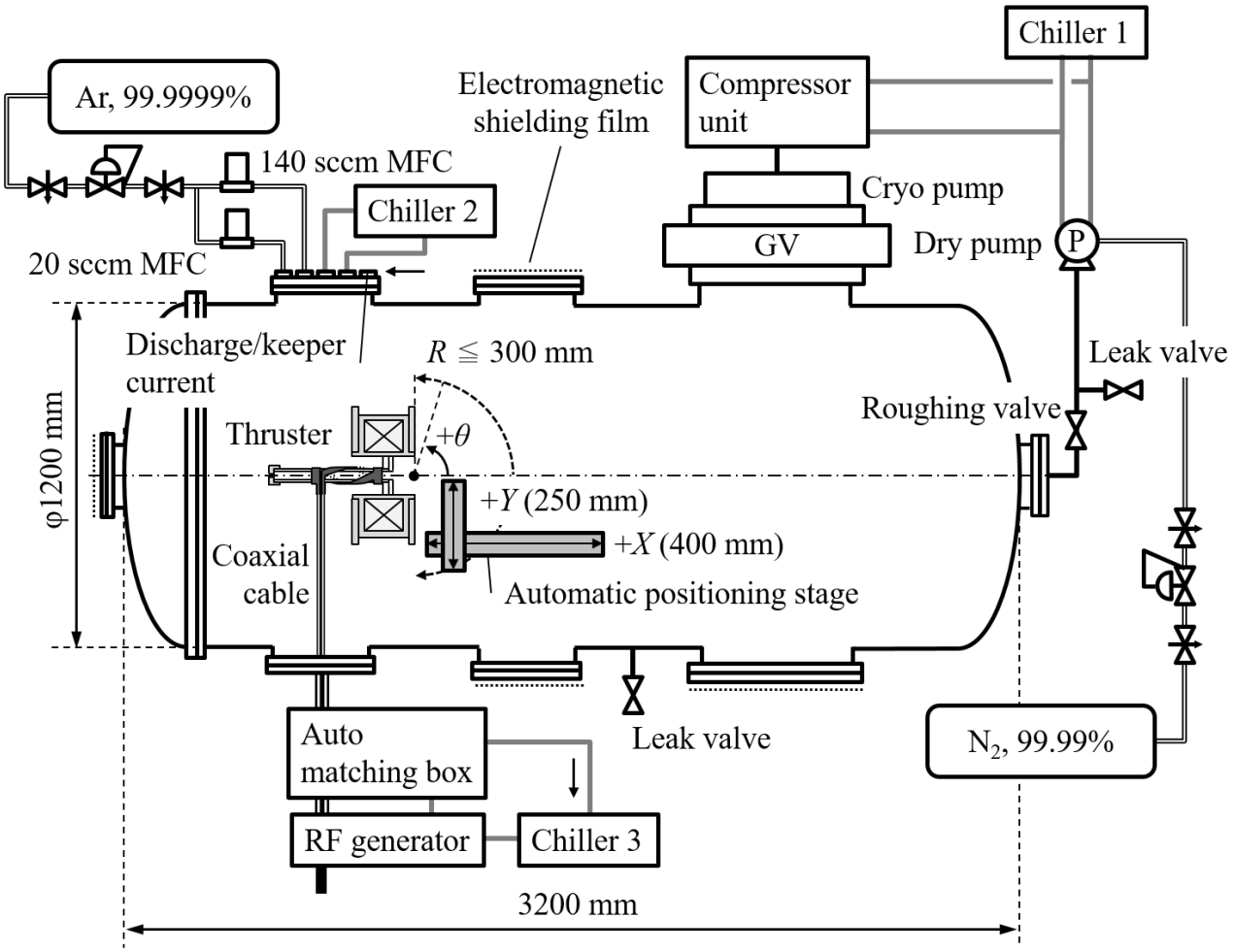

FIG. 2.2 Schematics of Chamber-B.

2.1.2.2.Feed systems of Chamber-B

Similarly to Chamber-A, the flow-rate-controlled propellants were supplied to the thruster and to the hollow cathode. For the controlling of the flow-rate, the same mass flow controllers and controlling units were used as in Chamber-A. However, a mass flow controller with the maximum flow rate of 20 sccm was used for thruster flow-rate controlling.

The thruster operated in Chamber-B equipped with a solenoid coil. For the cooling the solenoid coil, an air-cooled chiller was used (CF1100, cooling capability: 2.9 kW, Yamato Scientific Co., Ltd.). Distilled water was used as a coolant. The cooling water was supplied from the bottom port of the solenoid coil case and flowed out from the upper port.

The specifications of the power supply are summarized in Table 2.2. Electrical power for the main discharge, hollow cathode operation, solenoid coil, and for plasma diagnostics were supplied through a current feed through which located at the side flange of Chamber-B. Chamber-B was electrically grounded for safety, and all view ports had been covered by electromagnetic shielding films. Power supplies for the main discharge, hollow cathode operation, solenoid coil, and plasma diagnostics were all direct current type. For generating radio frequency (RF) plasma, an RF generator (RFK50ZH, frequency; 13.56 MHz, Kyosan Electric Mfg. Co., Ltd.), connected to an automatic impedance matching circuit (MBK50, Kyosan Electric Mfg. Co., Ltd.) was used. By using the auto-matching function, the output RF power from the RF generator and the reflected RF power from the residence circuit were monitored in real time. The RF generator was controlled by a dedicated controller. Both the RF generator and the automatic impedance matching circuits were water-cooled by an air-cooled chiller (CF1100, cooling capacity: 2.9 kW, Yamato Scientific Co., Ltd.). The output RF power was transmitted to the thruster through a 600-mm long coaxial power line. The power line had a 1/4 in. copper core and a 1 in. copper shield sleeve (inner diameter: 22.4 mm). Between the core and the shield there is a dielectric substance made of Teflon. From the value of the relative permittivity of Teflon, the power line has a characteristic impedance of 52 Ω.

Table 2.2 Power supplies used in the experiments in Chamber-B.

Application	CC/CV/RF	Model number	Maker	Specification
Main discharge	CV	N8761A	Keysight Technologies	300 V, 17 A
Hollow cathode discharge	CC	KC8002	Kaufman & Robinson Inc.	800 V, 2 A
Solenoid coil	CC	BC12015	Kaufman & Robinson Inc.	120 V, 15 A
RF generator	RF (13.56 MHz)	RFK50ZH	Kyosan Electric Manufacturing Co., Ltd.	5.0 kW
Plasma diagnostics	CV (bipolar)	NF4520	NF Corporation	± 200 V, ~15 A
	CV	PMC-250-0.25A	Kikusui Electronics Corp.	250 V, 0.25 A
	CV	PWR 800L	Kikusi Electronics Corp.	~80 V, ~80 A

2.1.2.3.Data acquisition systems

All electrical signals were collected by an oscilloscope (DL850, Yokogawa Meters & Instruments Corporation) with plug-in modules (701250, 12 bit resolution, Yokogawa Meters & Instruments Corporation) at a sampling rate of 100 Hz. The discharge voltage was measured with a high voltage probe (P6015A, damping ratio: 1000:1, TEKTRONIX, Inc.) connected in parallel to the discharge circuit. The keeper voltage was calculated based on the monitor signal from the hollow cathode power supply. The discharge current was calculated from the voltage drop on a resistance (10 ± 0.5 mΩ, rated input power: 4 W) connected in series to the discharge circuit. The ambient pressure inside the Chamber-B was recorded by using the monitor signal (linearity: ± 15%) from the ionization gauge.

2.1.2.4.Diagnostics positioning systems

Chamber-B has a traverse system consisting of a two-axis (*X* and *Y*) automatic linear stage and a stepping motor. Figure 2.3 shows the schematic of the traverse system; *X* and *Y* axis of moving directions are also shown. For the *X*- and *Y*- axis motion movements, electrical actuators XA-50L-400 and XA-42L-200 (both made by SUS Corporation) were used. The stroke-length in

X- and *Y*-axis was 400 mm and 200 mm, respectively. The position accuracy was 0.1 mm in both axes. For the controlling of the electrical actuator controlling, dedicated software (XA-PA4, SUS Corporation) was used. On the *Y*-axis stage, a stepping motor (PK56, Oriental Motor Co., Ltd.) with a power unit CRD514-KD was attached for inserting plasma diagnostics probes (see sections 2.3.4 and 2.3.5). The stepping motor was controlled by dedicated software (MEXE02). The accuracy of angular positioning was 0.1 deg. For the support of a plasma diagnostics probe, the stepping motor has a stainless steel L-shaped tube (outer diameter: 8.0 mm, inner diameter: 6.0 mm). The probe axis was oriented parallel to the center axis of the thruster.

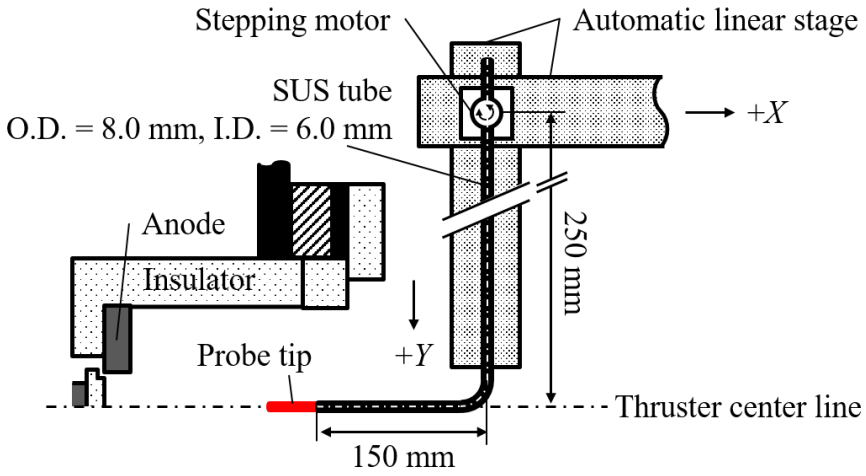

FIG. 2.3 Schematic of the probe traverse system for double and emissive probe measurements.

For the retarding potential analyzer (RPA, see section 2.3.1) and nude Faraday probe (see section 2.3.2) measurements, a swing system consisting of a stepping motor and a 250-mm-lomg stainless steel swing arm was used. Figure 2.4 shows the schematic of the swing system. The center axis of the RPA or nude Faraday probe was adjusted to the same level as the center axis of the thruster by using an aluminum rod.

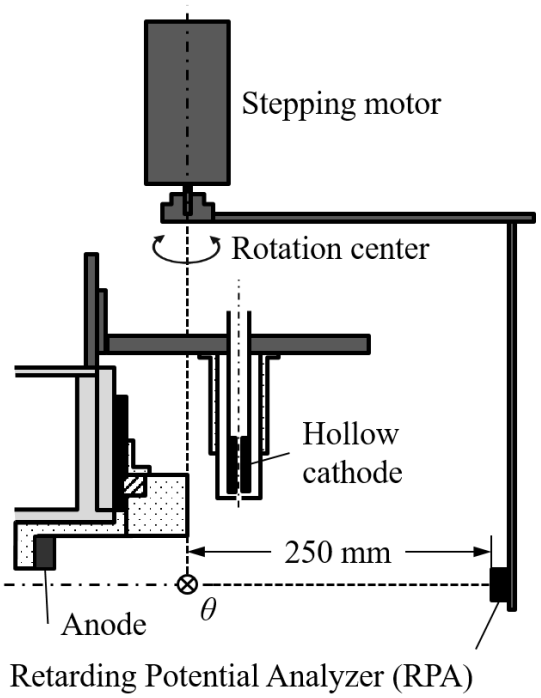

FIG. 2.4 Schematic of the swing system for RPA and nude Faraday probe measurements.

2.2. Thrust stand

A pendulum-type thrust stand of the same type as that of described in Ref. 81, consisting of a stand arm, vacuum bellows, and two bearings, was used to measure the thrust. Figure 2.5 shows the schematic of the thrust stand. The bellows and bearings were assembled on the vacuum chamber flange interfacing between the vacuum and the atmosphere. The radial load exerted to the bearings was compensated by adjusting the vertical position of the bearings under operating conditions, so that the frictional force exerted on the bearings, which degrades the thrust resolution, was effectively eliminated. The stand arm comprised of copper tubes inside its body, through which the cooling water and propellant were supplied. The displacement of the pendulum was amplified by an 1100 mm aluminum arm located outside the chamber and was sensed by a linear variable differential transformer (LVDT) (LVDT1301-2, Shinko Electric Co., Ltd.).

The thrust stand was calibrated using an arrangement of weights, a pulley, and a DC motor under identical vacuum conditions to those of during thruster operations.[82] The DC motor rotated the pulley to change the number of weights for varying the load applied to the thruster. The mass

of the weights was measured by using an electric scale (AW320, SHIMAZU Corporation). As the load was varied, the signal voltage of a differential transformer was measured three times. Figure 2.6 shows a typical calibration curve. The average value for each load was fitted by a least square method and a regression line was obtained. For loads from 0 to 49 mN, linearity was confirmed, with the regression line with a correlation coefficient of 0.997. In this calibration, the effect of the error of the measurement of the mass of the weight on the calibration factor was ± 0.02 mN/V. This corresponds to ± 2.0×10^{-3} mN, which is 0.01% of the thrust range of 26 mN, measured in this study. The thrust stand arm oscillated about the fulcrum with an oil dumper, without a feedback control system. Operating the vacuum pumps and supplying cooling water for the anode and solenoid coil caused vibration of the gauge head of the LVDT with an amplitude of 0.8 mm. Due to this oscillation, the thrust stand resolution was 0.2 mN, which was 0.8% and 5% of the measured maximum and minimum thrust value, respectively.

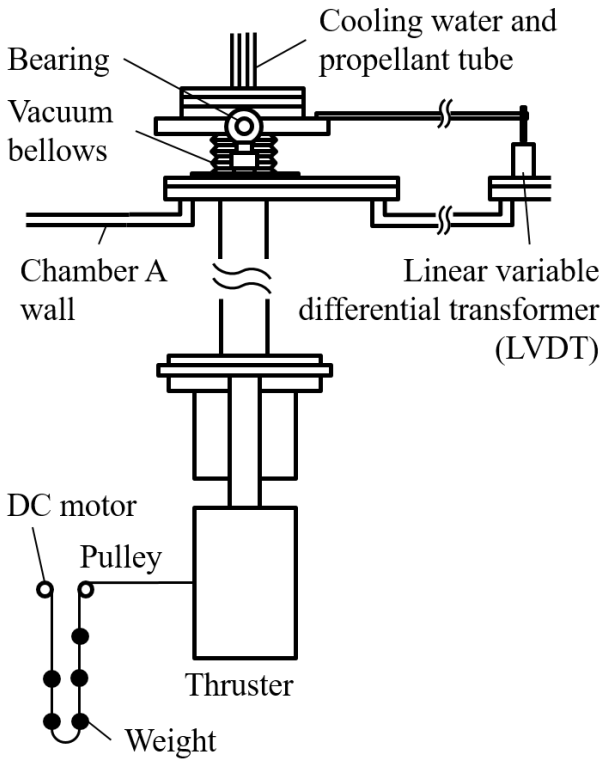

FIG. 2.5 Schematic of the thrust stand with calibration system.

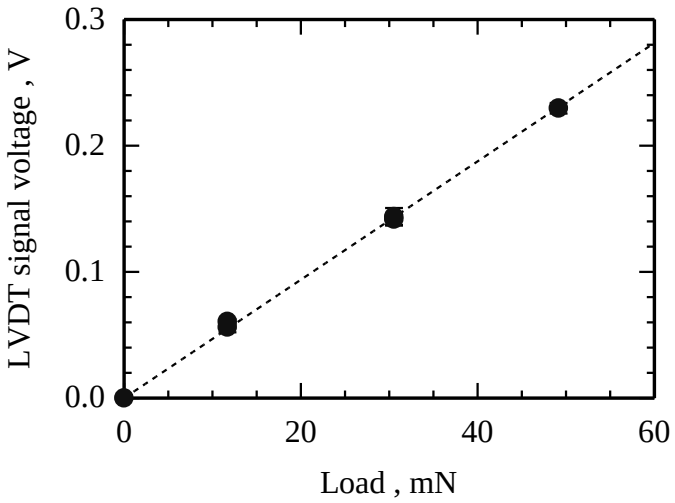

FIG. 2.6 Thrust stand calibration curve; the dependence of the linear differential voltage transfer (LDVT) signal on load.

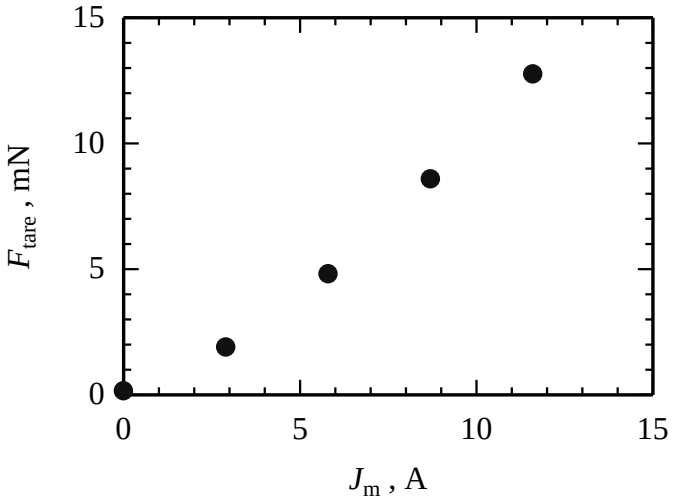

FIG. 2.7 Measured tare force F_{tare} with J_d = 10 A.

The electromagnetic interaction exerts a force on the current loops (tare force, F_{tare}). Figure 2.7 shows the measured F_{tare} with constant J_d of 10 A. To obtain F_{tare}, the thrust was measured while connecting the anode and cathode.

Figure 2.8 shows the typical time history of the LVDT signal. Taking the tare force into account, the thrust F_{exp} was calculated from the following equation:[82]

$$F_{EXP} = F_1 - F_2 - F_{tare}. \tag{2.1}$$

Here, F_1 is the time averaged LVDT signal during the thruster operation and F_2 is that of after the thruster operation.

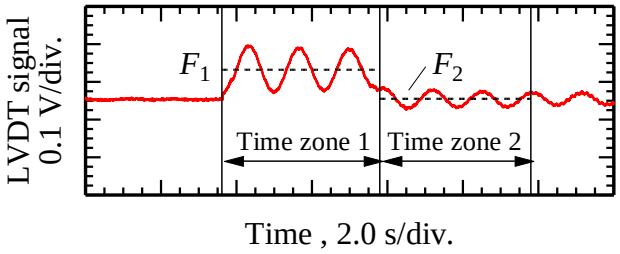

FIG. 2.8 LVDT signal time history. The thruster operates in time zone 1.

2.3. Plasma diagnostics

In order to obtain plasma parameters in the discharge channel and the exhaust plume, plasma diagnostics were conducted as follows.

- Ion energy distribution function (IEDF) and average ion beam energy measurement by a retarding potential analyzer (RPA).
- Integrated ion beam current and ion beam divergence half-angle measurement by a nude Faraday probe.
- Current fractions of each charge-state ion in the exhaust plume by an **E×B** probe.
- Electron number density and electron temperature measurement by a double probe.
- Space potential measurement by an emissive probe.

In this section, each measurement system and parameter calculation procedures are described in detail.

2.3.1. Retarding potential analyzer (RPA)

A retarding potential analyzer (RPA) has metal grid electrodes and works as a high-pass-filter for ion energy.[83] The cut-off energy eV_{RPA} varies as the applied voltage to the grid electrode. The RPA also has an ion collector. Ions that have a larger energy than the cut-off energy can pass through the grid electrodes and collected at the ion collector. If the value of the V_{RPA} and the

collected ion current J_c is known, then the IEDF can be calculated. The kinetic energy of the incoming ion is expressed in Eq. (2.2) by using potential difference V

$$eV = \frac{1}{2} m_i u^2. \tag{2.2}$$

Here, e, m_i, and u are elementary charge, ion mass, and ion velocity in the exhaust direction with the assumption of a one-direction motion. From Eq. (2.2), we have

$$du = \sqrt{\frac{2e}{m_i}} \frac{1}{2} V^{-1/2} dV. \tag{2.3}$$

Using the velocity distribution function $f_u(u)$, J_c is expressed as follows:

$$\begin{aligned} J_c &= en_i A \int_u^\infty u f_u(u) du = en_i A \int_{eV_{RPA}}^\infty \sqrt{\frac{2eV}{m_i}} f_\varepsilon(V) \sqrt{\frac{2e}{m_i}} \frac{1}{2} V^{-1/2} dV \\ &= \frac{e^2 n_i A}{m_i} \int_{eV_{RPA}}^\infty f_\varepsilon(V) dV. \end{aligned} \tag{2.4}$$

Here, n_i is ion number density, A is effective ion collection area, and $f_\varepsilon(V)$ is the IEDF. J_c is composed only ions whose energy is higher than eV_{RPA}. Therefore,

$$\frac{dJ_c}{dV_{RPA}} = -\frac{e^2 n_i A}{m_i} f_\varepsilon(V). \tag{2.5}$$

From Eq.(2.5), IEDF $f_\varepsilon(V)$ is calculated by differentiating J_c with respect to V_{RPA}.

Figure 2.9 shows the schematic of the RPA. It consists of three stainless steel grids (mesh size: 0.28×0.28 mm, blockage ratio: 66%), Photoveel spacers for isolating each of the grids, and a copper ion collector for the measurement of J_c. The RPA cover, which made of stainless steel, was connected to ground. The electric potentials of each grid were applied with respect to the cathode potential. The first grid set to a floating potential. Because the floating potential was lower than the space potential, incoming electrons were repealed. Moreover, the first grid decreased the plasma number density below the first grid to increase the Debye length $\lambda_{D:}$[45]

$$\lambda_D = \sqrt{\frac{\varepsilon_0 k T_e}{e^2 n_e}}. \tag{2.6}$$

Here, ε_0, k, T_e, and n_e are permittivity of vacuum, the Boltzmann constant, electron temperature, and electron number density, respectively. Based on double probe measurements (see section 2.3.4), typical n_e and T_e values around the RPA position were 10^{15} m^{-3} and 5 eV, respectively. Assuming that the sheath thickness is five times larger than the Debye length,[84] the grid size (0.28 mm) is smaller than the sheath thickness (1.25 mm). Therefore, on the second and third grid, the applied voltage infiltrated in the grid space. The second grid was negatively biased to 100 V with respect to the cathode potential by using a direct current power supply (PMC-250-0.25A, Kikusui Electronics Corp.) to repeal electrons. The third grid selected the incoming ions by varying its potential V_{RPA} with respect to the cathode potential. The value of V_{RPA} varied from -20 V up to 440 V in 1 Hz steps, by using a bipolar power supply (NF4520, NF Corporation). The copper ion collector was negatively biased to 30 V with respect to the cathode potential by using a direct current power supply (PWR800L, Kikusui Electronics Corp.). The collected ion current was calculated by using the voltage drop on the connected precision resistance (15 kΩ ± 150 Ω) connected in series.

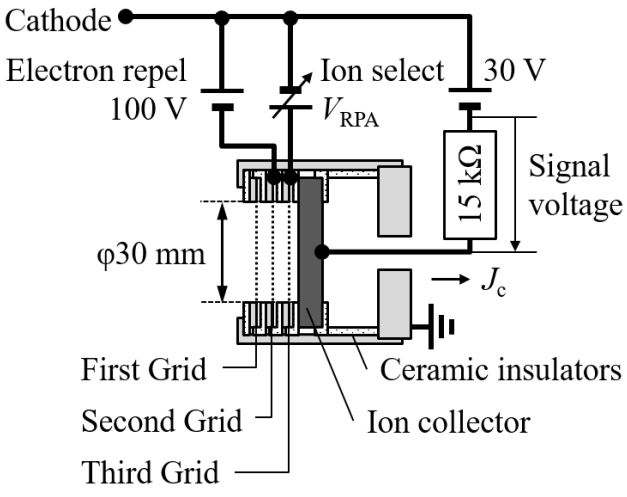

FIG. 2.9 Schematic and electrical circuit of the RPA.

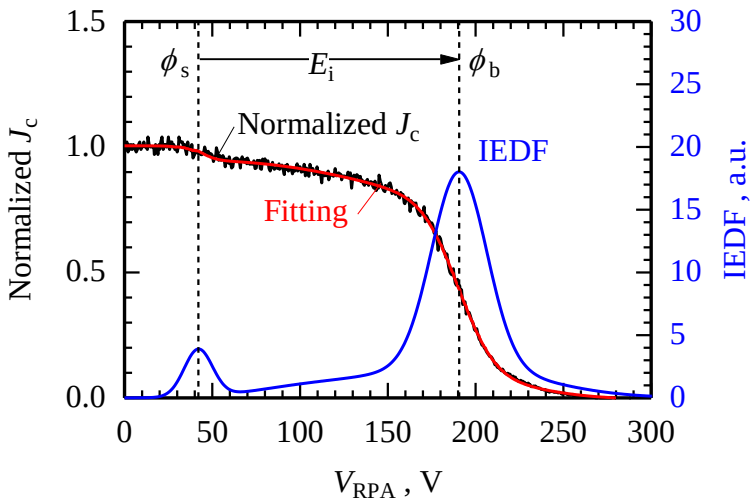

FIG. 2.10 *I-V* characteristics of the normalized ion current J_c –and the voltage V_{RPA} of the RPA's third grid of the RPA measurement (left axis) in V_d = 200 V. The calculated IEDF is also shown (right axis).

Figure 2.10 show a typical current – voltage characteristic of the RPA measurement. The black line shows J_c normalized by an average value in V_{RPA} < 0 V. As shown by the red line, the normalized J_c was smoothly fitted to the superimposed Gaussian function by using a least square method. The IEDF (blue line) was calculated by differentiation of the fitting curve with respect to V_{RPA}. The calculated IEDF had two peaks at $V_{RPA} = \varphi_s$ and $V_{RPA} = \varphi_b$. Because V_{RPA} varied with respect to the cathode potential, the first peak ($V_{RPA} = \varphi_s$) corresponds to the space potential at the position of RPA. The second peak ($V_{RPA} = \varphi_b$) corresponds to the average energy of the accelerated ions by the thruster operation. As shown in Fig. 2.10, both first and second peaks have energy dispersion. The energy dispersion mainly comes from the charge exchange collisions in the exhaust plume[85] or/and ionization position dispersion.[86] For the latter case, the energy dispersion decreases as the propellant flow rate increases.[87] Another possibility is the incident angle of injecting ions to the RPA. Because the RPA oriented perpendicular to the exhaust direction, only the axial component of the kinetic energy of the ions was taken into account. If the injecting ions have an incident angle, the energy of ions will distribute in the low-energy region. As shown in Fig. 2.10, there are ions that have a higher energy than the discharge voltage (in the case shown in Fig. 2.10, the discharge voltage was 200 V). However, quantitatively identifying the origin of

the dispersions is difficult and the dispersions are also affected by facility-induced collisions.[87] Because of the facility-induced effects, quantitative investigation of the dispersions is meaningless. In this dissertation, the ion beam energy, for characterizing the experimentally-measured ion beam energy distribution without quantifying the dispersions, is defined as:

$$E_i \equiv \varphi_b - \varphi_s. \tag{2.7}$$

2.3.2. Nude faraday probe

To measure the integrated ion beam current J_i and the ion beam divergence half-angle $<\theta>$, a nude Faraday probe[88,89] was used. Figure 2.11 shows the schematic of the nude Faraday probe. The nude Faraday probe has an ion collector part on its center and a coaxially guard ring. Both the ion collector part and the guard ring were made of copper. The ion collector has a circular shape with a diameter of 12 mm and the guard ring has an inner diameter of 13 mm and an outer diameter of 23 mm. The gap between the ion collector part and the guard ring was 0.5 mm. Both the ion collector part and the guard ring was negatively biased to 50 V by using a direct current power supply (PWR800L, Kikusui Electronics Corp.) with respect to the cathode potential to collect ions and repeal electrons. The Faraday probe is surrounded by an ion sheath. In practice, the effective ion collector area is not equal to the plasma-exposed area of the ion collector part, because of the sheath-edge effect. The guard ring suppresses the sheath-edge effect. As the sheath thickness is 1.0 mm (see section 2.3.4), a plane and uniform sheath can be formed in front of the ion collector part, because the gap is smaller than the sheath thickness. As a result, the effective ion collection area equals to the plasma-exposed area of the ion collector part.[90]

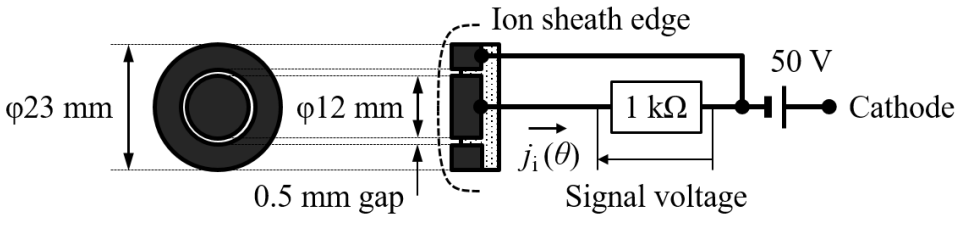

FIG. 2.11 Schematic and electrical circuit of the nude Faraday probe.

The nude Faraday probe was installed on the swing system (see Fig. 2.4) and the swing to the azimuthal direction in the horizontal plane on the axis. Here, angle θ is defined with respect to the center axis of the thruster (see Fig. 2.2). The swing radius R was set to 250 mm and θ ranged from -π/2 to π/2. With varying θ, the ion current was calculated based on the voltage drop on a resistance (1 kΩ) connected in series. An ion current density at angle θ, $j_i(\theta)$ was calculated by dividing the measured current by the ion collector part area. Figure 2.12 shows a typical ion current density j_i dependence on the rotation angle θ. Assuming that the exhaust plume is axisymmetric, the integrated ion beam current J_i can be calculated as

$$J_i \equiv \pi R^2 \int_{-\pi/2}^{\pi/2} j_i(\theta)|\sin\theta| d\theta \big/ (1+\gamma). \tag{2.8}$$

Here, a secondary electron emission is taken into account. The secondary electron emission coefficient γ for single ionized argon impact, with less than 1.0 keV incident energy is 0.05 – 1.2 for the Ar^+ – Cu impact.[91] The ion beam divergence half-angle $<\theta>$ is calculated by Eq. (2.9):[92]

$$\langle\cos\theta\rangle \equiv \frac{\int_{-\pi/2}^{\pi/2} j_i(\theta)|\sin\theta|\cos\theta d\theta}{\int_{-\pi/2}^{\pi/2} j_i(\theta)|\sin\theta| d\theta}. \tag{2.9}$$

In each operating condition, $j_i(\theta)$ was measured at least twice in both from the -π/2 to π/2 direction and the π/2 to -π/2 direction. The following figure about J_i and $<\theta>$; an average values of each trial and their standard deviation are shown in symbols and error bars, respectively.

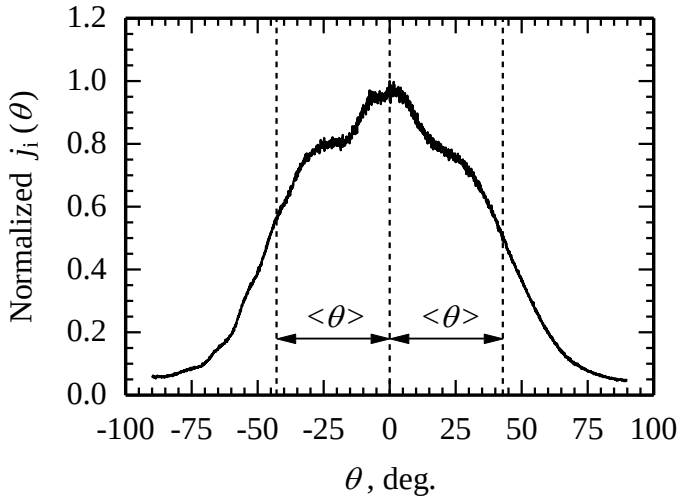

FIG. 2.12 Dependence of the normalized ion current density j_i on rotation angle θ.

2.3.3. E×B probe

To calculate the current fractions of each charge-state ion, an **E×B** probe was used. The **E×B** probe works as a band-pass filter for the velocity of incoming ions.[93] Ions that have a velocity within the specific range can pass through the electromagnetic field applied in the **E×B** probe, and are collected as ion current $J_{\mathbf{E\times B}}$. Figure 2.13 shows the schematics of the **E×B** probe. The **E×B** probe is composed of an entrance collimator, an **E×B** deflection section, an exit collimator, and a copper ion collector. The **E×B** deflection section selects ions based on their incoming velocity and both the entrance and the exit collimators enhance the selection accuracy. In the **E×B** deflection section, a uniform magnetic field *B* is applied by a permanent magnet and a soft iron yoke. A set of electrodes, with inter-electrode distance *d* apply an electric field *E*, perpendicular both to the magnetic field and exhaust velocity.

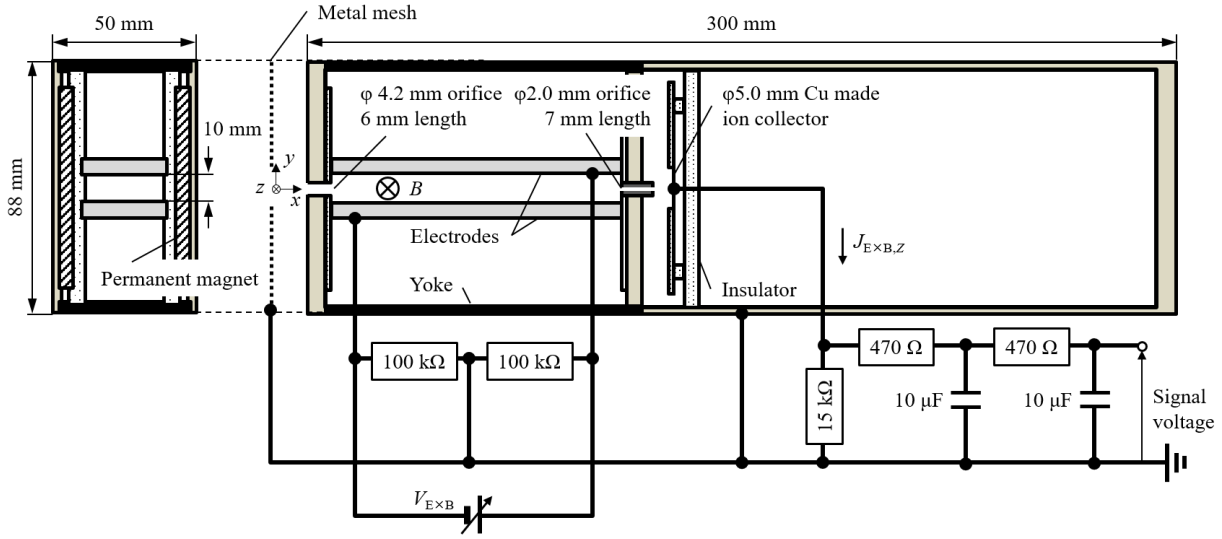

FIG. 2.13 Schematic and electrical circuit of the **E×B** probe.

The working principle of the **E×B** probe is as follows.[93] **E**, **B**, and ion velocity ***u*** are defined in a rectangular coordination system. Here, **E** and **B** are uniformly applied inside the **E×B** deflection section in one direction only:

$$\mathbf{E} = \begin{bmatrix} 0 \\ E_y \\ 0 \end{bmatrix}, \quad \mathbf{B} = \begin{bmatrix} 0 \\ 0 \\ B_z \end{bmatrix}, \quad \mathbf{u} = \begin{bmatrix} u_{\mathrm{i},Z} \\ 0 \\ 0 \end{bmatrix} \tag{2.10}$$

Here, E_y, B_z, and $u_{\mathrm{i},Z}$ are the y-axis component of **E**, z-axis component of **B**, and the Z-charged ion velocity, respectively. In this experiment, the charge state Z is a positive integer. For moving a single ion of charge state Z, the equation of motion is

$$m_{\mathrm{i},Z} \frac{d\mathbf{u}}{dt} = eZ\left(\mathbf{E} + \mathbf{u} \times \mathbf{B}\right). \tag{2.11}$$

Here, $m_{\mathrm{i},Z}$ is the mass of the Z-charged ion. Substituting Eq. (2.10) into Eq. (2.11), we get

$$m_{\mathrm{i},Z} \frac{du_x}{dt} = eZ\left(E_y + u_{\mathrm{i},Z} \times B_z\right). \tag{2.12}$$

For the ion to move through the **E×B** deflection section linear motion of a velocity of $u_{\mathbf{E}\times\mathbf{B}}$, the right-hand-side of Eq. (2.12) needs to be zero.

$$eZ\left(E_y + u_{\mathbf{E}\times\mathbf{B}} \times B_z\right) = 0.$$

$$u_{\mathbf{E}\times\mathbf{B}} = -\frac{E_y}{B_z} = -\frac{V_{\mathbf{E}\times\mathbf{B}}}{B_z d}. \tag{2.13}$$

Here, $V_{\mathbf{E}\times\mathbf{B}}$ is a relative voltage difference between the two electrodes. Therefore, in the $u_{\mathrm{i},Z} \neq u_{\mathbf{E}\times\mathbf{B}}$ case, the trajectory of the ion depends on the magnitude of the correlation between u_x and $u_{\mathbf{E}\times\mathbf{B}}$. If $u_{\mathrm{i},Z} < u_{\mathbf{E}\times\mathbf{B}}$ is satisfied, the electrostatic force, represented by $eZ\mathbf{E}$ in Eq. (2.11), is larger than the Lorentz force, $eZ(\mathbf{u} \times \mathbf{B})$in Eq. (2.11). In this case, the ion is deflected towards the negative potential side of the electrode. On the other hand, in the $u_{\mathrm{i},Z} > u_{\mathbf{E}\times\mathbf{B}}$ case, the Lorentz force is larger than the electrostatic force, and the ion is deflected towards the positive potential side of the electrode. Because $B_z d$ = const. in Eq.(2.13), $u_{\mathbf{E}\times\mathbf{B}}$ depends only on $V_{\mathbf{E}\times\mathbf{B}}$. In principle, assuming a collision-less motion inside the **E×B** probe, only the ions that satisfy $u_{\mathrm{i},Z} = u_{\mathbf{E}\times\mathbf{B}}$ can pass through the **E×B** deflection section. The expected $J_{\mathbf{E}\times\mathbf{B}}$ is

$$J_{\mathbf{E}\times\mathbf{B}} = \sum_Z eZn_{\mathrm{i},Z} u_{\mathbf{E}\times\mathbf{B}} A = \sum_Z eZn_{\mathrm{i},Z} \frac{V_{\mathbf{E}\times\mathbf{B}}}{B_z d} A. \tag{2.14}$$

Here, $n_{i,Z}$ is the number density of Z-charged ions and A is the effective ion collection area. From Eq. (2.14), $J_{\mathbf{E}\times\mathbf{B}}$ varies with $V_{\mathbf{E}\times\mathbf{B}}$. From the $J_{\mathbf{E}\times\mathbf{B}} - V_{\mathbf{E}\times\mathbf{B}}$ characteristics, the effective acceleration voltage of a Z-charged ion $V_{a,Z}$ can be calculated.[94,95] From the conservation law of energy, the incoming velocity $u_{i,Z}$ relates to $V_{a,Z}$ as

$$u_{i,Z} = \sqrt{\frac{2eZV_{a,Z}}{m_{i,Z}}}. \tag{2.15}$$

In the $u_{i,Z} = u_{\mathbf{E}\times\mathbf{B}}$ condition,

$$V_{\mathbf{E}\times\mathbf{B}} = B_z d\sqrt{\frac{2eZV_{a,Z}}{m_{i,Z}}}. \tag{2.16}$$

From Eq. (2.16), $V_{a,Z}$ of each charged states can be calculated.

All dimensions of the entrance collimator, the **E×B** deflection section, and the exit collimator are determined by the ion trajectory simulation[96] using Eq. (2.11). In practice, due to the finite orifice diameter of both the entrance and exit collimators, all the ions with a specific velocity, which depending on the dimensions of the collimators can pass through the **E×B** deflection section. Moreover, if ions have an incident angle with respect to the axis of the **E×B** probe center, the accuracy of ion selection also depends on the axial length of the collimators. Decreasing the orifice diameter and increasing the collimator length improve the ion selection accuracy. However, at the same time, the signal-to-noise ratio of the $J_{\mathbf{E}\times\mathbf{B}}$ measurement is deteriorated. In this experiment, the entrance collimator and the exit collimator have a 4.2 mm dia. orifice with a length of 6 mm and a 2.0 mm dia. orifice with a length of 7 mm, respectively. The length of the **E×B** section is 110 mm and the inter-electrode distance d was set to 10 mm. The ion collector which, with a 5-mm-diameter effective collection area was set 8 mm axially below the exit of the exit orifice. The relative potential of the electrodes can be varied from 0 to 100 V by using a voltage applying system, containing a set of function generators (SG-4322, IWATSU Electric Co., Ltd.) and a power amplifier (NF4520, NF Corporation). Two resistances with 100 kΩ were connected in parallel to the voltage applying system to keep the space potential at the center of the two

electrodes to ground. $J_{\mathbf{E}\times\mathbf{B},Z}$ is calculated from the voltage drop on a 15 kΩ resistance, through a second order low-path filter with a cutoff frequency of 33 Hz.

Figure 2.14 shows a typical current – voltage characteristic of the **E×B** probe measurement. The measured $J_{\mathbf{E}\times\mathbf{B},Z}$ is normalized by its peak value. The normalized $J_{\mathbf{E}\times\mathbf{B},Z}$ fit smoothly to the superimposed Lorentzian functions, using the least squares method. In Fig. 2.14, these are two peaks and each peak corresponds to a singly-charged ion (Z = 1, red dashed line) and doubly-charged ion (Z = 2, blue dashed line). The obtained current fractions of each charge-state ion are based on the peak height ratio.[97] The secondary electron emission[91] is taken into account. In the case shown in Fig. 2.14, the current fractions of singly-charged ion and doubly-charged ion are 76% and 24%, respectively.

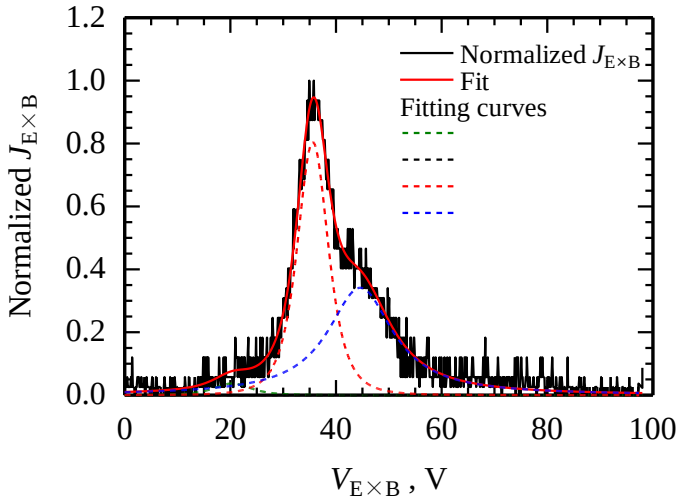

FIG. 2.14 Dependence of the normalized ion current $J_{\mathbf{E}\times\mathbf{B},Z}$ on the swing voltage $V_{\mathbf{E}\times\mathbf{B}}$ of the **E×B** probe measurement.

2.3.4. Double probe

To measure the electron number density n_e and the electron temperature T_e, a double probe[98] was used. Figure 2.15 shows the schematic of the double probe. In the plasma collection part, a tungsten wire with a diameter of 0.3 mm and with an effective length of 3 mm was used. The distance between two wires is 2.2 mm. Each wire is held inside a single bore mullite tube, connected to a larger double bore alumina tube. The double tier design is used for the cross section

of the probe in order to decrease the discharge perturbation. The double bore alumina tube is held by a stainless tube, connected to the probe traverse system (see section 2.1.2.4). The voltage difference between two wires was varied in 10 Hz steps, by using the same bipolar power supply, which was used for the RPA (see section 2.3.1). A current I in the wires was calculated by using the voltage drop on a resistance connected in series.

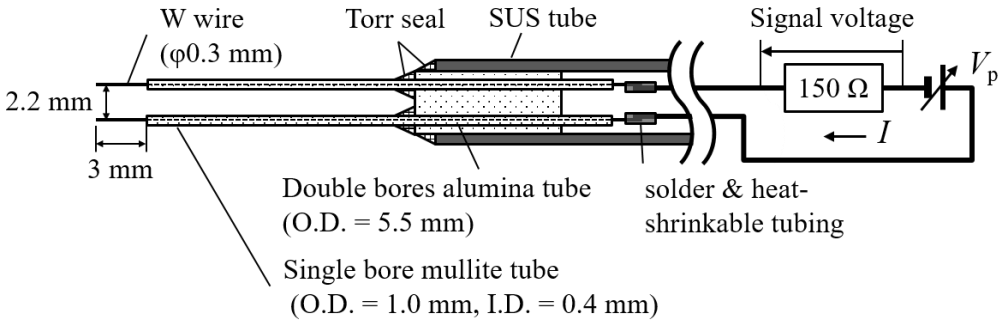

FIG. 2.15 Schematic of the double probe and electrical circuit.

Figure 2.16 shows a typical $I - V$ characteristic of the current and voltage V_p of the double probe measurement. The value of V_p was varied in 10 Hz steps. The n_e and T_e calculation procedure were as follows.[99] As shown in Fig. 2.16, the measured I is fitted to a hyperbolic tangent curve (red line) for a symmetric cylindrical double probe, with Eq. (2.17) incorporating the least square method:

$$I = I_{sat} \tanh\left(\frac{V_p}{2kT_e/e} \right) + c_1 V_p + c_2 . \tag{2.17}$$

In Eq. (2.17), the ion saturation current I_{sat}, the electron temperature T_e, coefficients c_1 corresponding to sheath expansion in the ion saturation region and c_2 corresponding to any offset current due to stray capacitance, are all calculated as fitting parameters. It is noted that the electron energy distribution function is possibly a bi-Maxwellian distribution due to the beam current from the hollow cathode. However, double probe cannot obtain the low energy distribution temperature, because they are limited to collecting the high-energy tail of the electron energy distribution.

Therefore, the presented T_e value is spuriously assumed that the plasma contains single temperature corresponding to the higher energy distribution owing to this restriction. From I_{sat} and T_e, n_e is calculated from Eq. (2.18), using Bohm approximation[100] for the ion velocity:

$$n_e = \frac{I_{sat}}{\kappa A_s}\sqrt{\frac{m_i}{kT_e}}. \tag{2.18}$$

Here, κ (= 0.61) is the density decrement inside the pre-sheath and A_s is electrode collection area. The effective collection area depends on the sheath surrounding the wires. By using T_e and n_e, the Debye length λ_D can be calculated from Eq. (2.18). The sheath thickness δ is then calculated according to[84]

$$\frac{\delta}{\lambda_D} \approx \frac{2}{3}\left[\frac{2}{\exp(-1)}\right]^{1/4}\left[\sqrt{-\frac{1}{2}\ln\left(\frac{m_e}{m_i}\right)}-\frac{1}{\sqrt{2}}\right]^{1/2}\left[\sqrt{-\frac{1}{2}\ln\left(\frac{m_e}{m_i}\right)}+\sqrt{2}\right]. \tag{2.19}$$

By using the probe radius r_p and the probe exposed area A_p, A_s follows from Eq. (2.20)[99] as,

$$A_s \approx A_p\left(1+\frac{\delta}{r_p}\right). \tag{2.20}$$

Substituting Eq. (2.20) into Eq. (2.18), a new n_e can be calculated from this new effective collection area and this process is iterated until convergence.

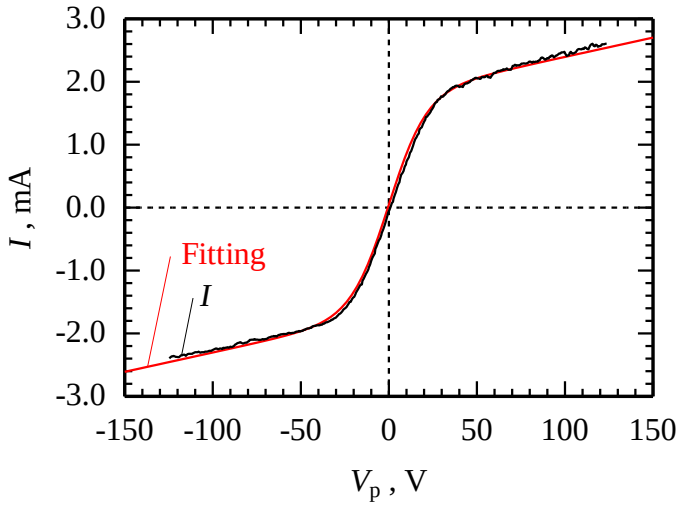

FIG. 2.16 Current I – voltage V_p characteristic of the double probe measurement.

2.3.5. Emissive probe

To measure the space potential V_s, an emissive probe[101] was used. The principle of the measurement of space potential is as follows. In plasma, the electric potential of a floating object V_f is lower than the space potential for adjusting the net current to zero. When an object is heated, thermionic electrons are emitted from the surface of the object. As a result, the floating potential moves towards the space potential. However, because of the space-charge effect, V_f obtained by the emissive probe is lower than V_s.[102] The measured V_f value was corrected by a factor of $\psi_c kT_e/e$[103] as

$$V_s = V_f + \psi_c \, kT_e/e. \tag{2.21}$$

The correction factor ψ_c depends on the Debye length to the filament radius ratio, and it varies between $0 < \psi_c < 1.5$ for argon gas. Figure 2.17 shows the schematic of the emissive probe. The electron emission part is made of a 1%-thoriated tungsten wire bent to a 2.0-mm-dia semicircle. The diameter of the wire is 0.185 mm and held by a single bore mullite tube, connected to a larger double bore alumina tube. In general, the electron emission part is Joule heated, by supplying a heater current J_h to emit sufficient amount of thermionic electrons.[104]

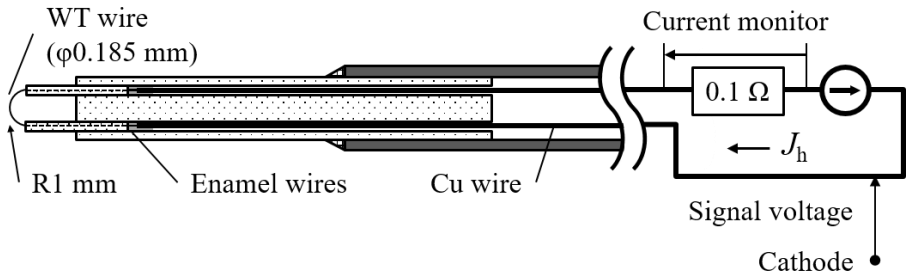

FIG. 2.17 Schematic of the emissive probe and electrical circuit.

Figure 2.18 shows the dependence of the floating potential V_f on the heater current J_h at two different positions on the central axis; the anode inlet (red symbol) and the thruster exit (black symbol). In the $J_h \leq 4.5$ A case, V_f is kept constant. As J_h increases above 4.5 A, V_f increases

rapidly and saturates in the case of $J_h \geq 5.5$ A. For the measured V_f the $J_h \geq 5.5$ A case is used, and J_h is kept above 5.5 A during the floating potential measurement.

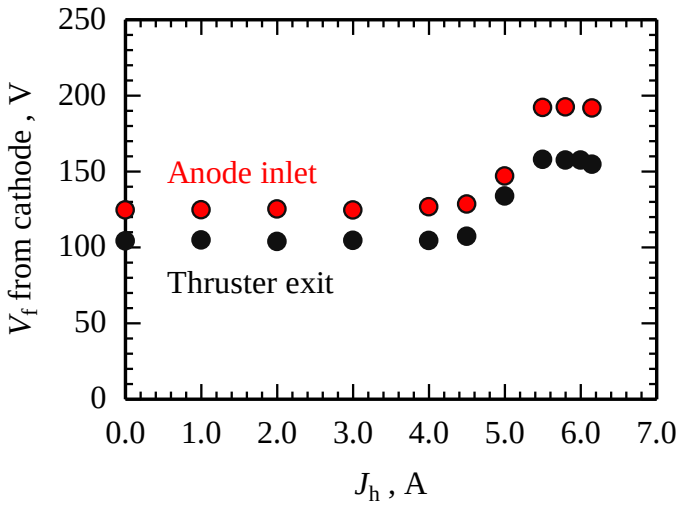

FIG. 2.18 Dependence of the floating potential V_f on heater current J_h at two different positions on the central axis; the anode inlet (red symbol) and the thruster exit (black symbol).

2.3.6. Error analysis in double probe and emissive probe experiments

In particular, introducing probes into a bulk plasma may cause non-negligible perturbations to the thruster discharge.[105,106] The disturbances influences the thruster operation characteristics and plasma properties, especially around the probe location. The former effects can be characterized by the discharge current J_d. Figure 2.19 shows the measured J_d at each double probe measurement positions, z_{probe}, at r_{probe} = 0 and 10 mm in a Type A magnetic field (see, Fig.5.2). The cylindrical coordinate definition is described in section 5.2. By inserting the double probe in the downstream region (z_{probe} > 115 mm), the difference in the values of J_d with and without the double probe operation was smaller than 2%. The difference in J_d was largest, up to 12% (absolute value), at z_{probe} = 0 mm, then decreased lowering its location. In 30 mm < z_{probe} < 115 mm, the highest difference in J_d was 7%. The insertion of the probe influences the plasma properties, as Staack et al.[107] reported that due to the secondary electron emission from probe body, inserting the probe causes the decrement of the electron temperature. However, in this dissertation, the data

for quantitative validation of the secondary electron emission effect did not obtained. The electron number density has a weak dependence on the electron temperature (see Eq. (2.18)). In the ionization and acceleration region, the space potential exceeded 100 V and several electron volts of uncertainty in electron temperature does not change the distribution of the space potential; in Eq. (2.21), V_s is much larger than $\psi_c kT_e/e$. The value of T_e presented in this dissertation can be underestimated, however, this decrement do not have a significant effect on the distribution of plasma parameters.

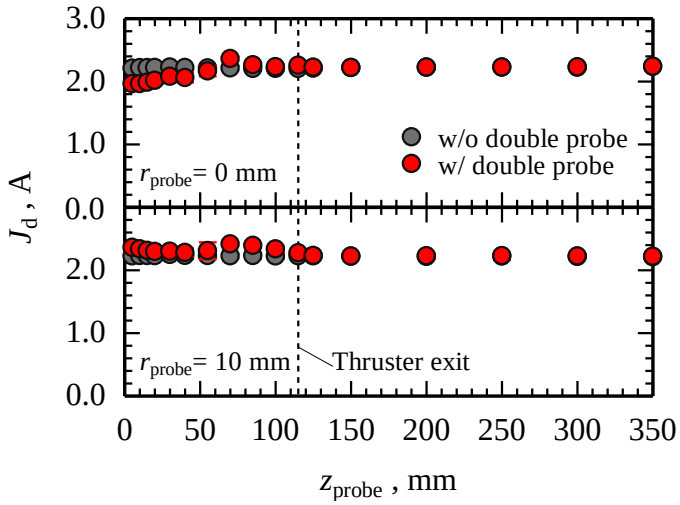

FIG. 2.19 Probe perturbation distributions on J_d at two different radial positions r_{probe}.

Because the double probe and the emissive probe are used in floating voltage, the dominant influence of the probe insertion depends on the sheath thickness as calculated by Eq. (2.19). From the electron number density and electron temperature measurements at r_{probe} = 0 mm in the case shown in Fig. 2.19, λ_D varied between 0.02 – 0.05 mm and therefore, the sheath thickness is 0.1 – 0.25 mm. As shown in Fig.2.19, the variation of J_d is the largest when the probe was inserted at z = 0 mm. At this point, δ equaled to 0.1 mm and the effective probe diameter $2(r_p + \delta)$ is 0.5 mm. Inside the ring anode, a double probe measurement point was set at every 2 mm. Because the effective probe diameter was smaller than the measurement point interval, the insertion of the probe influenced the local plasma properties and the measured parameter distributions were

limited. In addition to the plasma disturbances, n_e, T_e, and V_s measured by probe diagnostics had uncertainties. Large combinations of effects are contributed to into the uncertainties: the uncertainty of the electrode collection area,[108] finite ion temperature,[109] noise in the collected signal, and the applicability of the probe theory.[99] As mentioned above, I_{sat} and T_e are determined directly as fitting parameters in Eq. (2.17). The standard deviation of the fitting of T_e was up to 15%. The uncertainty of n_e is due to combinations of uncertainties of each parameter in Eq. (2.18), i.e. the standard deviation of the I_{sat} fitting, the finite ion temperature effect on κ, accuracy of A_{eff}, due to probe manufacturing, and uncertainty in T_e. Applying the laws of error propagation in Eq. (2.18), the estimated uncertainty in n_e was +13/-16%. From Eq.(2.21), the uncertainty of V_s is in the same order as the uncertainty of T_e. However, Eq (2.21) neglects the potential drop in the pre-sheath region.[110] In the typical operation condition of a Hall thruster, the pre-sheath thickness is comparable to the discharge channel width, i.e. 20 mm.[46] This is comparable to the inner diameter of the ring anode. Moreover, heating current flows in the emission probe causes a 4.5 V potential drop in the emission part. Therefore, the uncertainty of V_s is $+0.3(kT_e/e)/-0.9(kT_e/e) \pm 2.25$ V.

3.

High impedance electromagnetic acceleration in diverging magnetic field by using hollow cathode

3.1. Thermionic electrons for electric arc

In arc discharge, the major charge carrier is thermionic electrons. Previous studies used a rod cathode made of thoriated tungsten. Using a conventional rod cathode, a discharge current of the order of 10^2 to 10^4 A was necessary to increase the cathode surface temperature forcibly to obtain thermionic electrons for maintaining arc discharge.[111] Myers et al.[112] measured the cathode surface temperature. With 12 mg/s of nitrogen as a propellant and 875 A of discharge current, the surface temperature on the 2% thoriated tungsten rod cathode reached more than 3000 K. This high temperature operation could cause severe cathode erosion and shorten the thruster lifetime. In quasi-steady operation, the cathode surface temperature is typically low (with an average temperature < 1000 K) and spotty arc attachment occurs.[113] This increases the local surface temperature of the cathode, resulting in a much higher erosion rate.[114] Such cold cathode conditions also occur during the startup phase of steady-state operation, until the surface temperature becomes sufficiently high for thermionic electron emission.

As mentioned in section 1.2, high impedance operation is a promising method to utilize input power efficiently. However, unless using the conventional rod cathode, high impedance operation cannot be achieved. In this study, a thermionic electron emission-type hollow cathode was used in order to supply the thermionic electrons for sustaining a direct-current discharge in steady-state Af-MPD thruster. Before starting the main discharge, the hollow cathode has been ran with a

small propellant flow rate of approximately 0.2 mg/s and a keeper current of 2.0 A. Steady-state thruster operation was achieved at a discharge current level of up to 20 A, which is 10 to 1000 times lower than that of previous studies, while obtaining competitive thrust performance.

3.2. Applied-field MPD thruster using hollow cathode

In this chapter, a hollow cathode was utilized as a discharge cathode in Af-MPD thruster and demonstrated the high impedance, direct current discharge in diverging magnetic field with up to 265 mT of strength.

Figure 3.1 shows a diagram of the axisymmetric-type Af-MPD thruster. The thruster head comprises an axisymmetric anode, a hollow cathode on the central axis, insulators, and a solenoid coil. The anode is cylindrically shaped and made of copper, with the inner diameter varying from 52 mm to 80 mm in a conical transition. The hollow cathode (shown in Fig.3.2) consists of a commercial emitter made of Tantalum[115] (LHC-03AE1-01, Kaufman & Robinson Inc.), and its keeper electrode has a 2.0 mm diameter orifice. The solenoid coil applies the external magnetic field. Magnetic field strength distribution was measured using a Gauss meter (GM-4000, Denshijiki Industry Co. Ltd.). On the thruster axis, the maximum magnetic field strength was measured to be 265 mT at the center of the coil, and 103 mT at the exit of the anode. One flow channel inside the emitter and two outside flow channels at 11 mm off-axis (Fig.3.2 shows only one of the two outside flow channels) inject propellant into the discharge channel. The propellant mass flow rate through the hollow cathode is designated by $\dot{m}_1$, and that through two off-axis supply channels by $\dot{m}_2$. In this chapter, z designates the axial position originating at the anode exit. The position of the hollow cathode tip, z_c, was set either at the anode exit (z_c = 0 mm) or 105 mm upstream from the anode exit (z_c = -105 mm). The center of the solenoid coil was set at z = -80 mm. The anode and solenoid coil were water-cooled and could maintain steady operation at up to 6 kW.

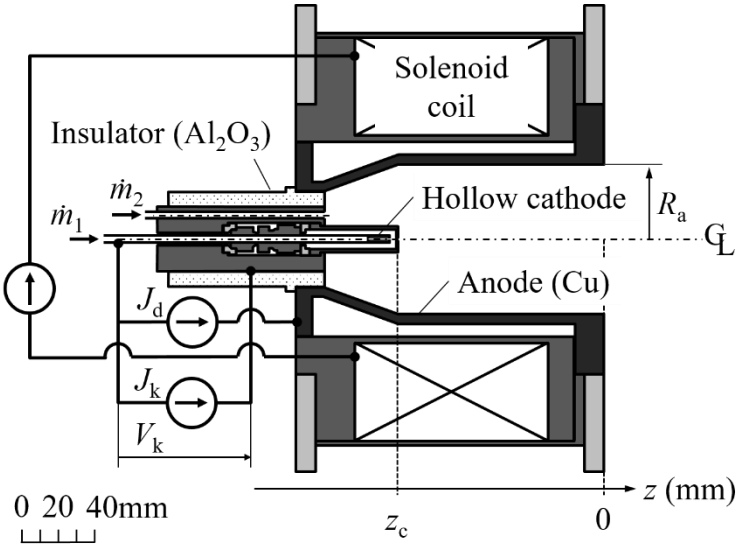

FIG. 3.1 Cross-sectional view and circuit diagram of axisymmetric Af-MPD thruster.

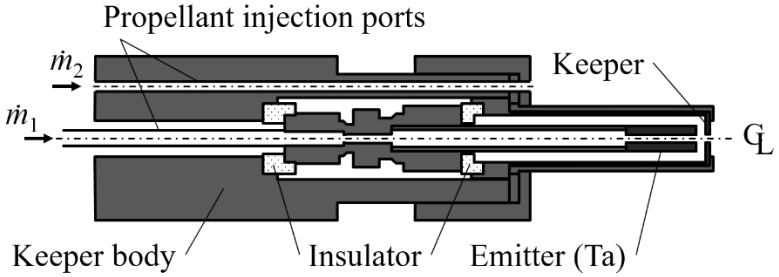

FIG. 3.2 Cross-sectional view if hollow cathode.

3.3. Discharge characteristics in diverging magnetic field

3.3.1. Operating range identification

All experiments in this chapter were conducted in Chamber-A. Table 3.1 summarizes the operating conditions used in these experiments. In the table, $\dot{m}$ represents the total propellant mass flow rate, $\dot{m} \equiv \dot{m}_1 + \dot{m}_2$. The representative value of the applied magnetic field, $\overline{B}$, is equal to the value at the coil center. The values for thrust F, discharge voltage V_d, and keeper voltage V_k were measured, while $\dot{m}_1$, $\dot{m}_2$, J_d, $\overline{B}$ and z_c were variable control parameters. As shown in Fig. 2.8, the thruster was operated at least for 4 s before turning off the discharge current. During this time, the ratio of the root mean square (RMS) of discharge current to the time averaged value was also evaluated. In this study, when this ratio was less than 10%, the operation was categorized as

"stable". The uncertainties obtained for $\dot{m}$, J_d, $\overline{B}$, R_a, and measured V_d were ± 6.2×10^{-2} mg/s, ± 51 mA, ± 10 mT, ± 0.1 mm, and ± 2.0 V, respectively. In the following figures in which experimental results are plotted, the symbol represents the time-averaged value, and the error-bar represents the RMS with a 68% confidence interval.

Table 3.1 Operating conditions.

Parameter, unit	Unit	Value
$\dot{m}_1$	mg/s	0.83 – 2.10
$\dot{m}_2$	mg/s	0 – 3.10
$\dot{m}$	mg/s	0.83 – 3.90
J_d	A	10 – 20
$\overline{B}$	mT	133 – 265
R_a	mm	40
z_c	mm	0 – 105

Zhurin et al.[116] presented the operating characteristics of an axisymmetric-type MPD thruster with applied magnetic field (they named it a "high-current end-Hall thruster") and with a discharge current of up to 8 kA, in which the self-field thrust was treated as the dominant thrust component. They used the flow Mach number, the ratio of the self-field thrust to the gas-dynamic thrust, and the ratio of flow velocity to **E**×**B** drift velocity as dimensionless, characteristic quantities. Their formulae contain a term proportional to J_d^2 for the self-field thrust and another term for the gas-dynamic thrust. However, as will be shown in the following discussions, their formulae do not apply to the present thruster performance because these terms are negligible in this study. In contrast, in an axisymmetric-type Af-MPD thruster, if the swirl acceleration is dominant, the thrust is proportional to the radius of the acceleration region.[117] The characteristic applied-field thrust, F_A, is expressed by the following equation:

$$F_A \equiv J_d \overline{B} R_a . \tag{3.1}$$

On the other hand, the self-field thrust[44] is characterized by the following equation:

$$F_S \equiv \mu_0 J_d^2 . \tag{3.2}$$

Based on Eqs. (3.1) and (3.2), the ratio α of the applied-field to self-field thrust, which is a representative values of operating conditions in an acceleration region, is given by

$$\alpha \equiv \frac{J_{\mathrm{d}} \bar{B} R_{\mathrm{a}}}{\mu_0 J_{\mathrm{d}}^2} = \frac{\bar{B} R_{\mathrm{a}}}{\mu_0 J_{\mathrm{d}}}. \tag{3.3}$$

In order to obtain real thrust components, F_{A} and F_{S} should be multiplied by their respective, effective factors. However, α still represents the relative contribution of an applied to self-magnetic thrust because its order of magnitude does not vary by this factorization.

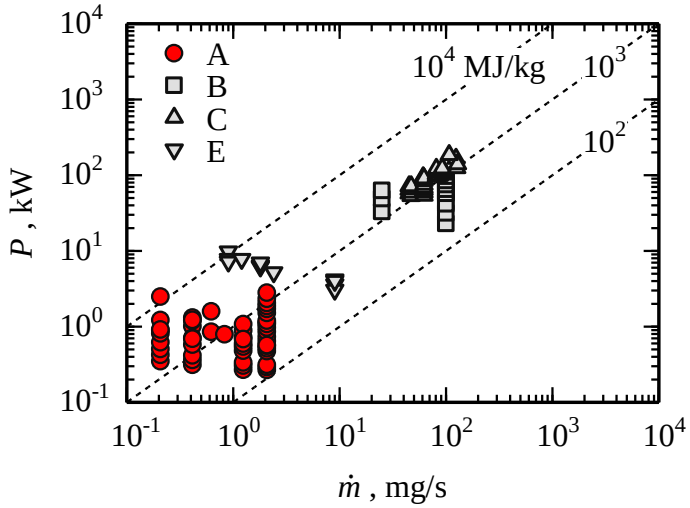

FIG. 3.3 Input power and propellant flow rate. A to E correspond to the same symbol as those used in Table 3.2. The uncertainties of $\dot{m}$ and P were no more than ± 7.4% and ± 0.2% of the measured value, respectively.

Figure 3.3 shows a plot of P vs. $\dot{m}$. In the figure, the letters A to E represent results from this study and previous studies, as indicated in Table 3.2. The figure does not include the data set of study C (Table 3.2), since the value of V_{d} is not indicated in the article. In this study (A), the values of both $\dot{m}$ and P were one to two orders of magnitude lower than those in the previous studies (B, C, E), but the specific power $P/\dot{m}$, in the range 10^2 – 10^4 MJ/kg, is at almost the same level. As mentioned in section 3.1, 10^2 – 10^4 A of J_{d} was necessary to obtain the thermionic electrons for keeping arc discharge using a conventional rod cathode. On the other hand, in this experiment, a thermionic-emission-type hollow cathode was used. Therefore, stable operation even with a small

propellant flow rate (approximately 0.2 mg/s) and a small current (~2 A) was achieved. As a result, operating with a small propellant flow rate and small input power can yield the same specific power level as in the previous studies.

Table 3.2 Operating ranges.

Data set	A	B	C	D	E
Reference	-	Myers et al.[118]	Tikhonov et al.[119]	Tahara et al.[120]	Sasoh et al.[121]
J_d, kA	0.01 – 0.02	0.75 – 1	6.5 – 16.5	1.2 – 2.9	0.085 – 0.2
$\overline{B}$, mT	133 – 265	30 – 165	38 – 190	45 – 90	25 – 250
$\dot{m}$, mg/s	0.83 – 3.9	25 – 100	400	45 – 126	0.9 – 9
P, kW	0.76 – 3.26	23 – 96	53 – 186	-	3 – 9.8
$P/\dot{m}$, $\times 10^9$ m^2/s^2	0.23 – 3.91	0.2 – 2.5	0.9 – 1.7	-	0.3 – 11
α, -	210 – 840	0.7 – 3.5	1 – 4.7	0.13 – 0.28	2.2 – 51

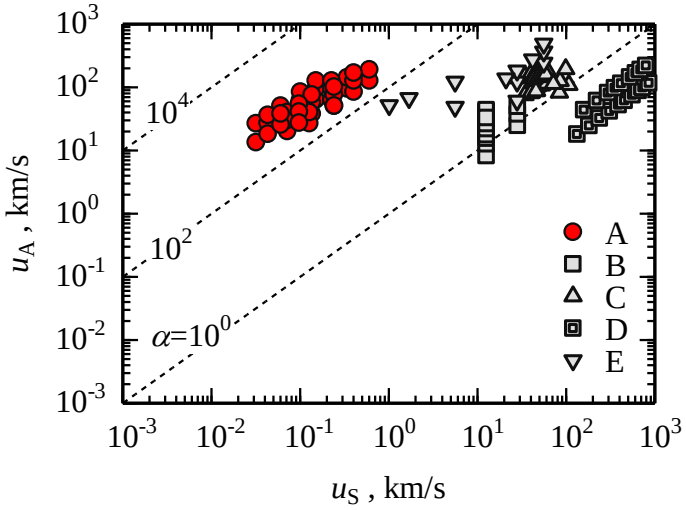

FIG. 3.4 Characteristic exhaust velocity ranges. A to E correspond to the same symbol as those used in Table 3.2.

Figure 3.4 shows the characteristic velocity based on the applied-field thrust, u_A, vs. that of the self-field thrust, u_S, given by:

$$u_A \equiv \frac{F_A}{\dot{m}}. \tag{3.4}$$

$$u_{\mathrm{s}} \equiv \frac{F_{\mathrm{s}}}{\dot{m}}. \tag{3.5}$$

The dashed lines correspond to constant values of α. As summarized in Table 3.2, α obtained in this study (A) was in the order of 10^2, while that of previous studies (B – E) was in the order of 10^{-1} to 10^1. As can be seen from Eq. (3.1), applying a strong magnetic field (~265 mT) increases the applied-field thrust even when a hollow cathode supplies a small discharge current (~20 A). In this way, Af-MPD thruster operation was achieved at very high values of α, which were higher than those reported in any previous study. In other words, operation was achieved in an applied-field-dominant condition.

3.3.2. High impedance discharge characteristics

Neglecting the Hall effect and ion slip, the generalized Ohm's law is given by

$$\mathbf{j} = \sigma(\mathbf{E} + \mathbf{u} \times \mathbf{B}). \tag{3.6}$$

In the rigid rotator model, each component in Eq. (3.6) can be expressed as follows in the cylindrical coordinate system.

$$\mathbf{j} = \begin{bmatrix} j_{\mathrm{r}} \\ 0 \\ 0 \end{bmatrix}, \ \mathbf{E} = \begin{bmatrix} E_{\mathrm{r}} \\ 0 \\ 0 \end{bmatrix}, \ \mathbf{B} = \begin{bmatrix} 0 \\ 0 \\ B_{\mathrm{z}} \end{bmatrix}, \ \mathbf{u} = \begin{bmatrix} 0 \\ u_{\theta} \\ 0 \end{bmatrix}. \tag{3.7}$$

Using Eqs. (3.6) and (3.7), the discharge voltage is expressed as

$$V_{\mathrm{d}} = V_0' - \int_{R_{\mathrm{C}}}^{R_{\mathrm{a}}} E_{\mathrm{r}} \mathrm{d}r \cong V_0' + \int_{R_{\mathrm{C}}}^{R_{\mathrm{a}}} \left(u_{\theta} B_{\mathrm{z}} - \frac{j_{\mathrm{r}}}{\sigma} \right) \mathrm{d}r \equiv V_0 + c_{\mathrm{v}} \frac{u_{\mathrm{A}}}{2} \bar{B} R_{\mathrm{a}}. \tag{3.8}$$

Here, V_0' is the sum of the anode sheath and cathode sheath drop. V_0 represents offset voltage; the sum of the potential drop due to V_0' and plasma's electrical residence drop. u_{A} and $u_{\mathrm{A}} \bar{B} R_{\mathrm{a}} / 2$ are the characteristics exhaust velocity of applied-field force and the representative value of the back electromotive force,[122] respectively. In the rigid rotator model, c_{v} is expressed as

$$c_{\mathrm{v,RR}} \equiv \left[1 - 3 \left(\frac{R_{\mathrm{c}}}{R_{\mathrm{a}}} \right)^2 \right]. \tag{3.9}$$

Substituting the keeper orifice radius for R_{c} (= 1 mm), $c_{\mathrm{v,RR}} \approx 1.0$.

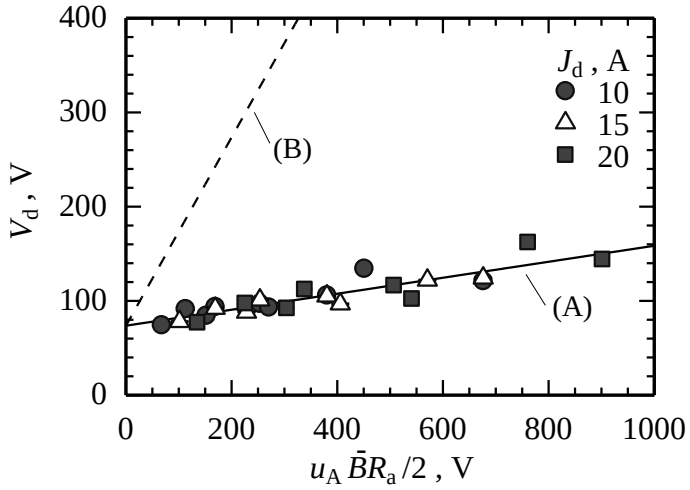

(a) z_c = -105 mm, $c_{v,EXP}$ = 0.084, V_0 = 74 V.

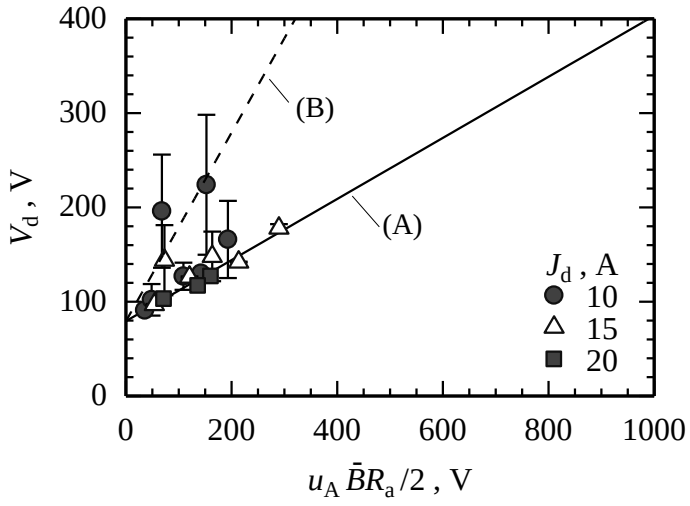

(b) z_c = 0 mm, $c_{v,EXP}$ = 0.32, V_0 = 79 V.

FIG. 3.5 V_d vs. $u_A \bar{B} R_a / 2$ of axisymmetric type Af-MPD thruster. (A): experimentally fit to Eq. (3.8), (B): rigid rotator model from Eqs. (3.8) and (3.9).

Figures 3.5 (a) and (b) show graphs of V_d vs. $u_A \bar{B} R_a / 2$ in $\dot{m}_1$ = 0.83 – 0.21 mg/s, $\dot{m}_2$ = 0 – 3.1 mg/s, J_d = 10 – 20 A, $\bar{B}$ = 133 – 265 mT, R_a = 40 mm. The uncertainty of V_d was no more than ± 2.7% of the measured value. As can be seen from the figure, V_d increases almost linearly with $u_A \bar{B} R_a / 2$. The rigid rotator model neglects the effect of viscosity; therefore, owing to viscosity, the effective value of c_v is smaller than that of $c_{v,RR}$. In this experiment, the effective value of c_v was estimated by curve fitting based on Eq. (3.8) and is represented as $c_{v,EXP}$. The fitted line is shown as the solid line (A), and the dashed line (B) shows the case for $c_v = c_{v,RR}$. Only stable

operating conditions, with RMS values (shown by the magnitude of the error bar) lower than 10% of the time-averaged value during thruster operation (shown by the symbol), were employed to the fit, thereby yielding $c_{v,EXP}$ = 0.084, V_0 = 74 V at z_c = -105 mm; and $c_{v,EXP}$ = 0.32, V_0 = 79 V at z_c = 0 mm. As increasing $u_A\overline{B}R_a/2$, the ratio of V_0 to V_d decreases, becoming 45% for both z_c = −105 mm and z_c = 0 mm. Therefore, for increasing $u_A\overline{B}R_a/2$, the contribution of the electromagnetic thrust generation in the power consumption increases.

In Ref. 123, with $\dot{m}$ = 100 mg/s (argon), α ~ 1 (J_d = 1 kA, $\overline{B}$ ~ 40 mT, R_a = 51 mm, z_c = 0 mm), the azimuthal Lorentz force causes the plasma to rotate and induces a shear force. This shear force and Joule heating due to kA-order discharge current causes the ion temperature to increase by up to 5 eV and transfer the internal energy to kinetic energy through the expansion along the magnetic nozzle. In this case, the azimuthal torque increases as $J_d\overline{B}R_a$ increases, but the shear force also increases. Therefore, the azimuthal velocity should saturate so that $u_A\overline{B}R_a/2$ and V_d are proportional to $\overline{B}$. On the other hand, under the conditions of this experiment, in which $\dot{m}$ ~ 3.9 mg/s and α ~ 100 (J_d ~ 20 A, $\overline{B}$ ~ 265 mT, R_a = 40 mm), From Fig. 3.5, V_d is proportional to $u_A\overline{B}R_a/2$ and from Eqs. (3.1) and (3.4), u_A is proportional to $\overline{B}$.As a result, V_d is a linearly increasing function of $\overline{B}^2$. Assuming that limiting the discharge current to 20 A suppresses heavy particle heating by decreasing the Joule heating, u_θ and $u_A\overline{B}R_a/2$ increase as $J_d\overline{B}R_a$ increases. In the rigid rotor model, the plasma is assumed to act as a rigid rotator by an azimuthal Lorentz force, $J_d\overline{B}R_a$, and expands through a diverging magnetic field. Owing to this expansion, the rotational energy is converted to the axial kinetic energy. In order to rotate ions inside the discharge channel, ions need to be magnetized; ion's Larmor radius must be smaller than R_a. In the case that the work done by the azimuthal Lorentz force is completely converted to rotational energy before the axial kinetic energy conversion, the ion's Larmor radius would become 37 mm with an ion rotational kinetic energy of 70 eV at $\overline{B}$ = 200 mT. This radius is closer to R_a and effect of finite ion-Larmor radius is not negligible. In reality, the plasma rotates in the azimuthal direction, and at the same time expands through the diverging magnetic field. Therefore, the

energy conversion from rotational energy to axial kinetic energy must occur simultaneously. Moreover, the viscous friction force accompanying the rotation is affected by the ions, and some portion of the rotational energy is converted to thermal energy. Therefore, the estimated value of $c_{v,EXP}$ is no more than 32% of $c_{v,RR}$. As with the rotational-kinetic energy conversion, the energy conversion from thermal energy to axial kinetic energy must occur simultaneously. As a result, the "effective" Larmor radius should be much smaller than the above overestimation. In the same manner, V_d is expressed in terms of the quantity $u_A \bar{B} R_a / 2$, and this results in the characteristic current-voltage behavior observed in F_A-dominant, high-α operation.

3.3.3. Thruster performances and loss mechanisms

The specific impulse, I_{sp}, and the thrust efficiency, η, are defined as

$$I_{sp} = \frac{F_{EXP}}{\dot{m} g}. \tag{3.10}$$

$$\eta = \frac{F_{EXP}^2}{2\dot{m}P} = \frac{F_{EXP}^2}{2\dot{m}\left(J_d V_d + J_k V_k\right)}. \tag{3.11}$$

Figure 3.6 shows the estimated values of I_{sp} and η of this study compared with those of previous studies, using argon as the propellant. Here, the effective propellant flow rate due to electrode erosion was not taken into account.

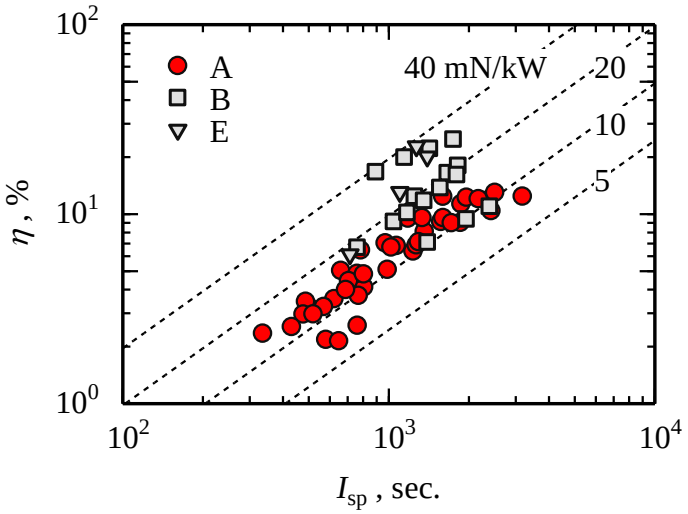

FIG. 3.6 Thruster performances, propellant species Ar. A to E correspond to the same symbol as those used in Table 3.2. The uncertainties of I_{sp} and η were no more than ± 10%, ± 29% of the measured value, respectively.

In this experiment (A), I_{sp} was 330 – 3200 s. In the data sets B and E, I_{sp} was 460–2400 s. From Eqs. (3.10) and (3.11), it can be seen that with constant η, the exhaust velocity is proportional to the square root of the specific power $P/\dot{m}$. Therefore, as shown in Fig. 3.6, I_{sp} is at the same level as in previous studies since $P/\dot{m}$ is at the same level. However, the thrust-to-power ratio is lower by a factor of two.

The thrust efficiency η was at most 13%. This values are about half of those obtained in previous studies. In an Af-MPD thruster, anode power consumption P_a has long been recognized as a major loss mechanisms: most of the input power is wasted in heating anode. Gallimore et al.[124] reported a breakdown of input power J_dV_d using argon as propellant under 31 mT of $\overline{B}$ and 850 A of J_d. In this case, anode power consumption fraction P_a/J_dV_d was 75% of total input power. Within this magnetic field range, the heat flux to the anode increased monotonically with $\overline{B}$. Myers et al.[111] also evaluated the power fraction of anode power deposition with several operating conditions and thruster geometries. They reported that P_a/J_dV_d was 50 – 85% through 22 – 225 mT of $\overline{B}$, 750 and 1000 A of J_d, 25 – 100 mg/s of argon, and 25.4 – 51 mm of R_a. P_a/J_dV_d was increased as decreasing propellant mass flux $\dot{m}/(\pi R_a^2)$. In Myers's report, $\dot{m}/(\pi R_a^2)$ was 1.2×10^2 – 3.0×10^2 kg/m^2/s. On the other hand, in this experiments, $\dot{m}/(\pi R_a^2)$ ranged 1.6 – 7.7 kg/m^2/s. In $\dot{m}_1$ = 1.25 mg/s, $\dot{m}_2$ = 0 mg/s, J_d = 20 A, $\overline{B}$ = 265 mT, and V_d = 144 V operation, η had maximum value of 13%. Using P_a/J_dV_d = 0.5 as in Ref. 111, P_a = 1442 W. Assuming P_a comes from the energy consumption at anode fall, anode sheath drop voltage is estimated as P_a/J_d = 72 V. This value agree well with V_0 in Fig. 3.5. From Eq. (3.8), schematic potential profile can be estimated as shown in Fig. 3.7. Owning to utilize the hollow cathode, the cathode sheath drop is expected to be small. Because supplied propellant mass flow rate was 1/10 – 1/100 times smaller than that of previous studies (see Fig. 3.3), space potential near the anode must be much lower than anode potential to collect electrons for sustaining constant current discharge. Thereby, the predominantly component of V_0 is expected to be anode sheath voltage, and the input power was predominantly consumed in anode fall.

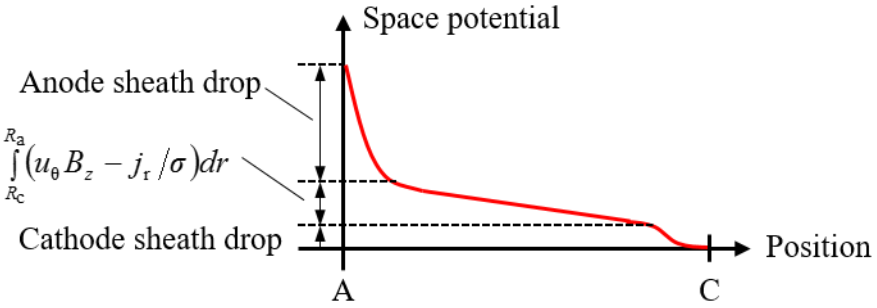

FIG. 3.7 Schematic of potential profile in Af-MPD thruster.

Another source of limiting thrust efficiency is collisional process. As shown in Fig. 3.6, calculated I_{sp} reached up to 3200 s. Assuming that ion velocity u_i is uniform on the thruster exit plane, ion kinetic energy $\langle\varepsilon_i\rangle$ is calculated as in Eq. (3.12).

$$\langle\varepsilon_i\rangle = \frac{1}{2e}m_i u_i^2 = \frac{1}{2e}m_i\left(gI_{sp}\right)^2. \tag{3.12}$$

From Eq. (3.12), $\langle\varepsilon_i\rangle \approx 200$ eV. This is larger than V_d (= 144 V). In practice, ion's velocity is higher than gI_{sp} because gI_{sp} is averaged plume exhaust velocity and Lorentz force accelerate only charged particles. Nerheim et al.[125] called this phenomena as anomalous velocity and explained from the view point of momentum transfer by Coulomb collisions between ions and electrons. However, this anomalous ion acceleration causes large velocity difference between ions and neutrals. The dominant mechanisms for momentum transfer from ions to neutrals is charge exchange collision. Assuming that 1.0 eV of electron temperature, 50% of propellant utilization ($\equiv J_i/(e\dot{m}/m_i)$),[50] and the neutrals flow in acoustic velocity, neutral velocity and number density is 1500 m/s and 2.0×10^{18} m^{-3}, respectively. At 200 eV of ion kinetic energy, charge exchange collision cross section[126] is 2×10^{-19} m^2 and mean-free-path of charge exchange collision is calculated as 1.0 m. This is much larger than thruster characteristics length. Therefore, ions and neutrals have insufficient momentum transfer collisions in downstream region. This condition is referred to as ion slip and causes deteriorate the thrust efficiency because of uncoupling of the electromagnetic process from the gasdynamic.[44]

3.4. Summary of Chapter 3

In this chapter, the operating characteristics of Af-MPD thruster , with a ratio of applied- to self-field thrusts α in the range of 10^2 – 10^3, was investigated. Discharge voltage was expressed using back electromotive force $u_A \overline{B} R_a / 2$. Using a hollow cathode, applied-field dominant operation was achieved under the same specific power level (10^2 – 10^4 MJ/kg) but with 10 to 100 times smaller mass flow rates than reported in previous studies. This was mainly achieved by the employment of a hollow cathode to maintain stable arc discharge at discharge current levels of up to 20 A. Even with a 10 A level of discharge current, the thrust efficiency achieved 13% as maximum. However, the input power can be mainly consumed by anode sheath drop and from the thrust measurement, ion anomalous acceleration can make the thruster operation inefficiently.

4.

Contribution of radio-frequency power on electrostatic ion acceleration

4.1. Pre-ionization propellant injection

Foster et al.[127] reported that the anode sheath drop voltage is in inverse proportion to near-anode ionization rate. They also made three proposals for increasing plasma density near the anode;[128] injection of pre-ionized propellant, consumable anode insert, and increasing discharge chamber pressure. In order to make the pre-ionized propellant, helicon plasma sources are useful because they produce high-density plasma on the order of 10^{19} m^{-3} using a relatively simple arrangement. In electrostatic acceleration process, the propellant utilization is close to unity, and only ions are accelerated using a static electric field without collisional dissipation process. This acceleration process is suitable for preventing ion slip losses as mentioned in section 3.3.3. Harada et al.[80] demonstrated electrostatic acceleration of helicon plasma using a cusped magnetic field and electrode placed at the exit of the helicon plasma source (Helicon Electrostatic Thruster, HEST). Nevertheless, a few open questions remain, i.e., the extent of the helicon plasma source contribution for enhancing the thrust efficiency, and whether there exists an optimal RF power to acceleration power ratio. In this chapter, the electrostatic acceleration method in diverging magnetic field is investigated by using HEST. The aim of this chapter is quantitatively investigating the power matching between RF plasma generation and electrostatic acceleration in HEST.

4.2. Helicon electrostatic thruster (HEST)

Figure 4.1 shows a schematic of HEST. HEST has an RF plasma source in the upstream region and electrostatic acceleration electrode in the downstream region. The RF plasma source was comprised of a ceramic (Photoveel) tube with an inner diameter of 27 mm and length of 150 mm. A Nagoya type III (m = +1) helical antenna was coaxially fixed the ceramic tube. The exit of the RF plasma source was located at the center of the solenoid coil. The magnetic field strength was 100 mT at the coil center. A copper ring anode had an inner diameter of 27 mm and thickness of 10 mm. The left-side-surface of the ring anode was located at 25 mm axially downstream from the coil center. In the downstream region, the magnetic field was greatly modified using 16 cylindrical Nd–Fe–B permanent magnets and soft iron yokes to generate a diverging magnetic field followed by a field-free region where the magnetic field strength was less than 3 mT. A commercial hollow cathode (DLHC-1000, Kaufman & Robinson Inc.) was used and its orifice was placed 70 mm off-axis at 175 mm axially downstream from the coil center.

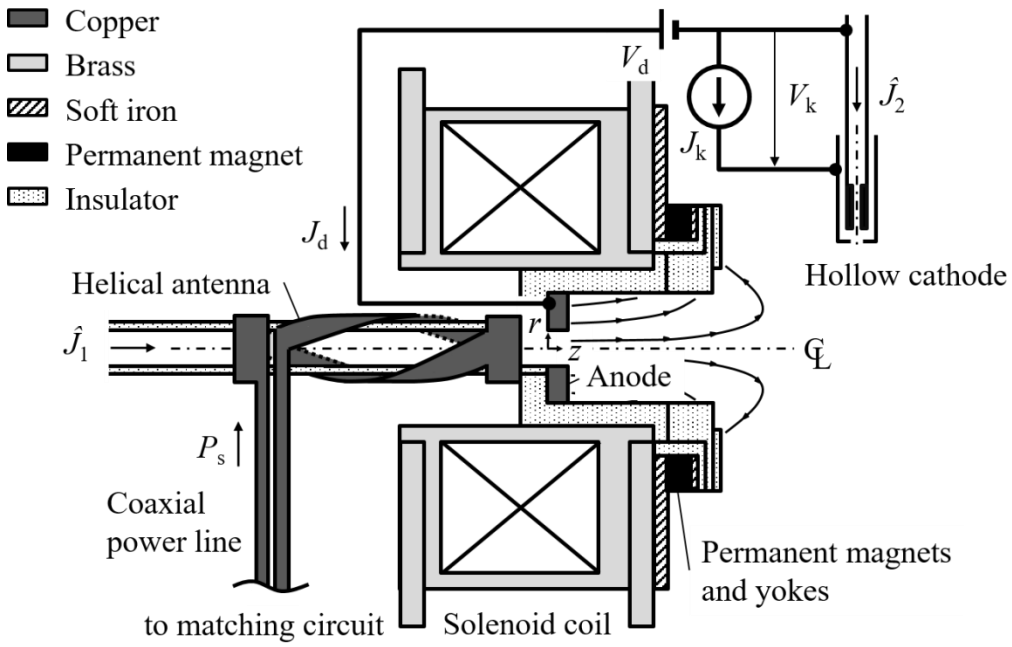

FIG. 4.1 Schematic of HEST.

4.3. Plasma source effects on ionization and acceleration performances

4.3.1. Operating conditions

All experiments were conducted in Chamber-B. The working gas flow rate supplied to the plasma source $\hat{J}_1$ was set to 0.5 or 1.0 Aeq, and the RF power to the plasma source P_s was increased every 20 W from 0 to 300 W and every 100 W from 300 to 1500 W. The discharge voltage V_d was set to 300 V in the $E_i(0)$, J_i, and discharge current J_d measurements. In the probe measurements, V_d was set to 200 V. The hollow cathode was operated with a working gas flow rate, $\hat{J}_2$, of 0.36 Aeq, and the keeper current J_k was set to 2.0 A. $E_i(0)$, J_i, $\langle\theta\rangle$, J_d, and keeper voltage V_k were measured at least twice in same operation condition. In the following figures, the circles represent the average value. The error bars in $E_i(0)$, J_i, J_d, and $\langle\theta\rangle$ correspond to the standard deviation ($\pm\sigma$) obtained from the number of trials. The operation time was at least 3.5 s at each operating condition.

4.3.2. Ion current and energy characteristics in $\hat{J}_1$= 0.5 Aeq operation

Figure 4.2(a) shows the variation of J_i with P_s for the $\hat{J}_1$ = 0.5 Aeq and V_d = 300 V operation. J_i increased with P_s. In particular, J_i increased from 0.07 to 0.36 A as P_s increased from 0 to 40 W. When P_s > 40 W, J_i increased more gradually. At P_s = 1500 W, J_i was equal to 0.80 A, which is 93% of the total supplied flow rate $\hat{J}_1 + \hat{J}_2$. Figure 4.2(b) shows the variation of $E_i(0)$ with P_s with $\hat{J}_1$ = 0.5 Aeq and V_d = 300 V operation. $E_i(0)$ decreased from 133 to 107 eV as P_s increased from 0 to 40 W. Conversely, while P_s increased from 40 to 80 W, $E_i(0)$ increased rapidly from 107 to 188 eV. At P_s = 1500 W, $E_i(0)$ reached 265 eV, which is 88% of V_d. In Ref. 129, by combing the annular helicon plasma source with a Hall thruster, the ion beam current increased up to 50% of $\hat{J}_1 + \hat{J}_2$ with the increase in helicon plasma source input power. However, the ion beam energy decreased to 80% of V_d. In this experiment, J_i and $E_i(0)$ increased by a factor of 11 and 2, respectively, as P_s increased from 0 to 1500 W. Therefore, in the $\hat{J}_1$ = 0.5 Aeq operation case, the RF plasma source contributed to both the ion generation and electrostatic acceleration.

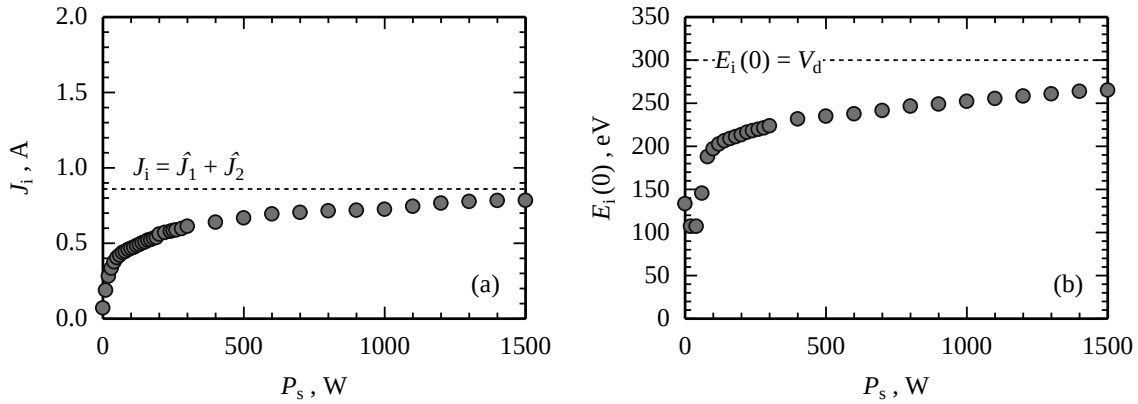

FIG. 4.2 P_s dependence with $\hat{J}_1$ = 0.5 Aeq, $\hat{J}_2$ = 0.36 Aeq, and V_d = 300 V. (a) P_s vs. J_i, (b) P_s vs. $E_i(0)$.

Figure 4.3 shows the distribution of n_e, T_e, and V_s on the center axis for the P_s = 0 and 300 W and V_d = 200 V operation. Due to a low signal-to-noise ratio, the n_e and T_e values at z > 150 mm were not obtained except the center axis. In the P_s = 0 W operation, n_e was equal to 2.0×10^{17} m^{-3} at z = 0 mm and decreased toward the downstream region. However, it had a local minimum of 6.3×10^{16} m^{-3} at z = 85 mm and a local maximum of 1.5×10^{17} m^{-3} at z = 125 mm. Meanwhile, in the P_s = 300 W operation, at z = 0 mm, $n_e = 3.0\times10^{18}$ m^{-3}. This is more than 10 times higher than that of the operation at P_s = 0 W. n_e then decreased monotonically toward the downstream direction. Shoji et al.[130] measured the variations in electron number density with the change in RF power. By using Nagoya type III antenna (m = + 1), a steep density increase was observed at approximately 400 W of RF power in the argon gas operation. They also reported that the required RF power to produce a steep density increase was smaller when the RF power frequency was close to the lower hybrid frequency ω_{LH}, which can be calculated as in Eq. (4.1).

$$\omega_{LH} \equiv \sqrt{\omega_{ci} \cdot \omega_{ce}}\,. \tag{4.1}$$

Here, ω_{ci} and ω_{ce} are the ion cyclotron frequency and electron cyclotron frequency, respectively. For a singly charged argon ion, ω_{LH} = 10.3 MHz at B = 100 mT. This is close to the RF power frequency (13.56 MHz). Therefore, the HEST also exhibited a density jump in the same RF power

range to that reported in Ref. 130; as a result, J_i increased from 0.07 A at P_s = 0 W to 0.61 A at P_s = 300 W (see Fig. 4.2(a)).

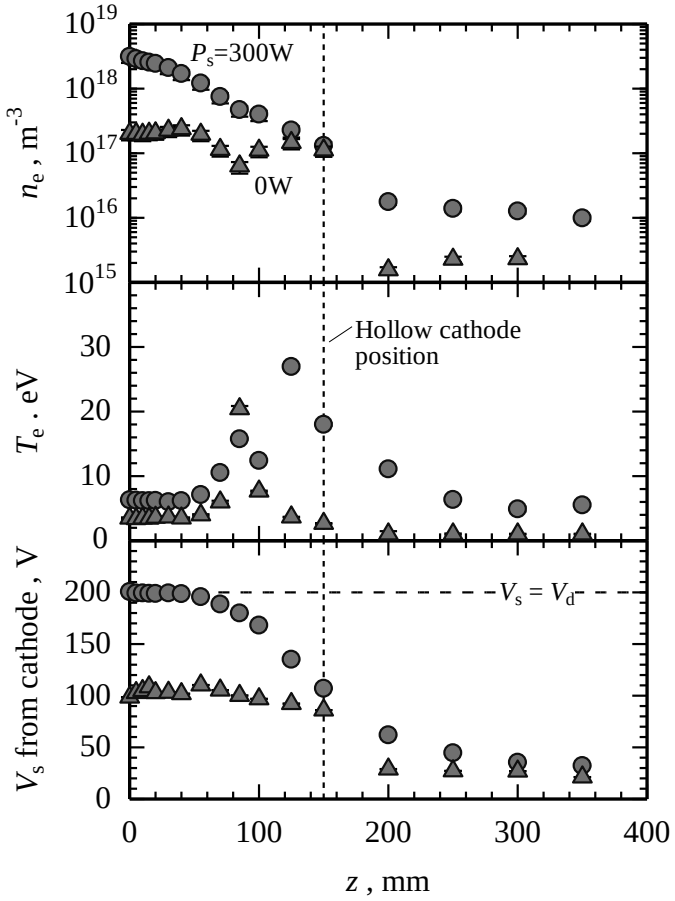

FIG. 4.3 n_e, T_e, and V_s distribution on axis. $\hat{J}_1$ = 0.5 Aeq, $\hat{J}_2$ = 0.36 Aeq, V_d = 200 V.

In the P_s = 0 W operation, V_s at z = 0 mm was 99 V and started to decrease from z = 85 mm, which is the same location to where T_e had the peak value of 20 eV. At z = 350 mm, V_s was 26 V. The electron temperature distribution relates to the space potential distribution.[131] Figure 4.4 shows the relation between potential distribution and electron energy. Electrons comes from low potential region (right side) and neutrals comes from high potential region (right side). Through the potential drop, the thermionic electrons diffused from the hollow cathode gained kinetic energy and then lost it by ionization collision with the injected working gas.

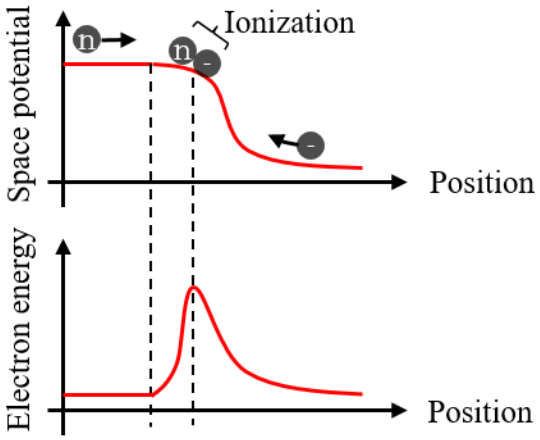

FIG. 4.4 Schematic of the relation between space potential and electron energy.

In the P_s = 300 W operation, T_e exhibited a double-peak distribution; small peak of 16 eV at z = 125 mm and large peak of 27 eV at z = 125 mm. One possible reason for this double-peak T_e distribution is that electron impact ionization occurred two times; the first one was at z = 125 mm and the second one was at z = 85 mm. At z = 125 mm, V_s = 135 V. The electrons can be accelerate again toward the anode potential and obtain the kinetic energy. Then, at z = 85 mm, the electrons collide with neutrals once again and lost their energy. V_s at z = 0 mm was 198 V, which is almost identical to the discharge voltage (200 V). At z = 85 mm, V_s started to monotonically decrease toward the downstream direction and reached 38 V at z = 350 mm. The measured V_s values at z = 0 and 350 mm were consistent with the IEDF, i.e., in the P_s = 300 W operation, the ion beam potential and space potential were 184 and 41 V, respectively. By injecting the pre-ionized working gas, the generated ions were electrostatically accelerated from near the anode potential and obtained an average energy of $E_i(0)$, as shown in Fig. 4.2(b).

Figure 4.5 shows the color contours of n_e, T_e, and V_s for the P_s = 300 W and V_d = 200 V operation. The n_e distribution is affected by the diverging magnetic field. As shown in Fig. 4.5(a), n_e was confined within $r \leq 20$ mm. From z = 70 mm, the end of the diverging magnetic field, the low electron number density region spread within $r \leq 20$ mm. As shown in Fig. 4.5(b), in the $r \geq 20$ mm region, T_e maintained a constant value along the magnetic lines of force because electrons

have a considerably larger mobility in the direction parallel to the magnetic lines of force than that in the perpendicular direction.[132] Conversely, in the $r \leq 20$ mm region, T_e varied along the magnetic lines of force. From Fig. 4.5(c), V_s decreases toward the downstream direction and the axial electric field was generated. Oudini et al.[133] reported that if the electron temperature and/or plasma density gradients are large, the magnetic lines of force will no longer be equipotential. As shown in Figs. 4.5(a) and (b), n_e and T_e varied along the magnetic lines of force, particularly, within $z \leq 20$ mm and $r \leq 20$ mm. Therefore, the space potential also varied along the magnetic lines of force and decreased in the axial direction.

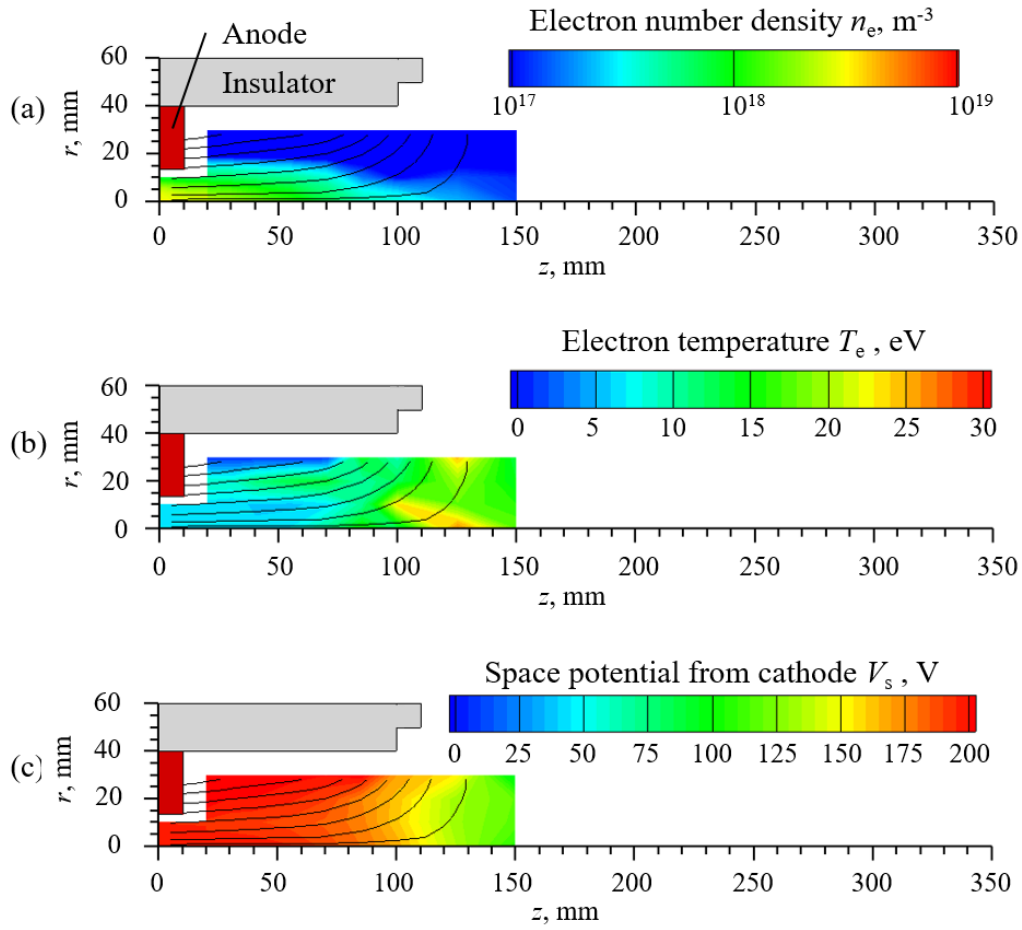

FIG. 4.5 Distribution of (a) n_e, (b) T_e, and (c) V_s. $\hat{J}_1$ = 0.5 Aeq, $\hat{J}_2$ = 0.36 Aeq, V_d = 200 V, P_s = 300 W.

4.3.3. Ion current and energy characteristics in $\hat{J}_1$= 1.0 Aeq operation

Figure 4.6(a) shows the variations of J_i with P_s in the $\hat{J}_1$ = 1.0 Aeq and V_d = 300 V operation. In the P_s = 0 W operation, J_i was equal to 1.0 A, which is 77% of $\hat{J}_1 + \hat{J}_2$. In general, J_i increased with P_s. However, J_i had a local minimum at P_s = 40 W. When P_s > 40 W, J_i increased with P_s. At P_s = 400 W, J_i was equal to the value of $\hat{J}_1 + \hat{J}_2$, and, at P_s = 1500 W, J_i was 1.2 times larger than $\hat{J}_1 + \hat{J}_2$. According to the current fraction of each charge-state ion measured by the **E×B** probe, the doubly charged argon ion current had 22% of J_i at P_s = 500 W and increased to 27% at P_s = 700 W.

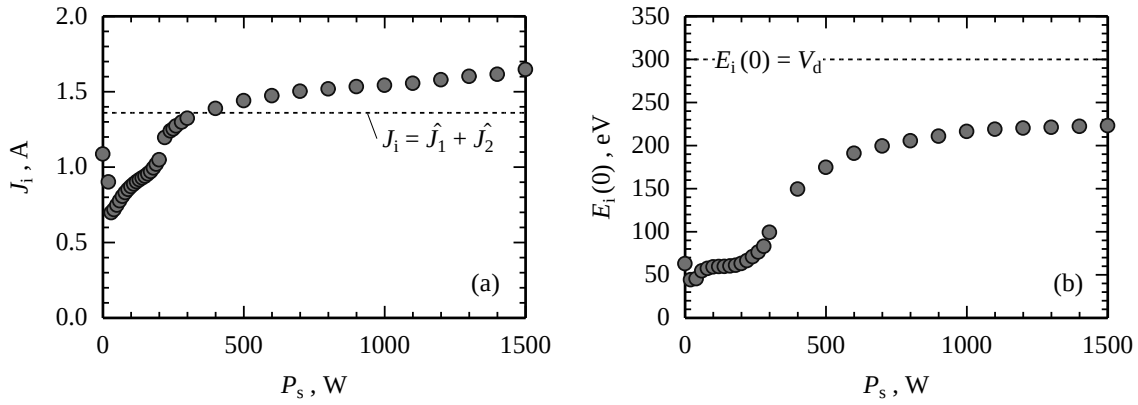

FIG. 4.6 P_s dependence with $\hat{J}_1$ = 1.0 Aeq, $\hat{J}_2$ = 0.36 Aeq, and V_d = 300 V. (a) P_s vs. J_i, (b) P_s vs. $E_i(0)$.

Figure 4.6(b) shows the variations of $E_i(0)$ with P_s for the $\hat{J}_1$ = 1.0 Aeq and V_d = 300 V operation. When $P_s \leq$ 200 W, $E_i(0)$ maintained approximately 60 eV and then increased from P_s = 200 W. However, $E_i(0)$ was gradually saturated at approximately 220 eV, which is 73% of V_d. From the **E×B** probe measurement in the P_s = 600 W operation (see Fig. 2.14), the effective acceleration voltage of a singly charged and doubly charged argon ion were 186 V and 143 V, respectively. Figure 4.7 shows schematic of the relation between an ionization position and an effective acceleration voltage for Ar^+ and Ar^{2+}. The effective acceleration voltage is space potential difference from where the ions were generated to downstream. Kim et al.[134] measured

the effective acceleration voltage on the axis of a Hall thruster. The effective acceleration voltage of a doubly charged ion was 10 – 30 V lower than that of a singly charged ion. From simulations by Katz et al.[135], the doubly charged ions were generated at a lower space potential region than that of the singly charged ions. Youbong et al.[94] measured the effective acceleration voltage of each charge-state ion in a cylindrical Hall thruster and reported an up to 30 V lower acceleration voltage of doubly and triply charged ions than that of singly charged ions. In our experiments, the doubly charged ions had a 43 V lower effective acceleration voltage than that of the singly charged ions. As shown in Fig. 4.3 the space potential of the HEST decreased monotonically from the upstream anode potential toward the downstream direction. Therefore, as described in Ref. 135, doubly charged ions were generated in a low space potential region, and, as a result, the effective acceleration voltage was also lower than that of singly charged ions. These results indicate that, in this $\hat{J}_1$ = 1.0 Aeq operation, the contribution of P_s to the increase of $E_i(0)$ was limited because of the generation of low-energy doubly charged ions.

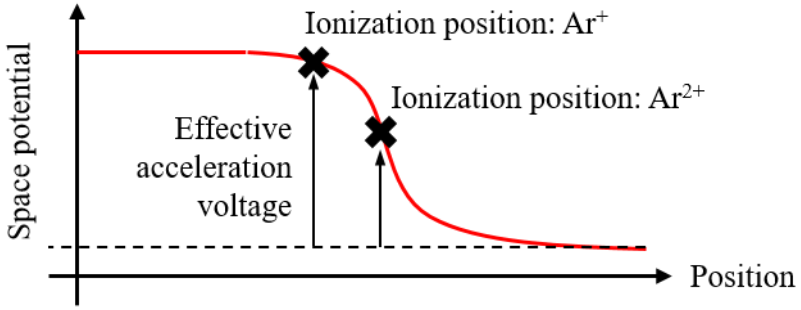

FIG. 4.7 Schematic of the relation between ionization position and effective acceleration voltage for single- and doubly-charged ions.

Figure 4.8 shows the color contours of n_e, T_e, and V_s for the $\hat{J}_1$ = 1.0 Aeq, P_s = 300 W, and V_d = 200 V operation. By increasing $\hat{J}_1$, the maximum value of n_e increased to 6.9×10^{18} m^{-3} at (r, z) = (0 mm, 0 mm). As shown in Fig. 4.8 (a), the electrons were confined by the diverging magnetic field as well as the $\hat{J}_1$ = 0.5 Aeq operation (see Fig. 4.5 (a)). However, in the $\hat{J}_1$ = 1.0 Aeq operation, the local peak of electron temperature vanished and the maximum electron temperature decreased

to 16 eV at (r, z) = (20 mm, 5 mm). As shown in Fig. 4.8 (c), in the $r \geq 5$ mm region, V_s maintained a constant value along the magnetic lines of force. In the $r \leq 5$ mm region, V_s varied along the magnetic lines of force because of the large n_e and T_e gradient;[133] this also occurs in the $\hat{J}_1 = 0.5$ Aeq operation (see Fig. 4.5 (c)). In general, V_s decreased from the upstream to downstream regions, and an axial electric field was generated. At (r, z) = (0 mm, 0 mm) and (0 mm, 350 mm), V_s was equal to 159 and 35 V, respectively. In the $\hat{J}_1 = 0.5$ Aeq operation, ions were accelerated from the anode potential (see Fig. 4.3). However, by increasing $\hat{J}_1$, the working potential difference decreased and, as a result, the acceleration performance deteriorated, as shown in Fig. 4.6 (b).

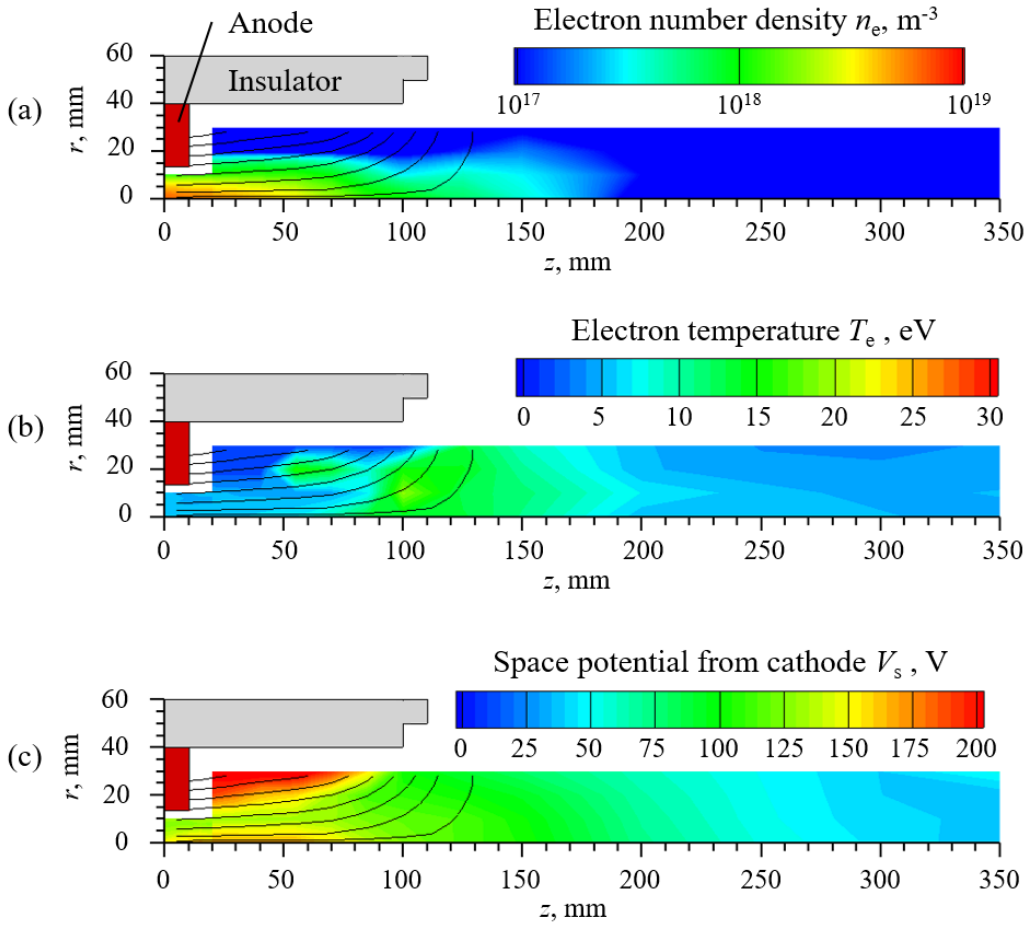

FIG. 4.8 Distribution of (a) n_e, (b) T_e, and (c) V_s. $\hat{J}_1 = 1.0$ Aeq, $\hat{J}_2 = 0.36$ Aeq, $V_d = 200$ V, $P_s = 300$ W.

4.4. Thruster performances

4.4.1. Discharge current characteristics

Figure 4.9 shows the dependence of J_i on J_d and $\hat{J}_1$ for the P_s = 0 – 1500 W and V_d = 300 V operation. Being independent of $\hat{J}_1$ and P_s, J_i was almost a linear function of J_d. J_i/J_d was adequately fit to a gradient of 0.4 – 0.6, which indicates that the discharge current was composed of 40 – 60% of the ion beam current from the plasma source, and the rest was the electron backflow from the hollow cathode.

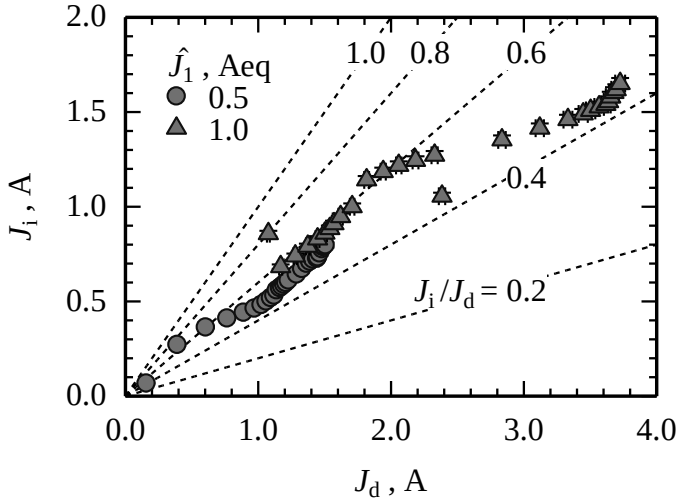

FIG. 4.9 J_d vs. J_i. $\hat{J}_2$ = 0.36 Aeq, V_d = 300 V, P_s = 0 – 1500 W.

4.4.2. Input power matching between plasma source and electrostatic acceleration

In this section, the thruster performance such as thrust F, specific impulse I_{sp}, and thrust efficiency η are estimated. From the energy conservation law, the average Z-charged ion velocity $u_{i,Z}$ can be calculated as

$$\frac{1}{2} m_i u_{i,Z}^2 = eZ\eta_{a,Z} V_d . \tag{4.2}$$

Here $\eta_{a,Z}V_d$ is effective acceleration voltage of Z-charged ions, respectively. By combining the law of the conservation of momentum, F can be calculated as

$$F \approx \sum_Z \left(m_i \frac{J_i}{Ze} \frac{J_{i,Z}}{J_i} u_{i,Z} \right) \cos\langle\theta\rangle. \tag{4.3}$$

Here, $J_{i,Z}/J_i$ is the current fraction of Z-charged ions. The $\eta_{a,Z}V_d$ and $J_{i,Z}/J_i$ values are obtained by the **E×B** probe measurement. In reality, the $J_{i,Z}/J_i$ value is a function of θ,[134] but, in this here, it is represented by a center axis value. The cos<θ> value is also assumed to have no dependence on Z. The definition of η can be expressed as follows;

$$\eta = \frac{F^2}{2 m_i \hat{J}/e \cdot \left(P_s + J_d V_d + J_k V_k \right)}. \tag{4.4}$$

Figure 4.10 shows the η dependence on $P_s/(J_d V_d)$, which is the RF power ratio against the electrostatic acceleration power. In the $\hat{J}_1$ = 0.5 Aeq case, $Z \leq 1$ is assumed, i.e., the exhaust plume consists of only singly charged ions. By varying $P_s/(J_d V_d)$, η achieved a peak value of 6.6% at $P_s/(J_d V_d) \approx 1.0$, which corresponds to P_s = 300 W. Yamagiwa et al.[136] analyzed the relation between the effective ion generation cost $c_{i,eff.}$ and η in a double-stage electrostatic thruster. Based on the energy conservation relation, $c_{i,eff.}$ is defined by

$$c_{i,eff} \equiv \frac{P_s + J_d V_d - E_i J_i}{J_i}. \tag{4.5}$$

Using $c_{i,eff.}$ and $P_s/(J_d V_d)$, η can be represented by

$$\begin{aligned} \eta &= \frac{J_i}{\hat{J}_1 + \hat{J}_2} \cdot \frac{J_i E_i}{P_s + J_d V_d} \cdot \left(\cos\langle\theta\rangle \right)^2 \\ &= \frac{J_i}{\hat{J}_1 + \hat{J}_2} \cdot \frac{1 + P_s/(J_d V_d) - c_{i,eff}/V_d \cdot J_i/J_d}{1 + P_s/(J_d V_d)} \cdot \left(\cos\langle\theta\rangle \right)^2. \end{aligned} \tag{4.6}$$

From Eq. (4.6), η is the product of the ion current ratio against the total supplied working gas flow rate, energy conversion efficiency, and ion beam divergence efficiency. <θ> had only a small dependence on both $\hat{J}_1$ and P_s, and was equal to 46 ± 2 deg, which corresponds to $(\cos\langle\theta\rangle)^2 \approx$ 0.48. In the $\hat{J}_1$ = 0.5 Aeq operation, as shown in Fig. 4.2 (a), J_i was saturated at $\hat{J}_1 + \hat{J}_2$ and, as shown in Fig. 4.9, J_i/J_d varied between 0.4 and 0.6. By substituting J_i, $E_i(0)$, and J_d in Eq. (4.5), $c_{i,eff.}$ can be calculated. When $P_s/(J_d V_d) < 1.0$, with the increase in P_s, $J_i/(\hat{J}_1+\hat{J}_2)$ increased rapidly

from 0.08 to 0.81 and $c_{i,eff.}$ varied between 390 and 840 W/A. Therefore, the increase in the first term of Eq. (4.6) i.e. $J_i/(\hat{J}_1+\hat{J}_2)$, mainly affected η. Conversely, when $P_s/(J_dV_d) > 1.0$, with the increase in P_s, $J_i/(\hat{J}_1+\hat{J}_2)$ slightly increased from 0.71 to 0.91 and $c_{i,eff.}$ increased from 870 to 2190 W/A. In this case, the decrease in the second term of Eq. (4.6) i.e. energy conversion efficiency, mainly affected η. Consequently, η had a peak value at the optimum input power ratio, which depends on both the ion generation and effective ion generation cost.

In the $\hat{J}_1 = 1.0$ Aeq case, assuming $Z \leq 1$, η exhibited the same dependence on $P_s/(J_dV_d)$ as in the $\hat{J}_1 = 0.5$ Aeq case; η increased rapidly with the increase in $P_s/(J_dV_d)$ from 0 to 0.6. In the $0.6 \leq P_s/(J_dV_d) \leq 0.9$ region, η maintained a constant value and started to decrease from $P_s/(J_dV_d) > 0.9$. In the $0.6 \leq P_s/(J_dV_d) \leq 0.9$ region, η had a maximum value of 8.7%. Considering doubly charged ions ($Z \leq 2$), with the increase in P_s from 500 to 700 W, $P_s/(J_dV_d)$ increased from 0.53 to 0.67 and η increased from 6 to 7%. Therefore, without taking into account the doubly charged ions, η can be overestimated to 17 – 20%. This overestimation comes from the thrust calculation in Eq. (4.3). In the $\hat{J}_1 = 1.0$ Aeq and $P_s = 700$ W operation, the calculated F in the $Z \leq 1$ and $Z \leq 2$ cases were 13 and 11 mN, respectively. As discussed in section 4.3.3, the doubly charged ions have a low effective acceleration voltage. The average momentum flux in the exhaust plume decreased and, as a consequence, the I_{sp} and η values decreased. From Fig. 4.10, η had maximum value with $P_s/(J_dV_d) \approx 0.6 – 1.0$ for $\hat{J}_1 = 0.5$ and 1.0 Aeq operation. This means that in order to maximize the thrust efficiency, required total input power is 1.6 – 2.0 times higher than that of without plasma source operation. In $\hat{J}_1 = 0.5$ operation, η had maximum value of 6.6% with total input power of 710 W. In this case, specific power was 2.0×10^3 MJ/kg. This is same order of the applied magnetic field thruster ($10^2 – 10^4$ MJ/kg) discussed in chapter 3. By inputting an optimal input power to the helicon plasma source, thrust efficiency reaches same level as high-impedance, Af-MPD thruster.

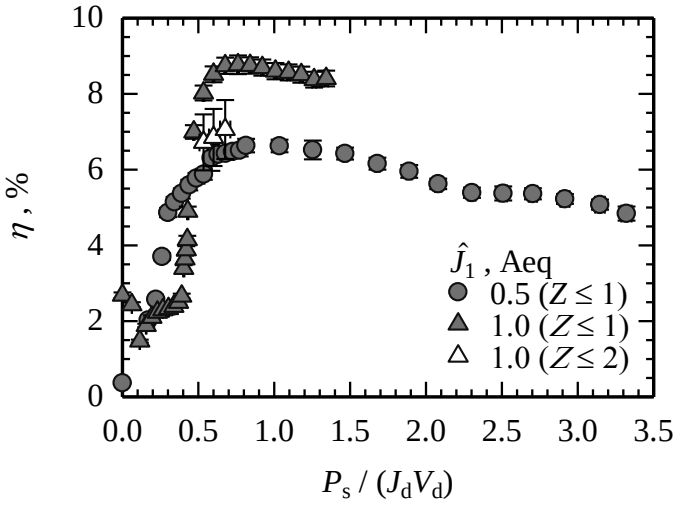

FIG. 4.10 Thrust efficiency η vs. input power ratio $P_s/(J_d V_d)$. $\hat{J}_2$ = 0.36 Aeq, V_d = 300 V.

4.5. Summary of Chapter 4.

In the operation of the HEST, the effects of RF power on the ion generation and electrostatic acceleration characteristics were evaluated. The RF power had different effects on thruster operation characteristics in different power range under constant discharge voltage of 300 V. For argon gas flow rate of 0.5 Aeq operation, in the RF power range of 0 to 80 W, the RF power increment was utilized for working gas ionization in the plasma source and then enhance the electrostatic acceleration through an axial electric field from the end of the diverging magnetic field. In this power range, ionization enhancement in the plasma source contributed to improve ion acceleration performance. However, in the RF power range of more than 80 W, the ion beam current and ion beam energy were both gradually saturated at 93% of total flow rate and 88% of discharge voltage equivalent, respectively. In this case, injected working gas was ionized with high effective ionization cost of up to 2190 W/A. Meanwhile, in the 1.0 Aeq operation, the ion beam current exceeded the total supplied working gas flow rate of 1.36 Aeq by inputting the RF power more than 400 W. The RF power increment was consumed for low energy, doubly charged ions generation. The thrust efficiency was governed by the RF power ratio against to electrostatic acceleration power. In both flow rate, the thrust efficiency reached maximum value at the RF power ratio against to electrostatic acceleration power of 0.6 – 1.0.

5.

Near-anode ionization and high impedance electrostatic ion acceleration in diverging magnetic field

5.1. Ionization near the anode potential region

Foster et al.[128] also proposed that increasing ionization rate near the anode decrease anode sheath drop voltage. As mentioned in section 4.1, Uchigashima et al.[137] investigated electron current path in HEST and concluded that electrons from the hollow cathode flow into the ring anode from anode inner surface. As shown in Fig. 4.6(a), by supplying 1.0 Aeq flow rate of argon, 77% of total supplied working gas was ionized by direct discharge. The extracted ion beam current was at the same level as that of inputting 200 W of RF power to the helicon plasma source. Based on afore-mentioned proposal and results, it is possible to remove helicon plasma source and thus, working gas injection near the anode inner surface is investigated to enhance ionization around the anode. In this chapter, this type of ion accelerator is termed as a "Diverging Magnetic field Electrostatic Thruster" (DM-EST).

5.2. Diverging magnetic field electrostatic thruster (DM-EST)

Figure 5.1 shows a schematic of the DM-EST. The main components, a solenoid coil, a ring anode, and a hollow cathode that are identical to those in the HEST.[80] As opposed to the helicon plasma source, an alumina-made insulating plate with a projection diameter of 24 mm was included at the ring anode entrance. The projection and the anode inner surface forms an annular slit with length and width corresponding to 2 mm and 1.5 mm, respectively. The supplied working gas was diffused azimuthally in advance, and it entered inside the ring anode through the slit.

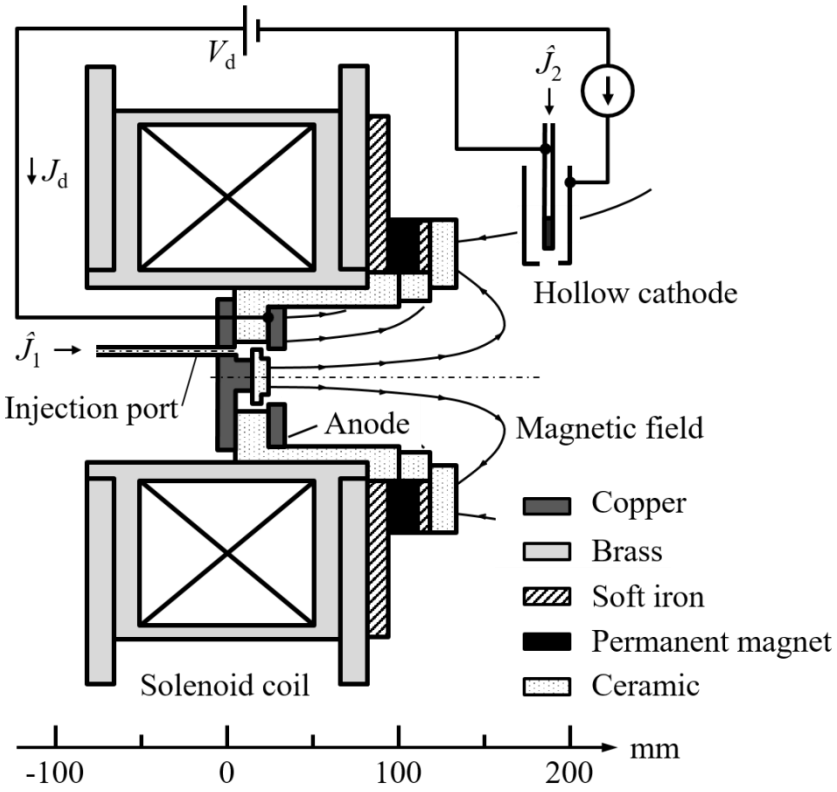

FIG. 5.1 Schematic of DM-EST, "nominal" (N) configuration.

The magnetic configuration and device geometry are similar to those of the End-Hall thruster (as shown in Fig 1.3 (c)). However two significant differences exist between the DM-EST and End-Hall thruster. As mentioned in section 1.3, the End-Hall thruster has a diverging section in its anode that is parallel to the diverging magnetic field lines of forces to create an ion beam with a wide divergence half-angle for plasma processing application. Conversely, the anode of the DM-EST has a ring shape without a diverging section. In the DM-EST, the ring anode surface is exposed only in the short zone at which efficient ionization of the propellant is expected to occur. Second, in the DM-EST, the propellant gas that is injected in the axial direction through an annular slit between the ring anode and an insulator does not directly impinge against any wall in the downstream. The enhancement of the ionization at the exit of the slit on the inner surface of the ring anode is essentially important for decreasing the anode potential drop.[128] Therefore, it is necessary to open the downstream region of the annular slit toward downstream such that a sufficient potential drop is generated near the anode inner surface.

Figure 5.2 shows the four types of magnetic field profiles that are examined in this chapter, namely Types N, S, A, and C. Type N corresponds to the same magnetic field profile as in the HEST. The cylindrical coordinates (r, z) for the axisymmetric configuration are defined on the central axis with their origin at the downstream surface of the insulating plate. The magnetic field strength B at the origin, B(0 mm, 0 mm), and at the exit of the annular slit, B(13.5 mm, 0 mm) were used to characterize each magnetic field profile. In Type N (Fig. 5.2(a)), the inner support that backed the insulating plate was made of copper. The magnetic field inside the ring anode was relatively uniform, i.e., B(0 mm, 0 mm) = B(13.5 mm, 0 mm) = 100 mT. In the other types shown in Figs. 5.2(b) to 5.2(d), the magnetic field profile near the ring anode was modified by changing the material of the inner and outer supports. In Type S (Fig. 5.2(b)), the magnetic field inside the ring anode was almost uniformly enhanced by using inner and outer supports composed of soft iron. The length of the outer support at its inner-most portion corresponded to only 9 mm and was connected to another 9 mm long cylinder composed of copper. Bothe the magnetic field strengths at the center and the ring anode inner surface were both increased within a variation of 10%, i.e., B(0 mm, 0 mm) = 210 mT and B(13.5 mm, 0 mm) = 190 mT. In Type A (Fig. 5.2(c)), the insulating plate was backed by a copper inner support with the same shape as the inner support of Type S. The magnetic field increased only near the ring anode inner surface by using an outer support composed of soft iron, which possessed a full length without a copper extension cylinder such as that used in Type S. The magnetic field displayed a higher enhancement near the ring anode inner surface (B(13.5 mm, 0 mm) = 250 mT) when compared to that on the central axis (B(0 mm, 0 mm) = 150 mT). In Type C (Fig. 5.2(d)), the copper inner support was replaced by an inner support composed of soft iron with the same shape as that of Type S. Additionally, the outer support was composed of copper. The magnetic field displayed a maximum enhancement near the central axis, with B(0 mm, 0 mm) = 300 mT and B(13.5 mm, 0 mm) = 190 mT.

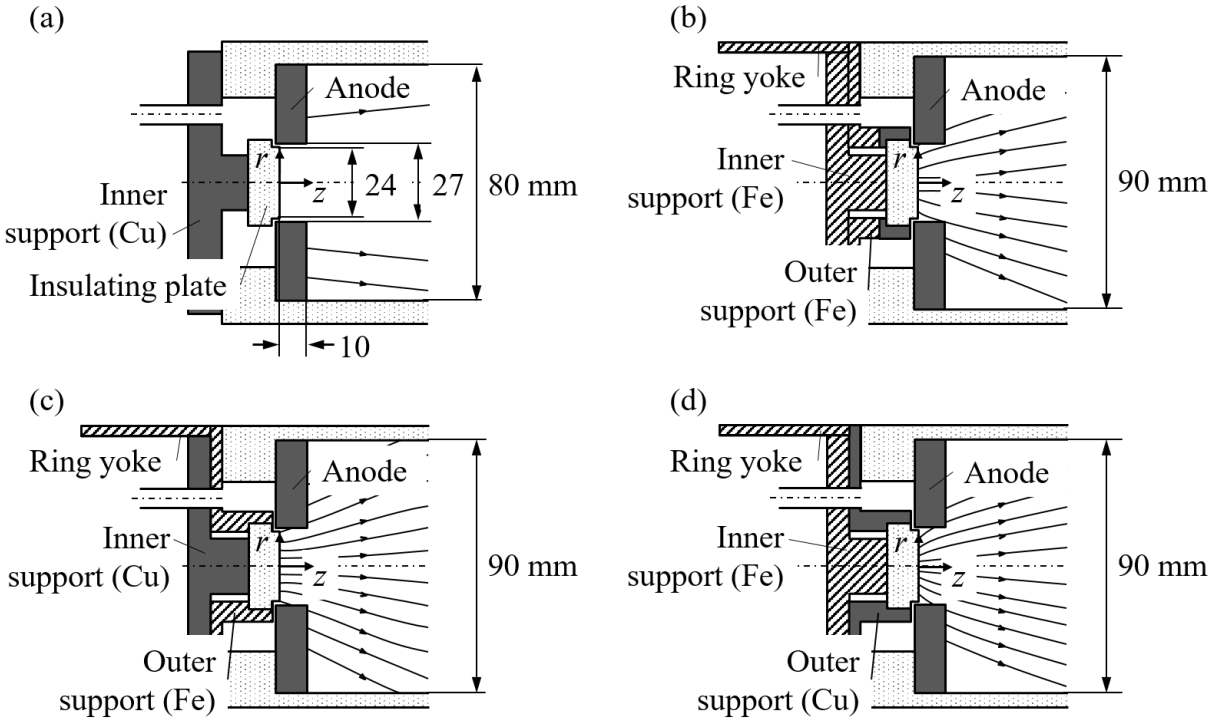

FIG. 5.2 Applied magnetic fields: (a) Type N, (b) Type S, (c) Type A, and (d) Type C.

5.3. Operating conditions

All experiments were conducted in Chamber-B. The flow rate of the working gas injected through the slit, $\hat{J}_1$, was set to 1.0 Aeq and the discharge voltage V_d ranged from 125 V to 225 V. The hollow cathode was operated with a working gas flow rate, $\hat{J}_2$, of 0.36 Aeq, and the keeper current J_k was set as 2.0 A. Each operating condition used to measure E_i, J_i, $\langle\theta\rangle$, J_d, and the keeper voltage V_k was repeated at least twice. A symbol depicts an average value in the following figures. The error bars in E_i, J_i, J_d, and $\langle\theta\rangle$ correspond to the standard deviation ($\pm\sigma$) obtained by several trials. The working gas supplied through the slit as well as through the hollow cathode corresponded to argon (purity 99.9999%). The operation time corresponded to a minimum of 3.5 s in each operating condition. In order to evaluate the effect of the insulating plate erosion, the insulating plate mass was measured by an electric balance (AW320, Shimazu Corp.) before and after five operation cycles (10 s run and 30 s interval) at the condition corresponding to $\hat{J}_1$ = 1.0 Aeq, $\hat{J}_2$ = 0.36 Aeq, and V_d = 200 V in a Type A magnetic field. The mass difference before and

after operation was smaller than the resolution of the electric balance (0.1 mg), and this corresponds to a maximum of 2 μg/C.

5.4. Ionization and acceleration scenario in diverging magnetic field

Figure 5.3 shows n_e, T_e, and V_s distributions in the Type N magnetic field.

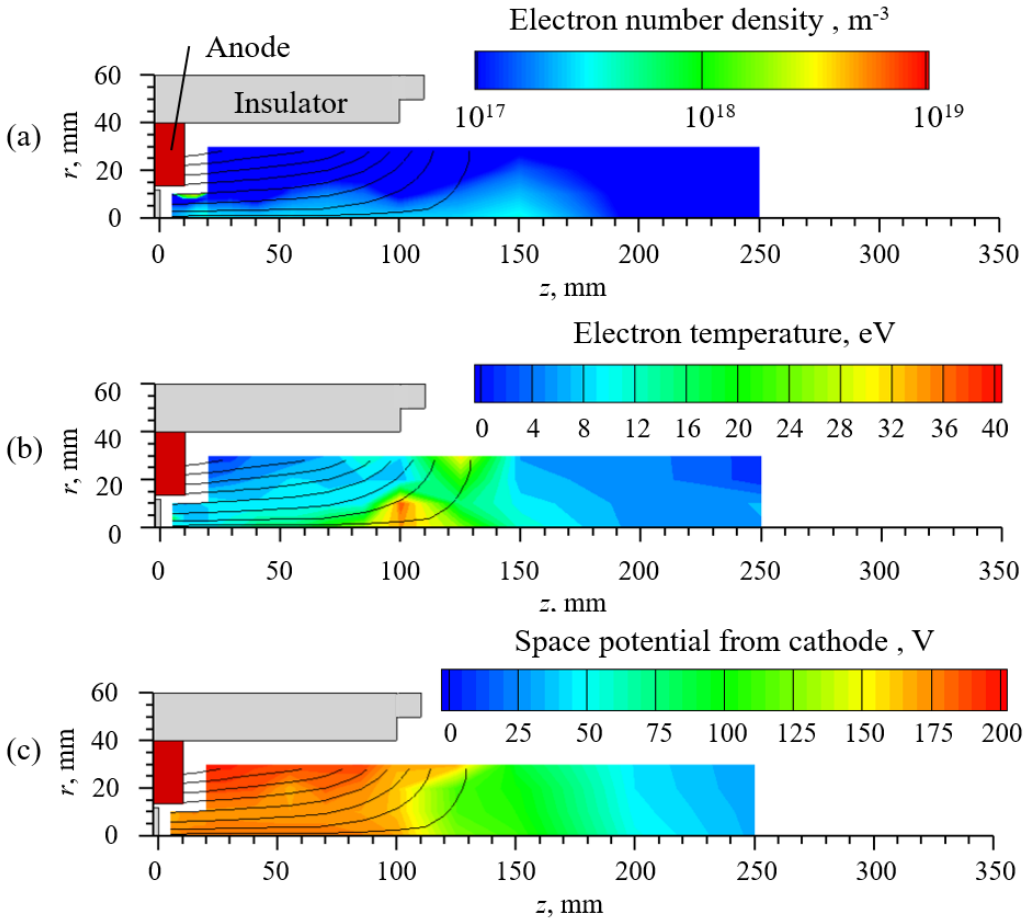

FIG. 5.3 n_e, T_e, and V_s distributions for Type N magnetic field with $\hat{J}_1$ = 0.50 Aeq, $\hat{J}_2$ = 0.36 Aeq, and V_d = 300 V.

As shown in Fig. 5.3(a), electrons are radially confined around the center axis by the diverging magnetic field. Additionally n_e exhibited a peak value of 3.2×10^{18} m^{-3} in the vicinity of the anode inner surface. As described in Ref. 128, the discharge chamber pressure increased when the working gas was injected through efflux holes or slits in the anode itself. The density of neutrals increases with increase in pressure, and thus, the ionization probability for a given electron flux

also increases. At this position, V_s corresponded to 180 V, and this is lower than the anode voltage by 20 V. This voltage drop exceeds the ionization energy of argon (15.8 eV). Therefore, the injected working gas was ionized at the exit of the slit by collisions with the accelerated electrons through the voltage drop. This scheme is hereafter referred to as "near-anode ionization scheme." The location where T_e exhibited a maximum (exceeding 30 eV) shifted downstream at z = 90 – 10 mm (see Fig. 5.3(b)) because the magnetic field rapidly diverged in the magnetic-field-free region. In the region that is immediately downstream from this zone, V_s began decreasing toward the downstream by 150 – 160 V in the region of the measurement.

These potential structures are explained by the mobility difference between ions and electrons. Figure 5.4 shows a schematic of the potential structure between parallel plate electrodes. In Fig. 5.4(a), it was assumed that the anode and the cathode possess same effective electrode areas. Because the electrons has much higher mobility than those of ions, the plasma's space potential (φ_s) exceeded the wall (electrode) potential (φ_w). In the vicinities of the anode and the cathode, the electron sheath was formulated ($\varphi_s > \varphi_w$) to repeal electrons to maintain quasi-neutrality. However, if the effective electrode area of the cathode significantly exceeds that of the anode (see Fig. 5.4(b)), ion flux toward the effective cathode area increases, φ_w exceeds φ_s in the vicinity of the anode to collect more electrons. As shown in Fig. 5.5, the DM-EST has the hollow cathode in the magnetic field-free region. An electron cloud is created in this region. The electron cloud works as an ion sink. Therefore, the effective cathode area exceeds that of the anode, and the space potential of the plasma was lower than that of the anode potential. In summary, the whole scenario of ion's generation and acceleration is as follows: At the entrance slit in the anode inner surface, the introduced neutral gas was ionized by electrons that gained a kinetic energy by the radial potential difference corresponding to the order of 10^1 V that exceeded the ionization energy of argon (15.8 eV). Subsequently, ions were accelerated by the potential drop corresponding to the order of 10^2 V from the exit of the diverging magnetic nozzle.

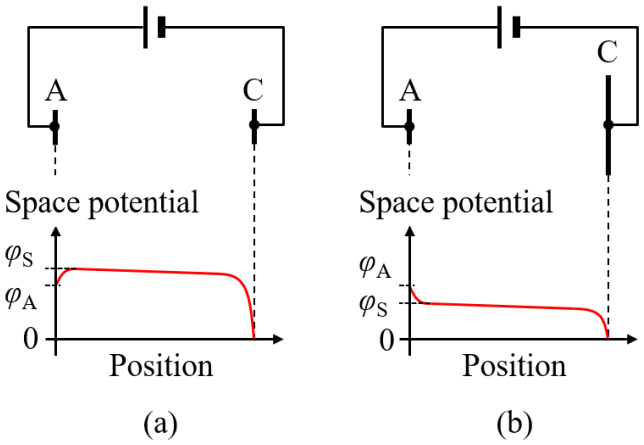

FIG. 5.4 A schematic of space potential structure in the case in which (a) anode and cathode possess the same effective electrode area, and (b) the cathode has larger effective electrode area than that of the anode.

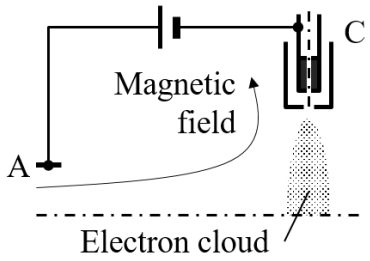

FIG. 5.5 Schematic of electron cloud and the electrodes.

5.5. Ion acceleration characteristics

5.5.1. Effect of magnetic field strength

In this section, the effect of the magnetic field strength was examined by comparing the ion beam characteristics of Types N and S in which have a relatively uniform applied magnetic field. Figure 5.6(a) shows the $j_i(\theta)$ distribution in Types N and S. In Types N and S, more than 175 V of discharge voltage was necessary for the breakdown and steady-state operation. In Type N, $j_i(\theta)$ exhibited a local peak at θ = 0 deg. and ± 50 deg. However, in Type S, $j_i(\theta)$ exhibited a maximum only at approximately θ = 0 deg. and then monotonically decreased with increase $|\theta|$. As shown in Fig. 5.6(b), the $<\theta>$ value of Type S was smaller than that of Type N by more than 10 deg. For example, at V_d = 225 V, $<\theta>$ corresponded to 52 deg. and 40 deg. for Types N and S, respectively.

In the case of Type N, <θ> increased by 3 deg. with increase in V_d from 175 to 225 V. However, the variation of <θ> did not exceed 1 deg in Type S.

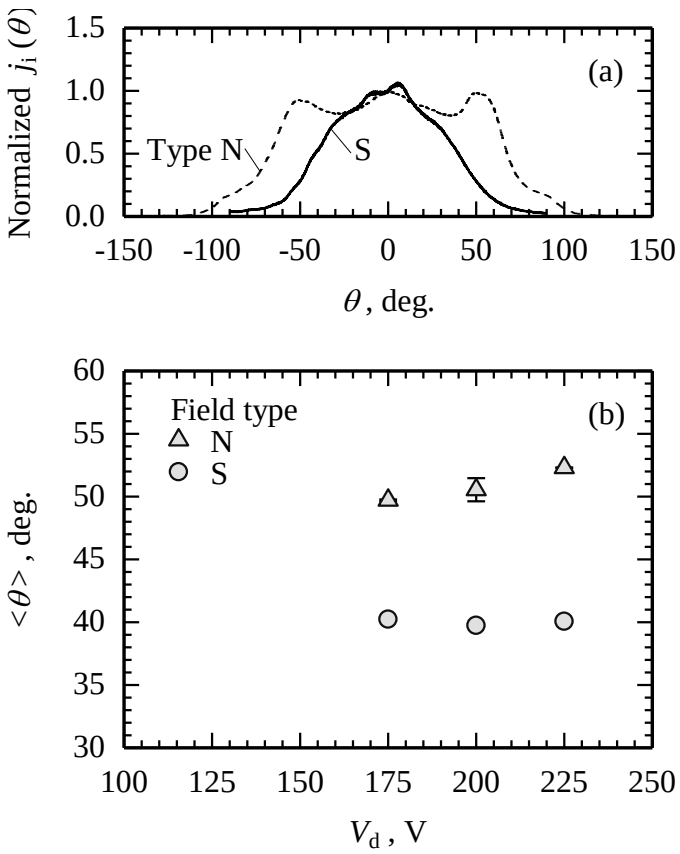

FIG. 5.6 Ion beam distribution characteristics in Types N and S magnetic fields, where $\hat{J}_1$ = 1.0 Aeq and $\hat{J}_2$ = 0.36 Aeq; (a) normalized ion beam current density j_i relative to angle θ with respect to the central axis for V_d = 200 V, (b) <θ> relative to V_d.

Figure 5.7 shows the V_d dependence of E_i, J_i, and J_d for Type N and S. In both types, the average value of E_i increased almost linearly with increase in V_d. In the steady-state operation ($V_d \geq 1.75$ V), the slope dE_i/dV_d corresponded to 0.65 and 1.0 for Type N and Type S, respectively. At V_d = 225 V, J_i was 87% and 100% of the total working gas flow rate $\hat{J}_1 + \hat{J}_2$ for Types N and S, respectively. In the latter, ion production by magnetized electrons increased due to the better confinement achieved by the stronger magnetic field. In both types, J_i was saturated to a value of $\hat{J}_1 + \hat{J}_2$ with increase in V_d. As shown in Fig. 5.7, J_d increased with the stronger magnetic field of Type S; at V_d = 225 V, J_d = 2.1 A and 2.6 A for Type N and S, respectively. Additionally, J_d

increased with increase in V_d in both types without saturation and exceeded $\hat{J}_1$ by a factor of 2 or higher. J_d equaled the electron current flowing into the ring anode, which corresponded to the sum of the ion current that should be neutralized by electrons and an "excess" electron current due to the diffusion of thermionic electrons from the hollow cathode. Additionally, J_i saturated with increase in V_d while J_d increased monotonically, and thus, the ratio J_i/J_d exhibited a maximum value corresponded to 0.67 for both types in the presented configuration; 67% of J_d corresponded to the ion current and the remaining corresponded to the electron backflow from the hollow cathode to the acceleration region. In Type N, J_i/J_d exhibited a peak value at V_d = 200 V. In Type S, it exhibited a maximum at V_d = 175 V and decreased monotonically with increase in V_d.

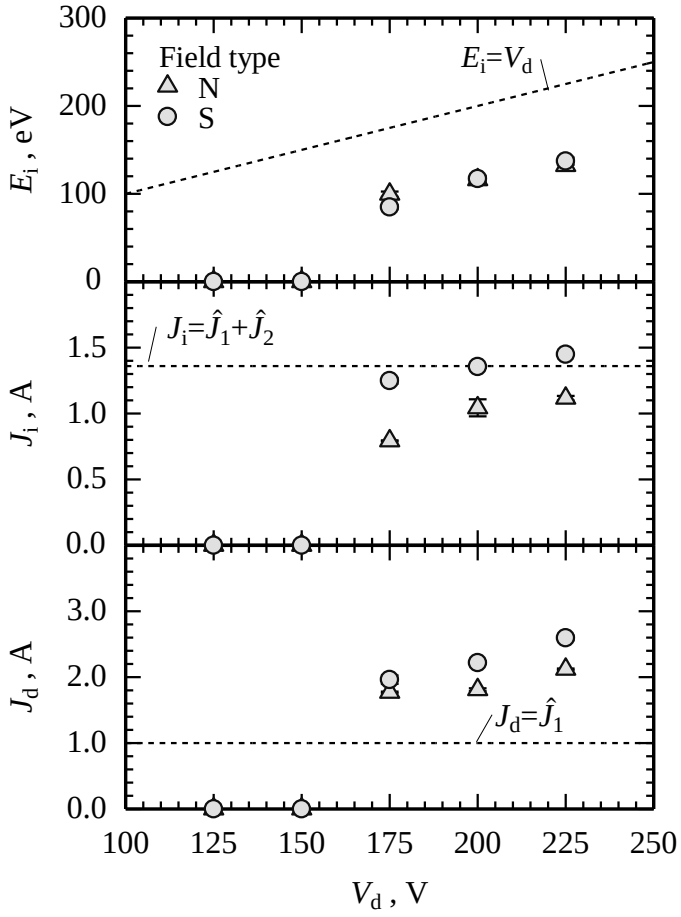

FIG. 5.7 V_d vs. E_i, J_i, and J_d for magnetic field Types N and S with $\hat{J}_1$ = 1.0 Aeq and $\hat{J}_2$ = 0.36 Aeq.

5.5.2. Effect of magnetic field distribution

In this section, the operation characteristics of Types A and C were compared to those of Type S to evaluate the effect of the magnetic field distribution. Figure 5.8(a) shows the $j_i(\theta)$ distribution for Types S, A, and C. Only in Type A, breakdown and steady-state operation were possible at a low discharge voltage corresponding to a minimum of V_d = 125 V. In Type A, j_i (θ) exhibited local maxima at θ = ± 10 deg., and these exceeded $j_i(0)$ by 5 to 10%. In a manner similar to Type S, j_i (θ) in Type C exhibited a peak value only at the central axis at θ = 0 deg. Figure 5.8(b) shows the V_d dependence of $<\theta>$ in Types S, A, and C. In contrast to Type S, the $<\theta>$ value of Type C increased with increase in V_d. However, it decreased in Type A. Among the types examined in this study, Type A exhibited the smallest $<\theta>$, and this corresponded to 39 deg. at V_d = 225 V.

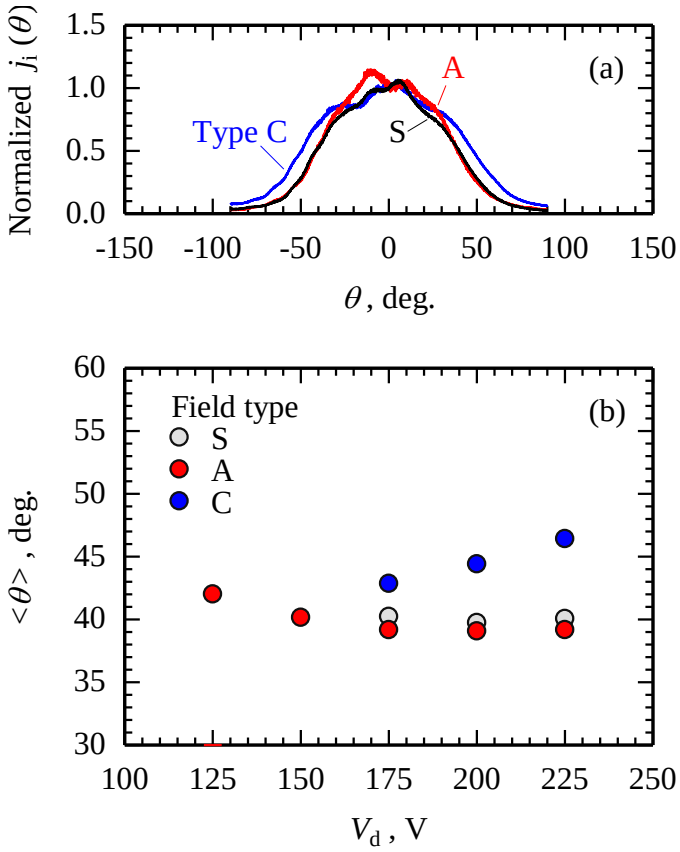

FIG. 5.8 Ion beam distribution characteristics for magnetic field Types S, A, and C with $\hat{J}_1$ = 1.0 Aeq and $\hat{J}_2$ = 0.36 Aeq; (a) normalized ion beam current density j_i vs. angle θ with respect to the central axis for V_d = 200 V, (b) $<\theta>$ vs. V_d.

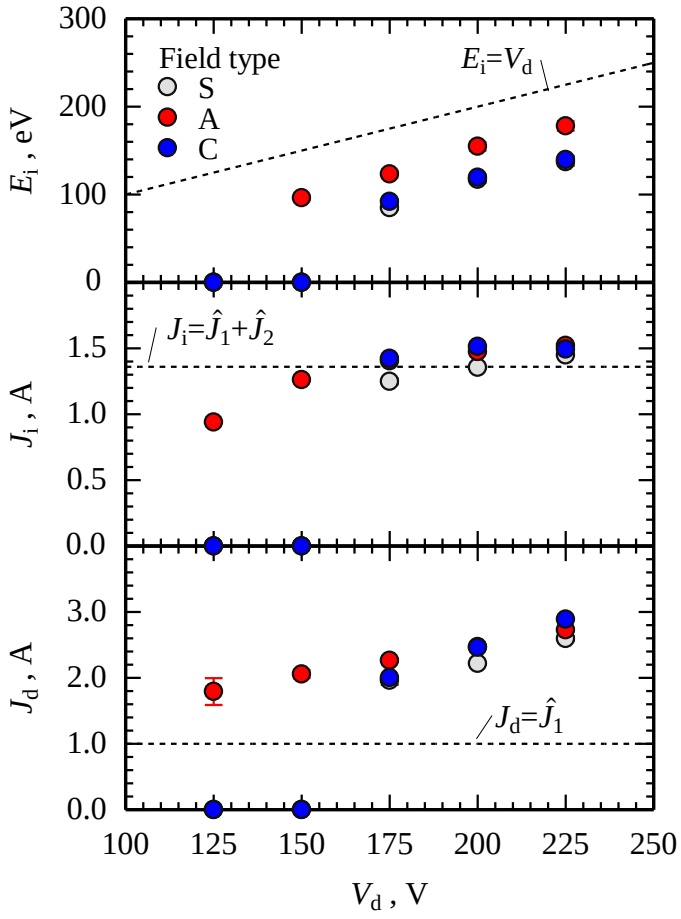

FIG. 5.9 V_d vs. E_i, J_i and J_d for magnetic field Types S, A, and C with $\hat{J}_1$ = 1.0 Aeq and $\hat{J}_2$ = 0.36 Aeq.

Figure 5.9 shows the V_d dependence of E_i, J_i, and J_d for Types S, A, and C. In Types A and C with increase in V_d, E_i increased almost linearly with the same increasing rate as Type S, $dE_i/dV_d \approx 1.0$ in the steady-state region ($V_d \geq 175$ V for Type C, and $V_d \geq 150$ V for Type A). When V_d corresponded to the range 175 V – 225 V, E_i of Type C differed from that of Type S by not more than 8%. However, in Type A, E_i exceeded that of Type S by approximately 40 eV, and E_i/V_d corresponded to 0.79 at V_d = 225 V. A clear difference was not observed in the variation of J_i among Types S, A, and C. At V_d = 225 V, J_i saturated at a value that slightly exceeded $\hat{J}_1+\hat{J}_2$. The cause for this excess value was not clearly identified and could be due to failure of the symmetry, doubly charged ions, or other reasons. However, it is expected that this small discrepancy will not

affect the conclusions obtained from the present experiments. In both Types A and C, J_d increased without saturation and subsequently J_i/J_d decreased with increase in V_d.

5.6. High impedance ion acceleration mechanisms in diverging magnetic field

In this section, the probe diagnostics results are used to analyze the ion acceleration and discharge characteristics discussed in Section 5.5.

5.6.1. Enhancement of the near-anode ionization scheme

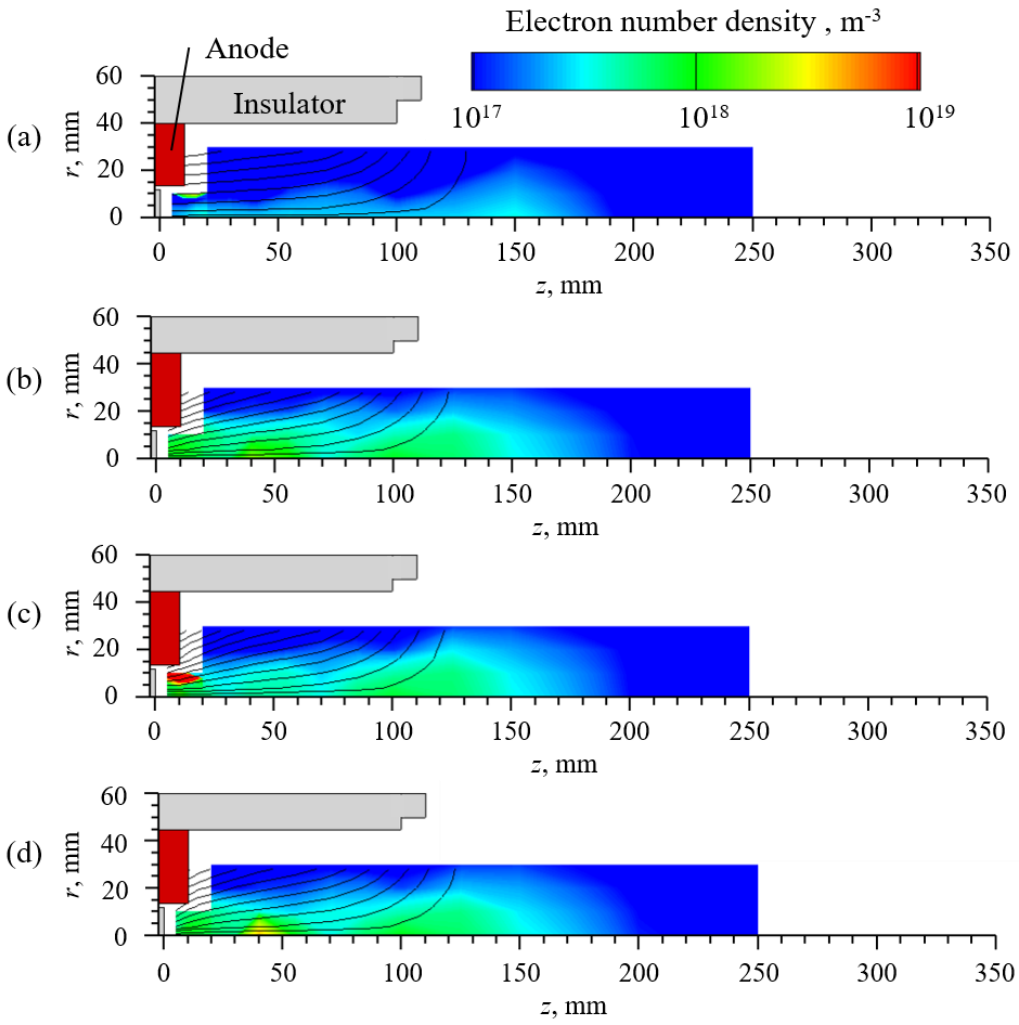

FIG. 5.10 Distributions of n_e for varying magnetic field types: (a) Type N, (b) Type S, (c) Type A, and (d) Type C with $\hat{J}_1$ = 1.0 Aeq, $\hat{J}_2$ = 0.36 Aeq, and V_d = 200 V.

As shown in Figs. 5.7 and 5.9, in Types S, A, and C, J_i exceeded that of Type N by 18 – 25%, and this indicates that J_i increases with increase in B. Figure 5.10 shows the n_e distribution for

each magnetic field type. In Types S, A, and C with a strong magnetic field, n_e on the central axis inside the ring anode corresponded to the order of 10^{18} m^{-3}. In Type C, n_e exhibited a local peak value of 1.8×10^{18} m^{-3} at (r, z) = (0 mm, 40 mm).

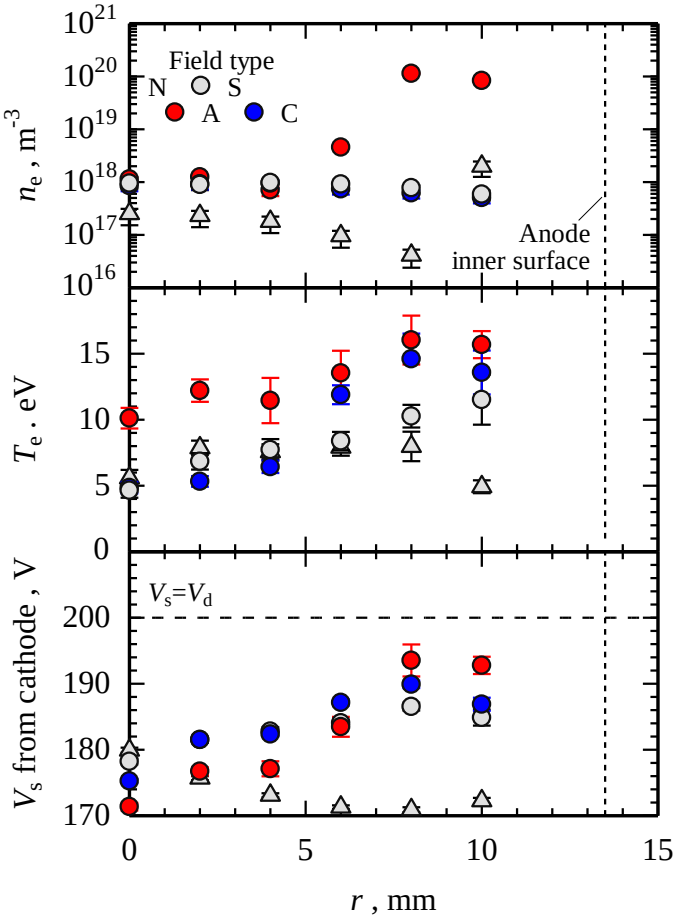

FIG. 5.11 Distributions of n_e, T_e, and V_s at z = 10 mm for various magnetic field types with $\hat{J}_1$ = 1.0 Aeq, $\hat{J}_2$ = 0.36 Aeq, and V_d = 200 V.

Figure 5.11 shows the radial distributions of n_e, T_e, and V_s at z = 10 mm near the right-hand-side end of the ring anode. In Type N with a relatively weak magnetic field of 100 mT, n_e remained at a low level of up to 2×10^{17} m^{-3} for $r \leq 8$ mm. However, it increased to 2×10^{18} m^{-3} at r = 10 mm due to the near-anode ionization scheme. In all other locations, n_e was higher in Types S and C when compared with that in Type N, and ranged between 5.0×10^{17} and 1.0×10^{18} m^{-3} in the entire r range. In Type A, n_e was at the same level as those in Types S and C for $r \leq 4$ mm, and it

subsequently increased to 1.0×10^{20} m^{-3} at r = 8 and 10 mm. Figure 5.12 shows the obtained current – voltage characteristics of the double probe measurements in Type A magnetic field at (a) (r, z) = (10 mm, 10 mm) and (b) (r, z) = (0 mm, 10 mm), respectively. The ion saturation current I_{sat} at (r, z) = (10 mm, 10 mm) exceeded than the ion saturation current at (r, z) = (0 mm, 10 mm) by 10^2 times. In both locations, the correlation coefficient exceeded 0.99, and thus, n_e in the vicinity of the ring anode inner surface can exceed that of the central axis value by 10^2.

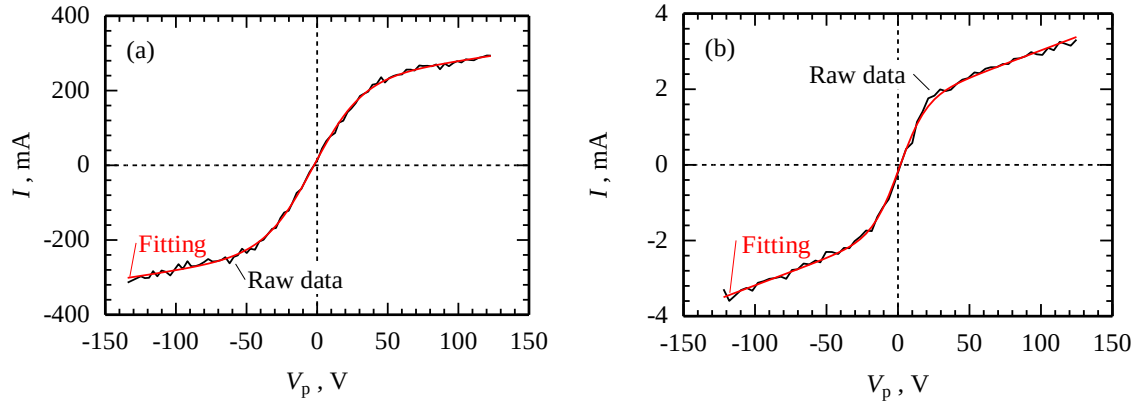

FIG. 5.12 Current (I) – voltage (V_p) characteristics of the double probe measurement in Type A magnetic field at (a) (r, z) = (10 mm, 10 mm), and (b) (r, z) = (0 mm, 10 mm), $\hat{J}_1$ = 1.0 Aeq, $\hat{J}_2$ = 0.36 Aeq, V_d = 200 V.

In Types N, S, and C, T_e approximately corresponded to 5.0 eV and increased slowly with increase in r. In Type N, T_e decreased at r = 10 mm, and this corresponded to an increase of n_e. In Type S, T_e continued to increase with increasing r. In Type A, T_e remained at the highest level corresponding to 10 – 16 eV. In Type C, T_e increased to the same level as Type A at r = 8 mm as shown in Fig. 5.10, and only Type A displayed a region of very high n_e of the order corresponding to 10^{19} m^{-3} near the inner surface of the ring anode. In Type N, V_s at z = 10 mm decreased with increase in r from 180 V at the center to 170 V at r = 10 mm. In Types S, A, and C that has a stronger magnetic field, V_s increased from the axis to the ring anode inner surface. In Type A, V_s was lowest at the central axis with a value of 171 V, and this was lower than the anode potential

(= V_d) by 29 V. Hence, strengthening magnetic field in the vicinity of the ring anode enhanced the near-anode ionization scheme.

5.6.2. Obliquely inward electric field

As shown in Figs. 5.6(b) and 5.8(b), $\langle\theta\rangle$ depends on the strength as well as the profile of the applied magnetic field. Specifically, $\langle\theta\rangle$ decreases in the following order: Types N, C, S, and A. Figure 5.13 shows color contours of T_e for all types. Each T_e distribution exhibited a peak in the diverging magnetic field. In Type N, T_e exhibited a maximum of approximately 34 eV near the central axis at z = 100 mm. In Types S, A, and C, the maximum T_e near 30 eV appeared upstream, at approximately z = 55 – 85 mm.

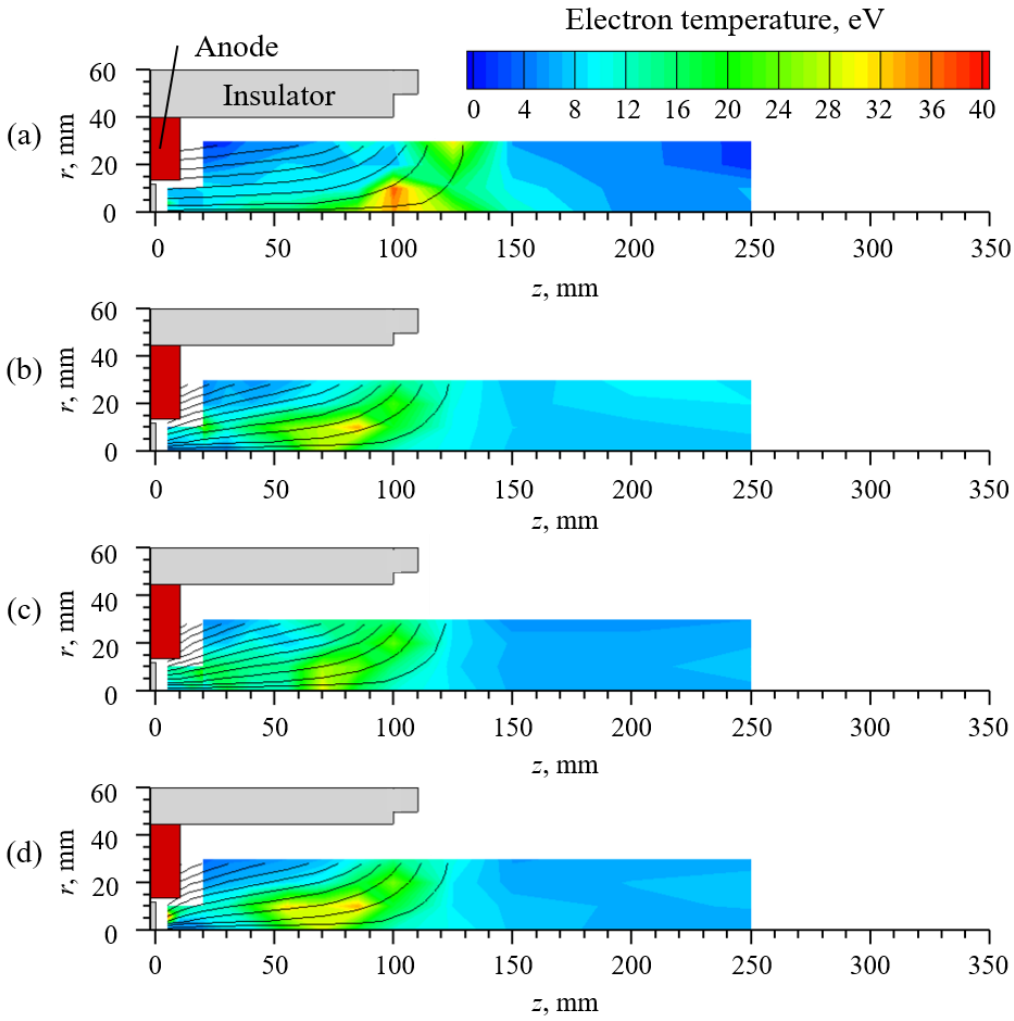

FIG. 5.13 Distributions of T_e for various magnetic field types: (a) Type N, (b) Type S, (c) Type A, and (d) Type C with $\hat{J}_1$ = 1.0 Aeq, $\hat{J}_2$ = 0.36 Aeq, and V_d = 200 V.

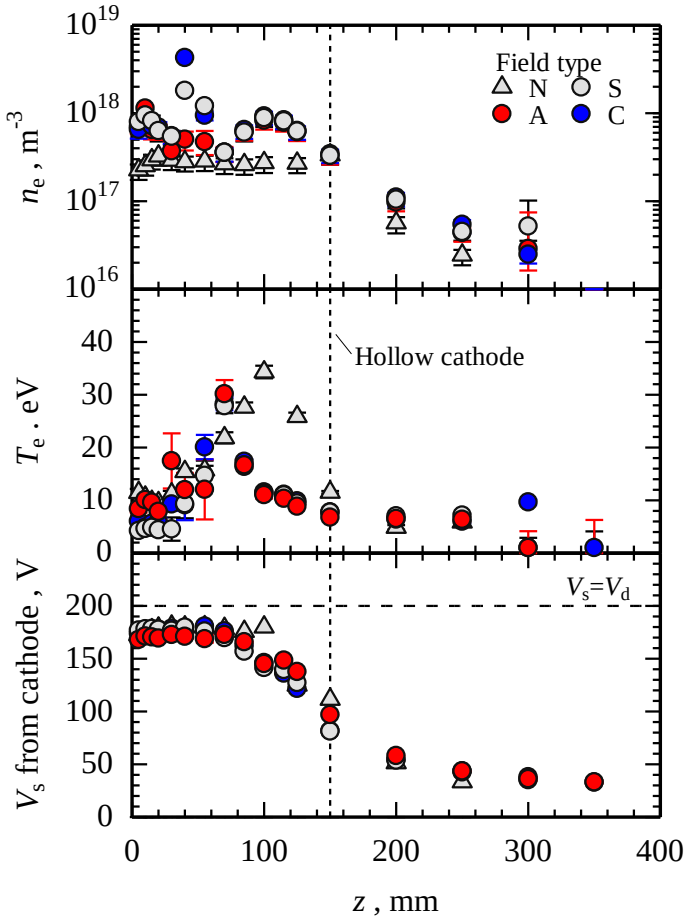

FIG. 5.14 Distributions of n_e, T_e, and V_s at the central axis for various magnetic field types with $\hat{J}_1$ = 1.0 Aeq, $\hat{J}_2$ = 0.36 Aeq, and V_d = 200 V.

Figure 5.4 shows the distributions of n_e, T_e, and V_s at the central axis. In the region near the maximum T_e, V_s began decreasing in the downstream direction. In Type N, V_s began decreasing at approximately z = 100 mm, where T_e corresponded to a maximum. However, in the other types that possess a stronger magnetic field, V_s began decreasing at z = 70 – 80 mm. These results suggest that increasing the magnetic field results in shifting the location of the ion acceleration region toward the ring anode. Figure 5.15 shows the color contours of V_s for all the examined magnetic field types. The strengthening of the magnetic field, as shown in Types S, A, and C, an electric field oriented obliquely inward, particularly in 50 mm ≤ z ≤ 100 mm region. The electric field collimated ions, and thereby decreased the $<\theta>$ value of Types S, A, and C with respect to that of Type N. The strength of the electric field was based on the space potential distribution and

resulted in a lowered space potential at the central axis. As shown in Fig. 5.4, Type A had the lowest space potential at the central axis for z = 0 – 55 mm and the smallest $\langle\theta\rangle$.

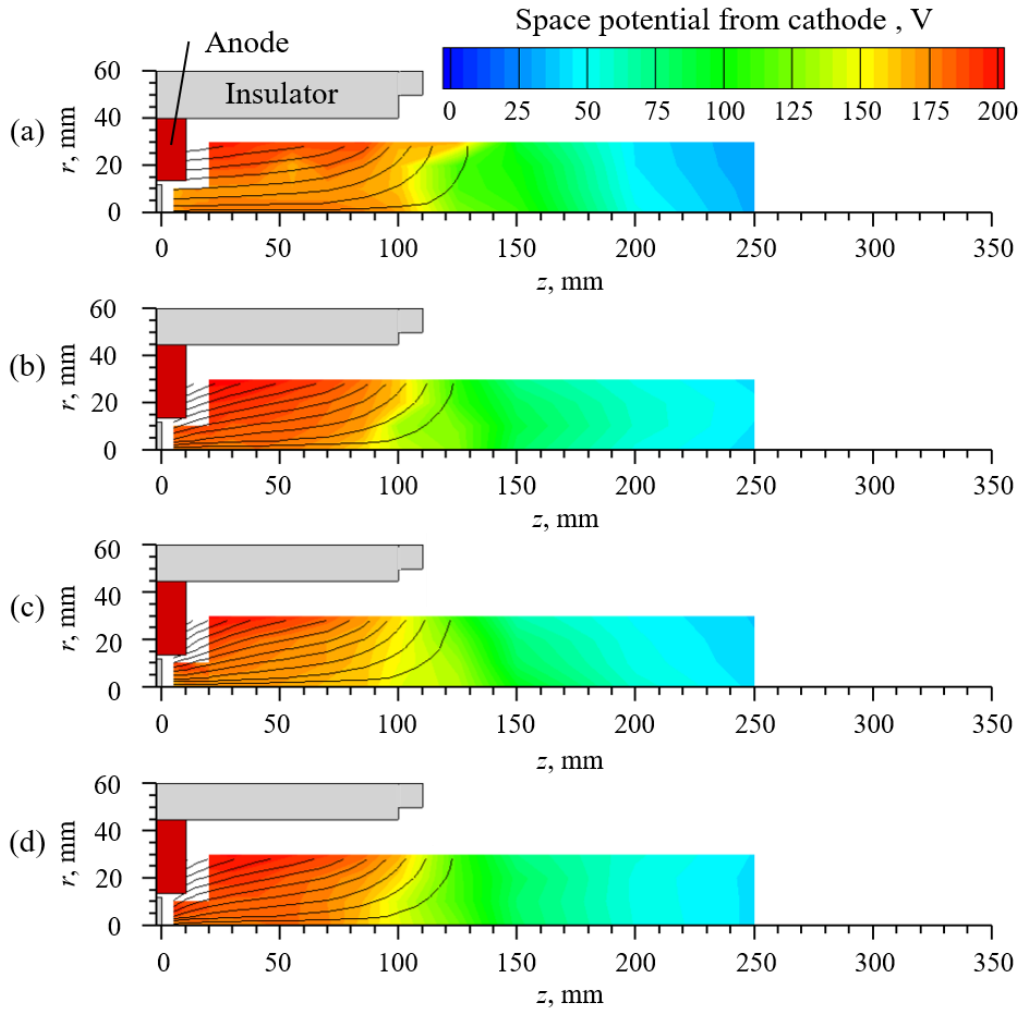

FIG. 5.15 Distributions of V_s for various magnetic field types: (a) Type N, (b) Type S, (c) Type A, and (d) Type C with $\hat{J}_1$ = 1.0 Aeq, $\hat{J}_2$ = 0.36 Aeq, and V_d = 200 V.

As shown in Eq. (2.7), the ion energy E_i of electrostatic acceleration was determined by the space potential difference from the ionization position (see φ_b in Fig. 2.10) to the IEDF measurement position (see φ_s in Fig. 2.10). As shown in Figs. 5.7 and 5.9, Type A exhibited the highest E_i and while the difference in E_i among Types N, S, and C did not exceed 5 eV. In Type A, ionization was locally enhanced near the ring anode inner surface, as shown in Fig. 5.10. The measured V_s at (r, z) = (10 mm, 10 mm) corresponded to 193 V and was close to the φ_b value

(=190 V) measured by the RPA. In Types N, S, and C, n_e exhibited maxima corresponding to 172 V, 181 V, and 179 V at (r, z) = (10 mm, 10 mm), (0 mm, 40 mm), and (0 mm, 40 mm), respectively. With respect to the IEDF measurement position (r, z) = (0 mm, 350 mm) as shown in Fig. 5.4, V_s was almost equal for all magnetic field types. Therefore, E_i mainly depends on V_s at the ionization position. In Type A, the enhanced ionization near the ring anode potential induced by the combination of the near-anode ionization scheme with the strengthened magnetic field increased the efficiency of the electrostatic ion acceleration.

5.7. Summary of Chapter 5

Working gas was injected along the inner surface of the ring anode, and the ionization efficiently occurred by the near-anode ionization scheme, and ions were electrostatically accelerated by an axial potential drop near the exit of the diverging magnetic field. A locally strengthened applied magnetic field at the ring anode inner surface achieved the highest ion beam energy and the smallest beam divergence of 39 deg. In the acceleration region, an obliquely inward electric field converged ions to the central axis, thereby mitigating ion collisions against the channel wall. Subsequently, ions were accelerated through a potential drop in the axial direction.

6.

Conclusions

The present dissertation involved experimentally demonstrating high impedance ion acceleration in applied diverging magnetic field to realize high thruster performance in conjunction with mitigating ion wall losses.

A thermionic emission type hollow cathode was used to maintain small current – high voltage discharge in a diverging magnetic field of applied-field magnetoplasmadynamic (Af-MPD) thruster. The ratio of applied- to self-field thrusts ranged from 10^2 to 10^3. The discharge voltage has a useful component of back electromotive force. Using the hollow cathode, applied-field dominant operation was achieved under the same specific power level (10^2 – 10^4 MJ/kg) although with 1/10 to 1/100 times smaller mass flow rates when compared to those reported in previous studies. A maximum thrust efficiency of 13% was achieved even with a 10 A level of discharge current. However, estimated back electromotive force ratio to the discharge voltage indicated that the input power was mainly consumed by anode sheath drop; based on the thrust measurement, excessive acceleration of the ions led to an inefficient thruster operation.

In order to decrease power consumption in the anode sheath drop, injecting pre-ionized working gas was examined in helicon electrostatic thruster (HEST), which has a radio-frequency (RF) plasma source. The RF power had different effects on thruster operation characteristics at different RF power ranges under a constant discharge voltage of 300 V. With respect to an argon gas flow rate of 0.5 Aeq operation in the RF power range of 0 W to 80 W, RF power was utilized for working gas ionization in the plasma source and subsequently enhanced electrostatic

acceleration through an axial electric field from the end of the diverging magnetic field. In this power range, ionization enhancement in the plasma source contributed to improving ion acceleration performance. However, in the RF power range exceeding 80 W, the ion beam current and the ion beam energy were both gradually saturated at 93% of the total flow rate and 88% of the discharge voltage equivalent, respectively. In this case, injected working gas was ionized with a high ionization cost corresponding to a maximum of 2190 W/A. In the 1.0 Aeq operation, the ion beam current exceeded the total supplied working gas flow rate of 1.36 Aeq by inputting RF power exceeding 400 W. The RF power increment was consumed for low energy and doubly charged ion generation. The thrust efficiency was governed by the RF power ratio relative to electrostatic acceleration power. In both flow rates, the thrust efficiency reached a maximum value at the RF power ratio relative to the electrostatic acceleration power of 0.6 – 1.0. Although additional RF power was input to the electrostatic acceleration power, expected thruster performance remained less than 10% under the same specific input power level of 10^3 MJ/kg as that of the Af-MPD thruster.

Instead of the RF plasma source, injecting working gas from the vicinity of the anode is another method for enhancing ionization near the anode without additional inputting power. An electron cloud was created in the downstream region due to the magnetic field-free region. Because the effective cathode area is larger than that of the anode, the anode potential was higher than that of space potential in order to keep quasi-neutrality. Thus, electrons obtained kinetic energy exceeding ionization energy through this potential difference. Electron impact ionization occurred in the vicinity of the anode (near-anode ionization scheme) by colliding with the locally injected working gas. The generated ions were electrostatically accelerated by an axial potential drop from the exit of the diverging magnetic field. As a result, the applied voltage was efficiently utilized for electrostatic acceleration. The strengthening of the magnetic field locally near the ring anode inner surface exhibited the highest ion beam energy and smallest beam divergence

corresponding to 39 deg. In the acceleration region, an obliquely inward electric field converged ions to the central axis, thereby ion beam divergence half-angle was decreased.

In summary, the high impedance ion acceleration in diverging magnetic field was demonstrated. (1) By using the hollow cathode, small current – high voltage operation in the diverging magnetic field was maintained. (2) The ions generated by the near-anode ionization scheme were efficiently electrostatically accelerated through the diverging magnetic field. Expected thruster performances based on probe diagnostics, namely 2900 s of specific impulse and to a maximum thrust efficiency of 33% with 30 mN/kw exceeded that of the HEST with inputting optimal RF power, and was comparable to previous electrostatic thrusters operated with a xenon propellant.

References

[1] M. Martinez-Sanchez and J. E. Pollard, "Spacecraft Electric Propulsion – An Overview," *J. Propul. Power* **14**, 688-699 (1998).

[2] Robert H. Frisbee, "Advanced Space Propulsion for the 21st Century," *J. Propul. Power* **19**, 1129-1154 (2003).

[3] Robin Raus, Yang Gao, Yunhua Wu, and Mark Watt, "Analysis of state-of-the-art single-thruster attitude control techniques for spinning penetrator," *Acta Astronaut.* **76**, 60-78 (2012).

[4] A. I. Morozov, "The Conceptual Development of Stationary Plasma Thrusters," *Plasma Phys. Rep.* **29**, 235-250 (2003).

[5] V. A. Obukhov, A. I. Pokryshkin, G. A. Popov, and N. V. Yashina, "Sustainer electric propulsion system application for spacecraft attitude control," *Acta Astronaut.* **67**, 145-154 (2010).

[6] E. Y. Choueiri, "A Critical History of Electric Propulsion: The First 50 Years (1906-1956)," *J. Propul. Power* **20**, 193-203 (2004).

[7] Vatsal Sheth, "Spacecraft Electric Propulsion – A review," *IJRAME* **9**, 43-55 (2014).

[8] Harold Gold, Raymond J. Rulis, Frank A. Maruna, Jr., and William H Hawersaat, "Description and Operation of Spacecraft in SERT 1 Ion Thruster Flight Test," NASA TM. X-52050, 1964.

[9] Ronald J. Cybulski, Daniel M. Shellhammer, Robert R. Lovell, Edward J. Domino, and Joseph T. Kotnik, "Results from SERT 1 ion Rocket Flight Test," NASA TN. D-2718, 1965.

[10] Kazuhisa Fujita, and Yoshihiro Arakawa, "Anode Heat Loss and Current Distributions in a DC Arcjet," *J. Propul. Power* **12**, 120-126 (1996).

[11] Monika Auweter-Kurtz, Thomas Gölz, Harald Habiger, Frank Hammer, Helmut Kurtz, Martin Riehle, and Christian Sleziona, "High-Power Hydrogen Arcjet Thrusters," *J. Propul. Power* **14**, 764-773 (1998).

[12] A. Kaminska, A. Bialek, and M. Dudeck, "Perfomance of an Argon Arc-jet Thruster for Satellites," *Rom. Journ. Phys.* **60**, 549-559, 2015.

[13] Paul J. Wilbur, Vincent K. Rawlin, and J. R. Beattie, "Ion Thruster Development Trends and Status in the United States," *J. Propul. Power* **14**, 708-715 (1998).

[14] James S. Sovey, Vincent K. Rawlin, and Michael J. Patterson, "Ion Propulsion Development Projects in U.S.: Space Electric Rocket Test I to Deep Space 1," *J. Propul. Power* **17**, 517-526 (2001).

[15] Shoji Kitamura, Yasushi Ohkawa, Yukio Hayakawa, Hideki Yoshida, and Katsuhiro Miyazaki, "Overview and research atatus of the JAXA 150-mN ion engine, " *Acta Astronaut.* **61**, 360-366 (2007).

[16] Kenn E. Clark, and Robert G. Jahn, "The Magnetoplasmadynamic Arcjet," *Acta Astronaut.* **13**, 315-325 (1967).

[17] Monika Auweter-Kurtz, "Plasma Thruster Development Program at the IRS," *Acta Astronaut.* **32**, 377-391 (1994).

[18] K. Toki, Y. Shimizu, and K. Kuriki, "On-Orbit Demonstration of a Pulsed Self-Field Magnetoplasmadynamic Thruster System," *J. Propul. Power* **16**, 880-886 (2000).

[19] Gerd Krülle, Monika Auweter-Kurtz, and Akihiro Sasoh, "Technology and Application Aspects of Applied Field Magnetoplasmadynamic Propulsion," *J. Propul. Power* **14**, 754-763 (1998).

[20] Dan R. Lev, and Edgar Y. Choueiri, "Scaling of Efficiency with Applied Magnetic Field in Magnetoplasmadynamic Thrusters," *J. Propul. Power* **28**, 609-616 (2012).

[21] Riccardo Albertoni, Fabrizio Paganucci, Paola Rossetti, and Mariano Andrenucci, "Experimental Study of a Hundred-Kirowatt-Class Applied-Field Magnetoplasmadynamic Thruster," *J. Propul. Power* **29**, 1138-1145 (2013).

[22] R. L. Burton, and P. J. Turchi, "Pulsed Plasma Thruster," *J. Propul. Power* **14**, 716-735 (1998).

[23] Abdolrahim Rezaeiha, and Tony Schönherr, "Review of Worldwide Activities in Liquid-Fed Pulsed Plasma Thruster," *J. Propul. Power* **30**, 253-264 (2014).

[24] Harold R. Kaufman, "Technology of Closed-Drift Thrusters," *AIAA J.* **23**, 78-87 (1985).

[25] A. I. Morozov, and V. V. Savelyev, "Fundamentals of stationary plasma thruster theory," Reviews of plasma physics, Springer US, New York, 203-391 (2000).

[26] Michael D. West, Christine Charles, and Rod W. Boswell, "Testing of a Helicon Double Layer Thruster Immersed in a Space-Simulation Chamber," *J. Propul. Power* **24**, 134-141 (2008).

[27] W. Andrew Hoskins, R. Joseph Cassady, Olwen Morgan, Roger M. Myers, Fred Wilson, David Q. King, and Kristi deGrys, "30 Years of Electric Propulsion Flight Experience at Aerojet Rocketdyne," in Proceedings of the 33rd *International Electric Propulsion Conference*, Princeton, USA (2013), IEPC Paper No. 2013–439.

[28] Kybecom Kwon, Mitchell L R Walker, and Dimitri N Mavris, "Self-consistent, one-dimensional analysis of the Hall effect thruster," *Plasma Sources Sci. Technol.* **20**, 045021 (2011).

[29] V. P. Kim, "Design Features and Operating Procedures in Advanced Morozov's Stationary Plasma Thrusters," *Tech. Phys.* **60**, 362-375 (2015).

[30] David Y. Oh, John Steven Snyder, Dan M. Goebel, Richard R. Hofer, and Thomas M. Randolph, "Solar Electric Propulsion for Discovery-Class Missions," *J. Spacecraft Rockets* **51**, 1822-1835 (2014).

[31] M. Dudeck, F. Doveil, N. Arcis, and S. Zurbach, "Plasma Propulsion for Geostationary Satellites and Interplanetary Spacecraft," *Rom. Journ. Phys.* **56** Supplement, 3-14 (2011).

[32] M. G. Marcucci and J. E. Polk, "NSTAR Xenon Ion Thruster on Deep Space 1: Ground and flight tests," *Rev. Sci. Instrum.* **71**, 1389-1400 (2000).

[33] Marc D. Rayman, Philip Varghcsc, David H. Lechman, and Leslie L, Livesay, "Results from the Deep Space 1 Technology Validation Mission," *Acta Astronaut.* **47**, 475-487 (2000).

[34] C. T. Russell and C. A. Raymond, "The Dawn Mission to Vesta and Ceres," *Space Sci. Rev.* **163**, 3-23 (2011).

[35] Peter Rathsman, Joakim Kugelbergm Per Bodin, Giuseppe D. Racca, Bernard Foing, and Luca Stagnaro, "SMART-1: Development and lesson learnt," *Acta Astronaut.* **57**, 455-468 (2005).

[36] Takashi Asai, Katsuhiko Yamada, and Ichiro Jikuya, "Fuel-Efficient Low-Thrust Transfer in Elliptic Orbits," *Trans. JSASS Aerospace Tech. Japan* **12**, Pd_1-Pd_9 (2014).

[37] Vladimir Kim, "Main Physical Features and Processes Determining the Performance of Stationary Plasma Thrusters," *J. Propul. Power* **14**, 736-743 (1998).

[38] Käthe Dannenmayer and Stéphan Mazouffre, "Elementary Scaling Relations for Hall Effect Thrusters," *J. Propul. Power* **27**, 236-245 (2011).

[39] Y. J. Ding, D. R. Yu, D. C. Jia, G. J. Yan, and H. Li, "Scaling Design and Experimental Study on Hall Thrusters with Curved Magnetic Field," *Contrib. Plasma Phys.* **51**, 68-82 (2011).

[40] Andrey A. Shagaya, "On Scaling of Hall Effect Thrusters," *IEEE T. Plasma Sci.* **43**, 12-28 (2015).

[41] Dan M. Goebel and Ira Katz, "Fundamentals of Electric Propulsion: Ion and Hall Thrusters," John Wiley & Sons, 440-442 (2008).

[42] Kurt A. Polzin, Thomas E. Markusic, Boris J. Stanojev, Amado DeHoyos, Yevgeny Raitses, Artem Smirnov, and Nathaniel J. Fisch, "Performance of a Low-Power Cylindrical Hall Thruster," *J. Propul. Power* **23**, 886-888 (2007).

[43] Akihiro Sasoh, "Generalized Hall Acceleration," *J. Propul. Power* **10**, 251-254 (1994).

[44] Robert G. Jahn, "Physics of Electric Propulsion," McGraw-Hill, New York, 142-195 (1968).

[45] Francis F. Chen, "Introduction to Plasma Physics and Controlled Fusion second edition," Plenum Press, New York, 2005.

[46] M. Keidar, D. Boyd, and I. I. Beilis, "Plasma flow and plasma-wall transition in Hall thruster channel," *Phys. Plasmas* **8**, 5315-5322 (2001).

[47] A. A. Ivanov, A. A. Ivanov jr, and M. Bacal, "Effect of plasma-wall recombination on the conductivity in Hall thrusters," *Plasma Phys. Control. Fusion* **44**, 1463-1470 (2002).

[48] Subrata Roy and B. P. Pandey, "Plasma-Wall interaction inside a Hall thruster," *J. Plasma Physics* **68**, 305-319 (2002).

[49] E. Ahedo and J. M. Gallardo, "Effects of the radial plasma-wall interaction on the Hall thruster discharge," *Phys. Plasmas* **10**, 3397-3409 (2003).

[50] Kimiya Komurasaki and Yoshihiro Arakawa, "Two-Dimensional Numerical Model of Plasma Flow in a Hall Thruster," *J. Propul. Power* **11**, 1317-1323 (1995).

[51] Kimiya Komurasaki and Yoshihiro Arakawa, "Performance Calculation of Hall Thrusters," *Acta Astronaut.* **38**, 185-192 (1996).

[52] S. Mazouffre, K. Dannenmayer, and J. Pérez-Luna, "Examination of plasma-wall interactions in Hall effect thrusters by means of calibrated thermal imaging," *J. Appl. Phys.* **102**, 023304 (2007).

[53] S. Mazouffre, K. Dannenmayer, and C. Blank, "Impact of discharge voltage on wall-losses in a Hall thruster," *Phys. Plasmas* **18**, 064501 (2011).

[54] Richard R. Hofer, Dan M. Goebel, Ioannis G. Mikellides, and Ira Katz, "Magnetic shielding of a laboratory Hall thruster. II. Experiments, " *J. Appl. Phys.* **115**, 043304 (2014).

[55] L. Garrigues, G. J. Hagelaar, J. Bareilles, C. Boniface, and J. P. Boeuf, "Model study of the influence of the magnetic field configuration on the performance and lifetime of a Hall thruster," *Phys. Plasmas* **10**, 4886-4892 (2003).

[56] Hiroyuki Koizumi, Kimiya Komurasaki, and Yoshihiko Arakawa, "Numerical prediction of wall erosion on a Hall thruster," *Vacuum* **83**, 67-71 (2009).

[57] Thomas Burton and Gregory Thompson, "Plasma-Induced Erosion on Ceramic Wall Structures in Hall-Effect Thrusters," *J. Propul. Power* **30**, 690-695 (2014).

[58] Richard R Hofer, Robert S. Jankovsky and Alec D. Gallimore, "High-Specific Impulse Hall Thrusters, Part 1: Influence of Current Density and Magnetic Field," *J. Propul. Power* **22**, 721-731 (2006).

[59] Lubos Brieda and Michael Keidar, "Plasma-wall interaction in Hall thrusters with magnetic lens configuration," *J. Appl. Phys.* **111**, 123302 (2012).

[60] Ioannis G. Mikellides, Ira Katz, Richard R. Hofer, and Dan M. Goebel, "Magnetic shielding of a laboratory Hall thruster. I. Theory and validation," *J. Appl. Phys.* **115**, 043303 (2014).

[61] Ioannis G. Mikellides, Ira Katz, Richard R. Hofer, and Dan M. Goebel, "Magnetic shielding of walls from the unmagnetized ion beam in a Hall thruster," *Appl. Phys. Lett.* **102**, 023509 (2013).

[62] Stéphane Mazoeffre, Julien Vaudolon, Guillaume Largeau, Carole Hénaux, Alberto Rossi, and Dominique Harribey, "Visual Evidence of Magnetic Shielding with the PPS-FLEX Hall Thruster," *IEEE T. Plasma Sci.* **42**, 2668-2669 (2014).

[63] R. W. Conversano, Ph.D. thesis, University of California, Los Angeles, 2015.

[64] Y. Raitses and N. J. Fisch, "Parametric investigations of a nonconventional Hall thruster," *Phys. Plasmas* **8**, 2579-2586 (2001).

[65] Artem Smirnov, Yegeny Raises, and Nathaniel J. Fisch, "Experimental and theoretical studies of cylindrical Hall thrusters," *Phys. Plasmas* **14**, 057106 (2007).

[66] Y. Raitses, A. Smirnov, and N. J. Fisch, "Enhanced performance of cylindrical Hall thrusters," *Appl. Phys. Lett.* **90**, 221502 (2007).

[67] N. Koch, H. P. Harmann, and G. Kornfeld, "Development and test status of the THALES high efficiency multistage plasma (HEMP) thruster family," in Proceedings of the 29th International Electric Propulsion Conference, Princeton, USA (2005), IEPC Paper No. 2005–297.

[68] N. A. MacDonald, M. A. Cappelli, S. R. Glldea, M. Martinez-Sánchez, and W. A. Hargus Jr, "Leaser-induced fluorescence velocity measurements of a diverging cusped-field thruster," *J. Phys. D: Appl. Phys.* **44**, 205203 (2011).

[69] C. Ryan, T. Wantock, T. Harle, and A. Konll, "Performance Characteristics of the Low-Power Halo Electric Propulsion System," *J. Propul. Power* **32**, 1544-1549 (2016).

[70] N. A. MacDonald, C. V. Yound, M. A. Cappelli, and W. A. Hargus Jr, "Ion velocity and plasma potential measurements of a cylindrical cusped field thruster," *J. Appl. Phys.* **111**, 093303 (2012).

[71] S. Mazouffre, S. Tsikata, and J. Vaudolon, "Development and experimental characterization of a wall-less Hall thruster," *J. Appl. Phys.* **116**, 243302 (2014).

[72] Julien Vaudolon, Stéphane Mazouffre, Carole Hénaux, Dominique Harribey, and Alberto Rossi, "Optimization of a wall-less Hall thruster," *Appl. Phys. Lett.* **107**, 174103 (2015).

[73] Günter Kornfeld, and Werner Schwertfege, PCT/DE2001/001106 (22 March 2001).

[74] Günter Kornfeld, Norbert Koch, and Hans-Peter Harmann, "New performance and reliability results of the THALES hemp thruster," in Proceedings of the 4th International Spacecraft Propulsion Conference, Sardinia, Italy (1004), SP-555.

[75] C. Charles, "Plasmas for spacecraft propulsion," *J. Phys. D: Appl. Phys.* **42**, 163001 (2009).

[76] Eduardo Ahed, and Jaume Navarro-Cavallé, "Helicon thruster plasma modeling: Two-dimensional fluid-dynamics and propulsive performances," Phys. Plasmas **20**, 043512 (2013).

[77] Alexey V. Arefiev and Boris N. Breizman, "Ambipolar acceleration of ions in a magnetic nozzle," *Phys. Plasmas* **15**, 042109 (2009).

[78] Adam Shabshelowitz and Alec D. Gallimore, "Performance and Probe Measurements of a Radio-Frequency Plasma Thruster," *J. Propul. Power* **29**, 919–929 (2013).

[79] Harlod R. Kaufman, Raymond S. Robinson, and Richard Ian Seddon, "End-Hall ion source," *J. Vac. Sci. Technol.* **A5**, 2081-2084 (1987).

[80] S. Harada, T. Baba, A. Uchigashima, S. Yokota, A. Iwakawa, A. Sasoh, T. Yamazaki, and H. Shimizu, "Electrostatic acceleration of helicon plasma using a cusped magnetic field," *Appl. Phys. Lett.* **105**, 194101 (2014).

[81] Akihiro Sasoh and Yoshihiro Arakawa, "A high-resolution thrust stand for ground tests of low-thrust space propulsion devices," *Rev. Sci. Instrum.* **64**, 719-723 (1993).

[82] M. Yonemoto and A. Sasoh, "Operation Characteristics of a Steady-State, Two-Dimensional MPD Thruster Using a Hollow Cathode," *T. Jpn. Soc. Aeronaut. S.* **10**, 7-12 (2012).

[83] J. A. Simpson, "Design of retarding field energy analyzers," *Rev. Sci. Instrum.* **32**, 1283–1293 (1961).

[84] I. H. Hutchinson, Principles of Plasma Diagnostics second edition, Cambridge University Press, 65–67 (2002).

[85] Lyon B. King and Alec D. Gallimore, "Identifying charge-exchange collision products within the ion-energy distribution of electrostatically accelerated plasmas," *Phys. Plasmas* **6**, 2936-2942 (1999).

[86] L. Gamigues, "Lon properties in a Hall current thruster operating at high voltage," *J. Appl. Phys.* **119**, 163305 (2016).

[87] Bryan Michael Reid, Ph.D. thesis, University of Michigan, MS, 2009.

[88] M. L. R. Walker, R. R. Hofer, and A. D. Gallimore, "Ion Collection in Hall Thruster Plumes," *J. Propul. Power* **22**, 205–209 (2006).

[89] Joshua L. Rovey, Mitchell L. R. Walker, Alec D. Gallimore, and Peter Y. Peterson, "Magnetically filtered Faraday , probe for measuring the ion current density profile of a Hall thruster," *Rev. Sci. Instrum.* **77**, 013503 (2006).

[90] Daniel L. Brown and Alec D. Gallimore, "Evaluation of ion collection area in Faraday probes," *Rev. Sci. Instrum.* **81**, 063504 (2010).

[91] A. von Engel, "Ionized Gases" Oxford University Press, 87 (1965).

[92] D. L. Brown, C. W. Larson, B. E. Beal, and A. D. Gallimore, "Methodology and historical perspective of a Hall thruster efficiency analysis," *J. Propul. Power* **25**, 1163–1177 (2009).

[93] P. Staib, "An E×B analyzer to study the particle fluxes, energy, and charge state in the scrape-off layer of Tokamaks," *J. Nucl. Mater.* **93&94**, 351-356 (1980).

[94] Youbong Lim, Holak Kim, Wonho Choe, Seung Hun Lee, Jongho Seon, and Hae June Lee, "Observation of a high-energy tail in ion energy distribution in the cylindrical Hall thruster plume," *Phys. Plasmas* **21**, 103502 (2014).

[95] D. Renaud, D. Gerst, S. Mazouffre, and A. Anesland, "E×B probe measurements in molecular and electronegative plasmas," *Rev. Sci. Instrum.* **86**, 123507 (2015).

[96] Bu. Wrenger and K. H. Meiwes-Broer, "The application of a Wien filter to mass analysis of heavy clusters from a pulsed supersonic nozzle source," *Rev. Sci. Instrum.* **68**, 2027-2030 (1997).

[97] Rohit Shastry, Richard R. Hofer, Bryan M. Reid, and Alec D. Gallimore, "Method of analyzing E×B probe spectra from Hall thruster plumes," *Rev. Sci. Instrum.* **80**, 063502 (2009).

[98] E. O. Johnson and L. Malter, "A Floating Double Probe Method for Measurements in Gas Discharge," *Phys. Rev.* **80**, 58-70 (1950).

[99] Daniel A. Herman and Alec D. Gallimore, "An ion thruster internal discharge chamber electrostatic probe diagnostic technique using a high-speed probe positioning system," *Rev. Sci. Instrum.* **79**, 013302 (2008).

[100] P. Chung, "Electrostatic probes in stationary and flowing plasmas: Part 1. Collisionless and transitional probes," *AIAA J.* **12**, 133-144 (1974).

[101] Irving Langmuir, "The Pressure Effect and Other Phenomena in Gaseous Discharges," *J. Franklin Inst.* **196** 751–62 (1923).

[102] J. P. Sheehan, Y. Raitses, N. Hershkowitz, I. Kaganovich, and N. J. Fisch, "A comparison of emissive probe techniques for electric potential measurements in a complex plasma," *Phys. Plasmas* **18**, 073501 (2011).

[103] A. Fruchtman, D. Zoler, and G. Makrinich, "Potential of an emissive cylindrical probe in plasma," *Phys. Rev. E* **84**, 025402 (2011).

[104] J. P. Sheehan and N. Hershkowitz, "Emissive probes," *Plasma Sources Sci. Technol.* **29**, 063001 (2011).

[105] D. Yordanov, St. Lishev, and A. Shivarova, "How does a probe inserted into the discharge influence the plasma structure?," *J. Appl. Phys.* **119**, 183302 (2016).

[106] Y. Raitses, M. Keidar, D. Staack, and N. J. Fisch, "Effects of segmented electrode in Hall current plasma thrusters," *J. Appl. Phys.* **92**, 4906-4911 (2006).

[107] D. Staack, Y. Raitses, and N. J. Fisch, "Shielded electrostatic probe for nonperturbing plasma measurements in Hall thrusters," *Rev. Sci. Instrum.* **75**, 393-399 (2004).

[108] T. E. Sheridan "How big is a small Langmuir probe?," *Phys. Plasmas* **7**, 3064-3088 (2000).

[109] G. A. Emmert, R. M. Wieland, A. T. Mense, and J. N. Davidson, "Electric sheath and presheath in a collisionless, finite ion temperature plasma." *Phys. Fluids* **23**, 803-812 (1980).

[110] L. A. Schwager, "Effects of secondary and thermionic electron emission on the collector and source sheaths of a finite ion temperature plasma using kinetic theory and numerical simulation," *Phys. Fluids B* **5**, 631-645 (1983).

[111] Roger M. Myers and George C. Soulas, "Anode Power Deposition in Applied-Field MPD Thrusters," 28th AIAA/ASME/SAE/ASEE Joint Propulsion Conference and Exhibit, AIAA paper 1992-3463, July 1992.

[112] R. M. Myers, N. Suzuki, A. J. Kelly, and R. G. Jahn, "Cathode Phenomena in a Low-Power Magnetoplasmadynamic Thruster," *J. Propul. Power* **7**, 760–766 (1991).

[113] Daisuke Nakata, Kyoichiro Toki, Ikkoh Funaki, and Hiroshi Kuninaka, "Performance of ThO_2-W, Y_2O_3-W, and La_2O_3-W Cathodes in Quasi-Steady Magnetoplasmadynamic Thrusters," *J. Propul. Power* **27**, 912–915 (2011).

[114] Monika Auweter-Kurtz, Bernd Glocker, Helmut I. Kurtz, Otto Loesener, Herbert O. Schrade, Nikolaos Tubanos, Thomas Wegmann, Dieter Willer, and James E. Polk, "Cathode Phenomena in Plasma Thrusters," *J. Propul. Power* **9**, 882–888 (1993).

[115] H. R. Kaufman and J. R. Kahn, "Hollow Cathode Without Low-Work-Function Insert," in Proceedings of the 29th International Electric Propulsion Conference, Princeton, USA (2005), IEPC Paper No. 2005–47.

[116] V. V. Zhurin, A. G. Popov, A. A. Porotnikov, V. B. Tikhonov, and I. A. Utkin, "The State of Research and Development of End-Hall Plasma Thrusters in the USSR," in Proceedings of the 22th International Electric Propulsion Conference, Ohio, USA (1991), IEPC Paper No. 1991–080.

[117] D. B. Fradkin, A. W. Roehling, D. J. Stratton, T. F. Williams, M., and K. W. Liewer, "Experiments using a 25-kW Hollow Cathode Lithium Vapor MPD Arcjet," *AIAA J.* **8**, 886-894 (1970).

[118] Roger M. Myers, "Geometric Scaling of Applied-Field Magnetoplasmadynamic Thrusters," *J. Propul. Power* **11**, 343–350 (1995).

[119] Victor B. Tikhonov, Sergei A. Semenikhin, and James E. Polk, "Own Magnetic Field Impact on MPD Thrusters Performance with External Magnetic Field," in Proceedings of the 26th International Electric Propulsion Conference, Ohio, USA (1999), IEPC Paper No. 1999–176.

[120] H. Tahara, Y. Kagaya, T. Yoshikawa, "Performance and Acceleration Process of Quasisteady Magnetoplasmadynamic Arcjets with Applied Magnetic Fields," *J. Propul. Power* **13**, 651–658 (1997).

[121] A. Sasoh, and Y. Arakawa, "Electromagnetic Effects in an Applied-Field Magnetoplasmadynamic Thruster," *J. Propul. Power* **8**, 98–102 (1992).

[122] A. Sasoh, and Y. Arakawa, "hrust Formula for Applied-Field Magnetoplasmadynamic Thrusters Derived from Energy Conservation Equation," *J. Propul. Power* **11**, 351–356 (1995).

[123] P. G. Mikellides, P. J. Turchi, and N. F. Roehling, "Applied-Field Magnetoplasmadynamic Thrusters, Part 1: Numerical Simulations Using the MACH2 Code," *J. Propul. Power* **16**, 887–893 (2000).

[124] A. D. Gallimore, R. M. Myers, A. J. Kelly, and R. G. Jahn, "Anode power deposition in an applied-field segmented anode MPD thruster," *J. Propul. Power* **10**, 262–268 (1994).

[125] Nerheim N. M. and Kelly A. J., "A Critical Review of the Magnetoplasmadynamic (MPD) Thruster for Space Application," NASA TR 32-1196, Feb. (1968).

[126] A. V. Phelps, "Cross Sections and Swarm Coefficients for Nitrogen Ions and Neutrals in N2 and Argon Ions and Neutrals in Ar for Energies from 0.1 eV to 10 keV," *J. Phys. Chem. Ref. Data* **20**, 557-573 (1991).

[127] J. E. Foster, and A. D. Gallimore, "An investigation into the role that a transverse magnetic field plays in the formation of large anode sheath potentials," *Phys. Plasmas* **3** 4239-4249 (1996).

[128] J. E. Foster, and A. D. Gallimore, "The effect of an auxiliary discharge on anode sheath potentials in a transverse discharge," *J. Appl. Phys.* **81**, 3422-3432 (1997).

[129] Adam Shabshelowitz, and Alec D. Gallimore, “Performance of a Helicon Hall Thruster Operating with Xenon, Argon, and Nitrogen,” *J. Propul. Power* **30**, 664-671 (2014).

[130] T. Shoji, Y. Sakawa, S. Nakazawa, K. Kadota and T. Sato, “Plasma production by helicon waves,” *Plasma Sources Sci. Technol.* **2**, 5-10 (1993).

[131] James M. Hass and Alec D. Gallimore, “Considerations on the Rolle of the Hall Current in a Laboratory Model Thruster,” *IEEE. Trans. Plasma Sci.* **30**, 687-697 (2002).

[132] Jean-Pierre Boeuf, “Physics and modeling of Hall thrusters,” *J. Appl. Phys.* **121**, 011101 (2017).

[133] N. Oudini, G. J. M. Hagellar, J. P. Boeuf and L. Garrigues, “Physics and modeling of an end-Hall (gridless) ion source,” *J. Appl. Phys.* **109**, 073310 (2011).

[134] Sang-Wook Kim, and Alec D. Gallimore, “Plume Study of a 1.35-kW SPT-100 Using an E×B probe,” *J. Spacecraft Rockets* **39**, 904-909 (2002).

[135] Ira Katz, Richard R. Hofer, and Dan M, Goebel, “Ion Current in Hall Thrusters,” *IEEE T. Plasma Sci.* **36**, 2015-2024 (2008).

[136] Yoshiki Yamagiwa and Kyoichi Kuriki, “Performance of Double-Stage-Discharge Hall Ion Thruster,” *J. Propul. Power* **7**, 65-70(1991).

[137] A. Uchigashima, T. Baba, D. Ichihara, A. Iwakawa, A. Sasoh, T. Yamazaki, S. Harada, M. Sasahara, and T. Iwasaki, “Anode geometry effects on ion beam energy performance in helicon electrostatic thruster,” *IEEE. Trans. Plasma Sci.* **44**, 306–313 (2016).